The Non-Linear Electrodynamic Coupling Between the Solar Wind, Magnetosphere and Ionosphere

Frederick D. Wilder

Dissertation submitted to the faculty of the Virginia Polytechnic Institute and State University in partial fulfillment of the requirements for the degree of
Doctor of Philosophy
in
Electrical Engineering

C. Robert Clauer, Chair
Wayne A. Scales
J. Michael Ruohoniemi
Joseph B. H. Baker
Timothy Pratt
John H. Simonetti

March 29, 2011
Blacksburg, VA

Keywords: Solar Wind, Ionosphere, Magnetosphere, Electromagnetics, Plasma Physics

The Non-Linear Electrodynamic Coupling Between the Solar Wind, Magnetosphere and Ionosphere

Frederick D. Wilder

ABSTRACT

The polar electric potential imposed on the ionosphere by coupling between the earth's magnetosphere and the solar wind has been shown to have a non-linear response to the interplanetary electric field (IEF). This dissertation presents an empirical study of this polar cap potential saturation phenomenon. First, the saturation of the reverse convection potential under northward is demonstrated using bin-averaged SuperDARN data. Then, the saturation reverse convection potential is shown to saturate at a higher value at higher solar wind plasma beta. The reverse convection flow velocity is then compared with cross-polar cap flows under southward IMF under summer, winter and equinox conditions. It is demonstrated that the reverse convection flow exhibits the opposite seasonal behavior to cross polar cap flow under southward IMF. Then, an interhemispheric case study is performed to provide an explanation for the seasonal behavior of the reverse convection potential. It is found using DMSP particle precipitation data that the reverse convection cells in the winter circulate at least partially on closed field lines. Finally, SuperDARN and DMSP data are merged to provide polar cap potential measurements for a statistical study of polar cap potential saturation under southward IMF. It is found that the extent of polar cap potential saturation increases with increasing Alfvènic Mach number,

and has no significant relation to Alfvèn wing transmission coefficient or solar wind dynamic pressure.

ACKNOWLEDGEMENTS

I foremost would like to express my most sincere gratitude to my advisor, Professor C. Robert Clauer, who has supported me during the research and also assisted me immensely with his expertise in the field of space science. I'd also like to thank him for all the opportunities to travel and see the world, meeting many exciting people in the process. I would also like to thank Professor Wayne A. Scales for assisting me in my decision to pursue space science as well as introducing me to the field. Thanks also go to Professors John H. Simonetti and Timothy Pratt for serving on my committee.

In addition, I would like to thank Professors Joseph B. H. Baker and J. Michael Ruohoniemi for helping to provide me with some of the software to perform this research, serving on my committee, and providing many helpful discussions on the best way to pursue this phenomenon. Thanks also goes to Drs. Xia Cai and Daniel Weimer, who have provided a large amount of feedback on much of my research. I would also like to thank Dr. Valeriy Petrov and Dr. Vladimir (Volodya) Papitashvili for access to the Flat File Software, as well as the MIST virtual global magnetic observatory. Special thanks to Robin Barnes for providing and assisting me with the SuperDARN toolkit.

Further, I would like to thank Drs. Aaron Ridley, Margaret Kivelson, George Siscoe and Ramon Lopez for providing in depth discussion on their theoretical models which explain polar cap potential saturation. I'd also like to thank Drs. Pat Newell

and Marc Hairston for providing guidance in the use and interpretation of data from the DMSP satellites. Special thanks goes to Ellen Cousins at Dartmouth College for assistance and feedback on my method for merging DMSP and SuperDARN data.

Finally, I would like to thank my Parents and family who have been very supportive throughout my life and academic career as a whole. In addition, I'd like to thank my fiancée, Laura Elizabeth Hofford, whose support has kept me both happy and sane during my time as a doctoral student.

This research is supported by the National Science Foundation through grants ATM-0728538, ATM-0849031, and ANT-0839858 and by NASA through grant NNX07AH23G to the Virginia Tech. Operation of the northern hemisphere SuperDARN radars is supported by the national funding agencies of Canada, France, Japan, the United Kingdom and the United States. The DMSP particle detectors were designed by Dave Hardy of AFRL, and data obtained from JHU/APL.

TABLE OF CONTENTS

LIST OF FIGURES

Figure

LIST OF TABLES

Table

LIST OF APPENDICES

Appendix

CHAPTER I

INTRODUCTION

The interactions between the sun and the Earth have been a subject of fascination since the dawn of human history. With the invention of the telescope, scientists such as Galileo Galilei observed the sun's surface and sunspots (*Russell*, 1995). As modern technology and observational capabilities developed, a scientific discipline known as "solar-terrestrial physics" or "space physics" emerged.

Central to solar-terrestrial physics is the interaction between plasma ejected from the sun and the Earth's magnetic field. The corona is the outermost layer of the sun's atmosphere. It is an extremely hot gas consisting of ionized hydrogen, free electrons, and helium. Due to a large pressure difference between the corona and interplanetary space, this plasma expands outward at supersonic speeds and is called the "solar wind" (*Hundhausen*, 1995). Since the sun is constantly rotating, the portion of the Sun's magnetic field contained within the plasma will be ejected in a spiral shape, similar to a lawn sprinkler, known as the "Parker spiral" (*Hundhausen*, 1995). The Parker spiral is shown in Figure 1.1.

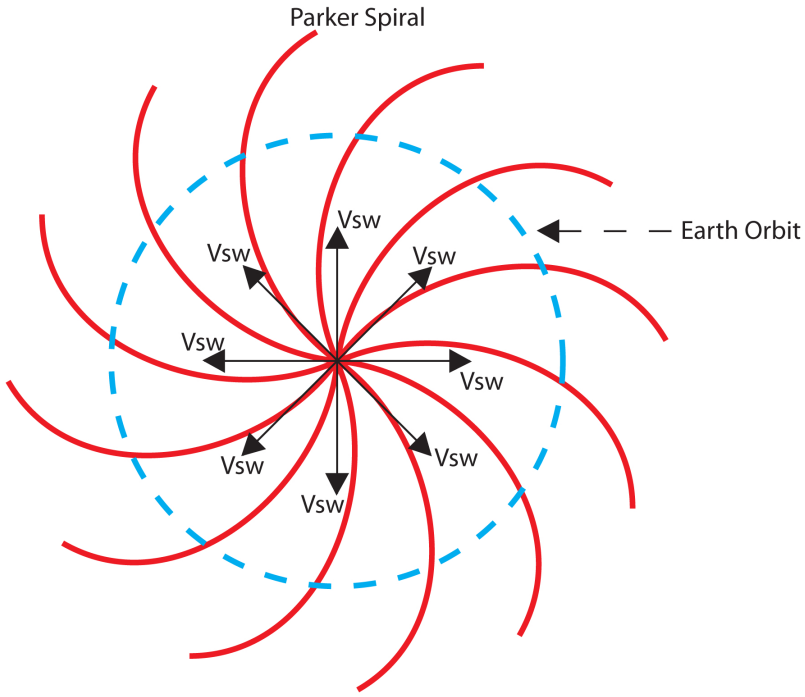

Figure 1.1: Archimedes spiral representation of solar wind propagating at velocity, Vsw (*Hundhausen*, 1995).

1.1 The Solar Wind

1.1.1 The Interplanetary Magnetic Field

Because of its high conductivity, the solar wind is often assumed to be an ideal Magnetohydrodynamic (MHD) fluid. When describing the time rate of change of the magnetic field, it can be shown that the magnetic induction equation becomes:

$$\frac{\partial \mathbf{B}}{\partial t} = \nabla \times (\mathbf{u} \times \mathbf{B}) \tag{1.1}$$

Where $\mathbf{B}$ is the magnetic field contained in the solar wind, and $\mathbf{u}$ is the velocity of the solar wind (*Gurnett and Bhattacharjee*, 2005). Since the right hand side of (1.1) assumes very large conductivity in the solar wind plasma, there is no term included for the diffusion of the magnetic field. It is therefore assumed that the magnetic field is "frozen in" the solar wind and that field lines are carried by the solar wind

bulk velocity (*Gurnett and Bhattacharjee*, 2005). This frozen-in field is called the "interplanetary magnetic field" (IMF).

For this research, the IMF will be measured in geocentric solar magnetospheric (GSM) coordinates. In this, the origin is at the center of the Earth, the positive X axis points towards the sun, the Z axis is oriented along magnetic north, and the Y axis is perpendicular to the Earth's dipole axis, as shown in Figure 1.2(*Kivelson and Russell*, 1995). The Y,Z plane rocks on the X axis as the Earth rotates.

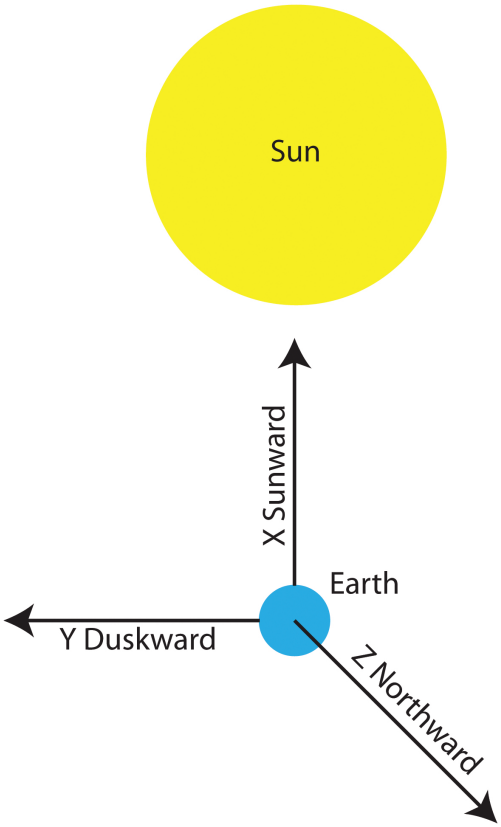

Figure 1.2: The GSM Coordinate System

In MHD, Ohm's law is usually given by (1.2).

$$\mathbf{J} = \sigma(\mathbf{E} + \mathbf{u} \times \mathbf{B}) \tag{1.2}$$

Where **J** is the electric current density in the plasma, σ is the electrical conductivity of the plasma, and **E** is the associated electric field. Due to the frozen in condition, however, the $[\mathbf{E} + \mathbf{u} \times \mathbf{B}]$ term must be negligible to maintain a finite current density (*Hundhausen*, 1995). The associated electric field in the frame of reference of the solar wind plasma is then given by (1.3).

$$\mathbf{E} \approx -(\mathbf{u} \times \mathbf{B}) \tag{1.3}$$

1.1.2 Important Parameters in the Solar Wind

In a compressible, moving plasma such as the solar wind, there are several parameter's which characterize its behavior and how it interacts with obstacles. One such parameter is the dynamic pressure of the plasma, sometimes referred to as "ram pressure," given by (1.4) (*Gurnett and Bhattacharjee*, 2005).

$$P_{dyn} = \rho V^2 \tag{1.4}$$

Where P_{dyn} is the solar wind dynamic pressure, ρ is the density of the plasma, and V is the solar wind bulk speed. Since particles in a plasma cannot cross magnetic field lines, the magnetic field carried by the solar wind also exerts a pressure, called "magnetic pressure" (*Gurnett and Bhattacharjee*, 2005). The ratio of the solar wind's thermal pressure to its magnetic pressure is called the solar wind "plasma beta," and is given by (1.5) (*Gurnett and Bhattacharjee*, 2005).

$$\beta = \frac{P_{th}}{P_{mag}} = \frac{nkT}{B^2/2\mu_0} \tag{1.5}$$

Where β is the solar wind plasma beta, P_{th} is the solar wind thermal pressure, P_{mag} is the solar wind magnetic pressure, n is the solar wind number density, k

is Boltzmann's constant, T is the solar wind temperature in Kelvin, and B is the magnitude of the IMF.

Like any other gas, sound waves can propagate through the solar wind via the vibration of the particles contained therein. The sonic Mach number is the ratio between the solar wind bulk speed and its sound speed. Since it is an MHD fluid, other electromagnetic waves can propagate in it called "MHD waves." The two common wave modes are the Alfvèn wave ("shear" mode) and the magnetosonic wave ("transverse" mode). The Alfvèn wave is an MHD wave which propagates along magnetic field lines, and is analogous to viewing the magnetic field line as a vibrating string. The magnetosonic wave is an MHD wave which propagates transverse to magnetic field lines and is closely related to sound waves. There are also Mach numbers for the Alfvèn wave and magnetosonic wave, which are ratios of the solar wind bulk speed to each wave's respective phase speed. The three Mach numbers and the associated phase speeds are given by (1.6) through (1.8) *Gurnett and Bhattacharjee* (2005).

$$M_{CS} = \frac{V}{V_{CS}} = V(\frac{\rho}{\gamma P_{th}})^{1/2} \tag{1.6}$$

$$M_A = \frac{V}{V_A} = V(\frac{B^2}{\mu_0 \rho})^{-1} \tag{1.7}$$

$$M_{MS} = \frac{V}{V_{MS}} = \frac{V}{(V_A^2 + V_{CS}^2)^{1/2}} \tag{1.8}$$

Where M_{CS}, M_A, and M_{MS} are the sonic, Alfvènic, and magnetosonic Mach numbers, respectively; V_{CS}, V_A, V_{MS}, are the sound, Alfvèn, and magnetosonic speeds, respectively; and γ is related to the number of degrees of freedom in the plasma (often assumed to be 5/3).

1.2 The Earth's Magnetosphere

As the solar wind flows through interplanetary space, it interacts with planetary magnetic fields in a variety of ways. The Earth's magnetic field, for example, presents an obstacle to the solar wind plasma causing a shock to form upstream. The Earth's magnetic field is confined to a cavity in the solar wind flow called the magnetosphere. Due to the dynamic pressure of the solar wind, the magnetosphere is compressed on the day side and drawn into a long comet-like tail behind the Earth on the night side (*Walker and Russell*, 1995). The shocked solar wind flows around the magnetosphere in a region called the magnetosheath. The area where the solar wind dynamic pressure is at a standoff with the Earth's magnetic pressure is called the "magnetopause" and the subsolar magnetopause distance is typically located at about 10 Earth radii (R_E) away from the center of the Earth on the dayside (*Walker and Russell*, 1995). A current system called the "Chapman-Ferraro" currents exists at the magnetopause due to the magnetic shear between the IMF and the Earth's magnetic field, and provides the force necessary to stand-off the solar wind dynamic pressure. Figure 1.3 shows an illustration of a typical interaction between the solar wind and the magnetosphere.

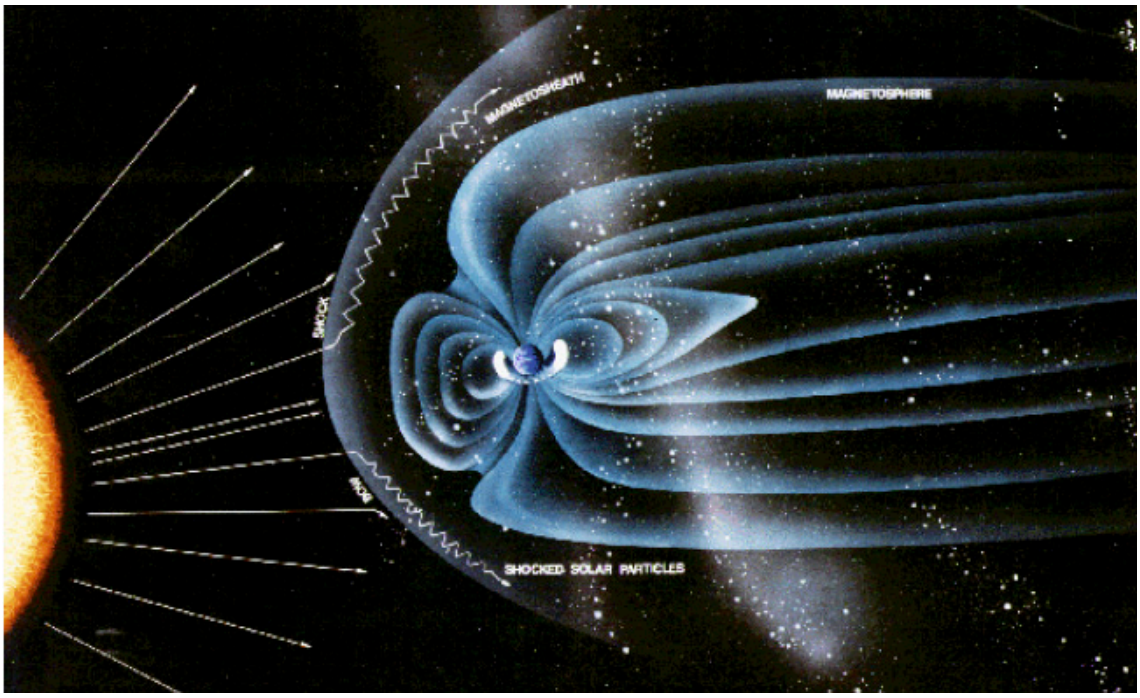

Figure 1.3: An illustration of the solar wind encountering the Earth's magnetosphere. Courtesy of NASA Marshal Space Flight Center's Space Plasma Physics Branch. Available at http://science.nasa.gov/ssl/pad/sppb/edu/magnetosphere/images/mag+sun.gif

Large scale convection of plasma within the magnetosphere is tied to various parameters within the solar wind. This convection maps along magnetic field lines into the Earth's polar ionosphere, where it can have a direct impact on ionospheric electric fields and thus modern technology. It is therefore important to understand the mechanisms by which magnetospheric convection is driven.

1.2.1 Magnetic Reconnection

The primary mechanism whereby energy and momentum are coupled to the magnetosphere from the solar wind is the process of magnetic reconnection on the day side of the Earth (*Dungey*, 1961). Magnetic reconnection is a process in plasma physics where two anti-parallel magnetic field lines collide at very high pressure, and

the field lines literally shear and merge (*Dungey*, 1961). For example, if the IMF is oriented southward when the solar wind encounters the Earth's magnetic field, reconnection will occur on the dayside at the sub-solar point, as in Figure 1.4 (*Dungey*, 1961).

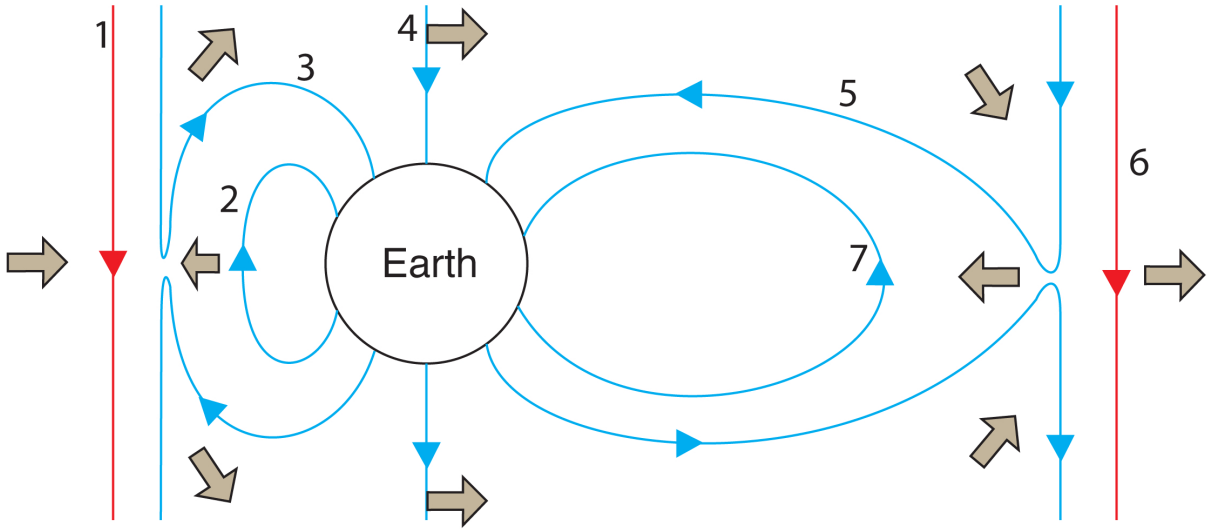

Figure 1.4: Magnetic reconnection and its driving of magnetospheric convection. Red lines are the IMF, blue lines are geomagnetic field lines, and shaded arrows indicate the flow of plasma. The IMF (1) is antiparallel to the geomagnetic field lines (2) near the dayside sub-solar point. These field lines merge in an x-shaped geometry, and form highly bent field lines (3). These new field lines experience high Maxwell stress and are carried over the polar cap (4) where they reconnect again in the tail (5). The reconnection results in two field lines: one which continues into the solar wind (6), and a nightside magnetospheric field line (7) which can swing back to the dayside (2) where the process can repeat. Adapted from *Dungey* (1961)

Reconnection occurs when the frozen in flux condition breaks down (*Hughes*, 1995). The simplest model of reconnection is the Sweet-Parker model, which is illustrated by Figure 1.5.

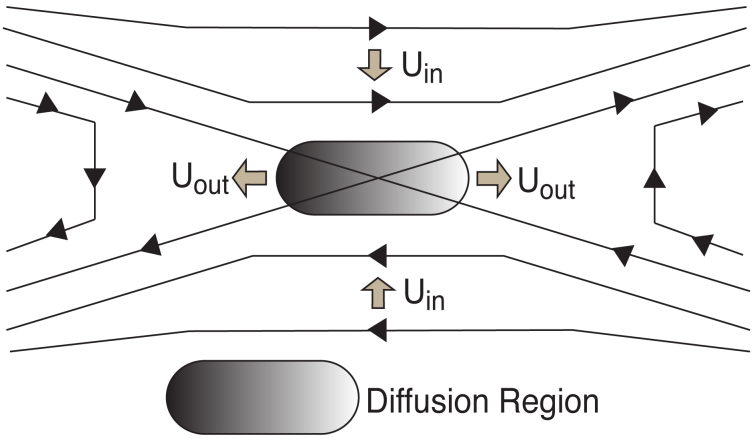

Figure 1.5: The Sweet-Parker model of reconnection (*Gurnett and Bhattacharjee*, 2005).

In the Sweet-Parker model of magnetic reconnection, there is a region in the center of the X-line where the frozen field condition breaks down, called the diffusion region (*Hughes*, 1995). The outflow velocity U_{out} is twice the Alfvèn speed of the inflowing plasma (*Hughes*, 1995).

Magnetic reconnection can also occur when the IMF has other orientations. When the IMF is oriented in an east-west direction, reconnection occurs on the flanks of the Earth's magnetosphere, which will skew the resulting magnetospheric convection patterns either in the east or the west (*Friis-Christensen and Wilhjelm*, 1975). When the IMF is oriented northward, the IMF and the Earth's magnetic field are anti-parallel on lobe field lines on the night side of the cusp of the magnetosphere, where the magnetic field lines enter and exit the poles (*Dorelli et al.*, 2007). This reconnection orientation is shown by Figure 1.6.

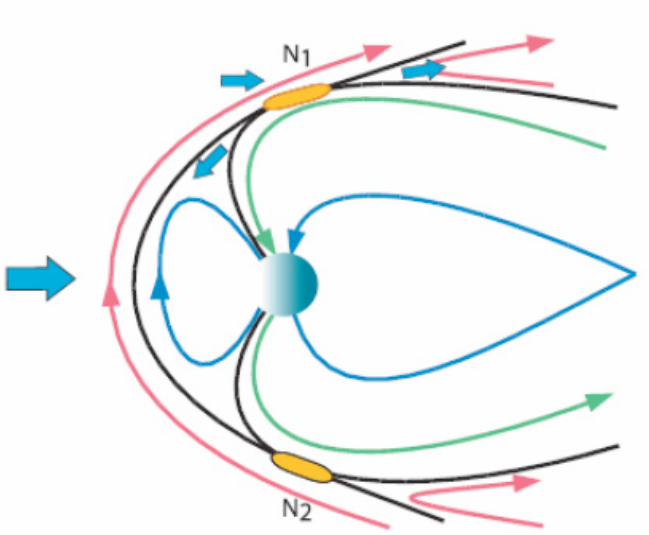

Figure 1.6: Reconnection at high latitudes for northward IMF. N1 and N2 are the points where the diffusion regions exist, the red field lines are the IMF, and the blue and green lines are the Earth's magnetic field. From *Dorelli et al.* (2007)

One stark difference between northward and southward IMF is that there separate merging points between the IMF and the magnetosphere in each hemisphere under northward IMF, while there is one around the equatorial dayside under southward IMF. Having merging at a separate point for each hemisphere, as in Figure 1.6, could lead asymmetries during periods around solstice where there is a strong dipole tilt. It has been hypothesized in the past that near solstice, direct magnetic merging between lobe field lines and the IMF only occurs in the summer hemisphere (*Crooker*, 1992; *Watanabe et al.*, 2005, 2006). Figure 1.7 shows hypothetical cartoons of the magnetic field configuration for northward IMF and (a) equinox conditions and (b) solstice or strong IMF B_X conditions. For equinox conditions, the reconnection geometry is the same as in Figure 1.6. For solstice conditions, the picture becomes more complicated. Direct magnetic merging only occurs in the summer (northern) hemisphere (Figure 1.7a), and the resultant field line geometry includes lobe field

lines from the northern hemisphere which drape over the dayside magnetipause to merge with lobe field lines in the southern hemisphere (Figure 1.7b). This results in new dayside magnetic flux tubes (Figure 1.7c). This process is sometimes referred to as "internal reconnection" and its signatures have been observed empirically by *Watanabe et al.* (2006). These different modes of magnetic merging under Northward IMF could have an impact on the observed coupling between the Solar Wind, Magnetosphere and Ionosphere.

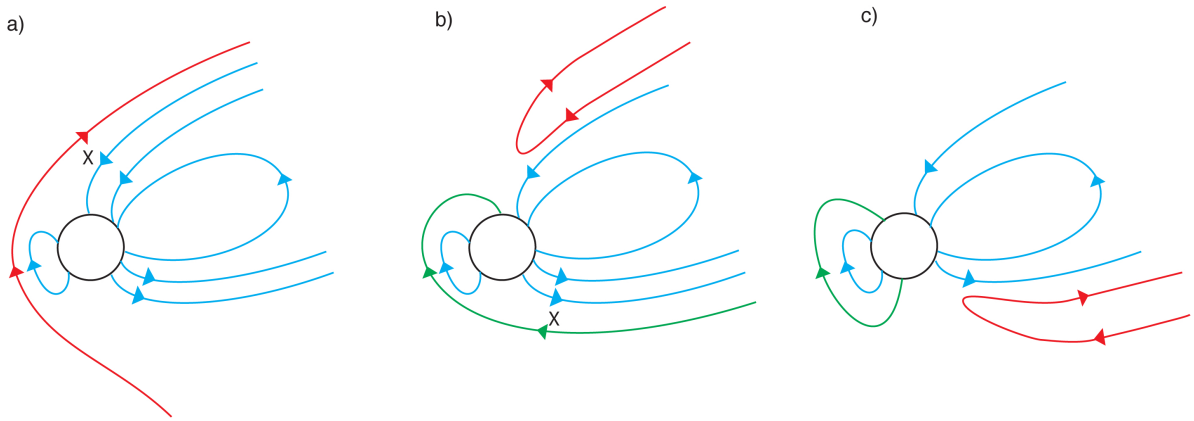

Figure 1.7: Possible reconnection configuration under northward IMF during northern hemisphere summer conditions. (a) The IMF field line (red) bends over the magnetosphere (blue), with merging occuring at the point marked by the 'x.' (b) The result of the merging in (a), with an IMF field line (red) which continues into the solar wind, and an over-draped field line (green) which internally reconnects with the magnetospheric field at the point marked by the 'x.' (c) The result of the internal reconnection in (b), with an IMF field line (red) that continues into the solar wind, and a new dayside closed field line (green).

1.2.2 Viscous Interactions

Another mechanism thought to influence magnetospheric plasma convection is a viscous-like interaction between the solar wind and the Earth's magnetosphere (*Axford and Hines*, 1961). When a viscous fluid flows over a solid boundary, the viscous effects are confined to a thin layer close to the solid body surface called the

"boundary layer" (*Karemcheti*, 1966). Since the velocity at the surface must have a limiting value of zero, but the fluid has non-zero velocity, the boundary layer is an unstable region where the velocity increases rapidly (*Karemcheti*, 1966).

In the magnetosphere, shocked solar wind flows over the surface in a region called the magnetosheath as in Figure 1.3. The magnetosheath plasma has a viscous-like interaction with the magnetosphere, in which a boundary layer is formed (*Sckopke et al.*, 1981). Unlike a fluid flowing over a solid body, the boundary layer of the magnetosphere will have an induced drag, which causes circulation of plasma throughout the magnetosphere (*Sckopke et al.*, 1981). The higher density region of the boundary layer carries instabilities within it. These are predominantly thought to be what is called the Kelvin-Helmholtz instability (*Kivelson*, 1995). This interaction is analogous to wind blowing over water, driving movement and ripples on the surface.

The viscous drag resulting in the boundary layer drives circulation of plasma throughout the entire magnetosphere (*Axford and Hines*, 1961). The resulting plasma motion is shown in Figure 1.8.

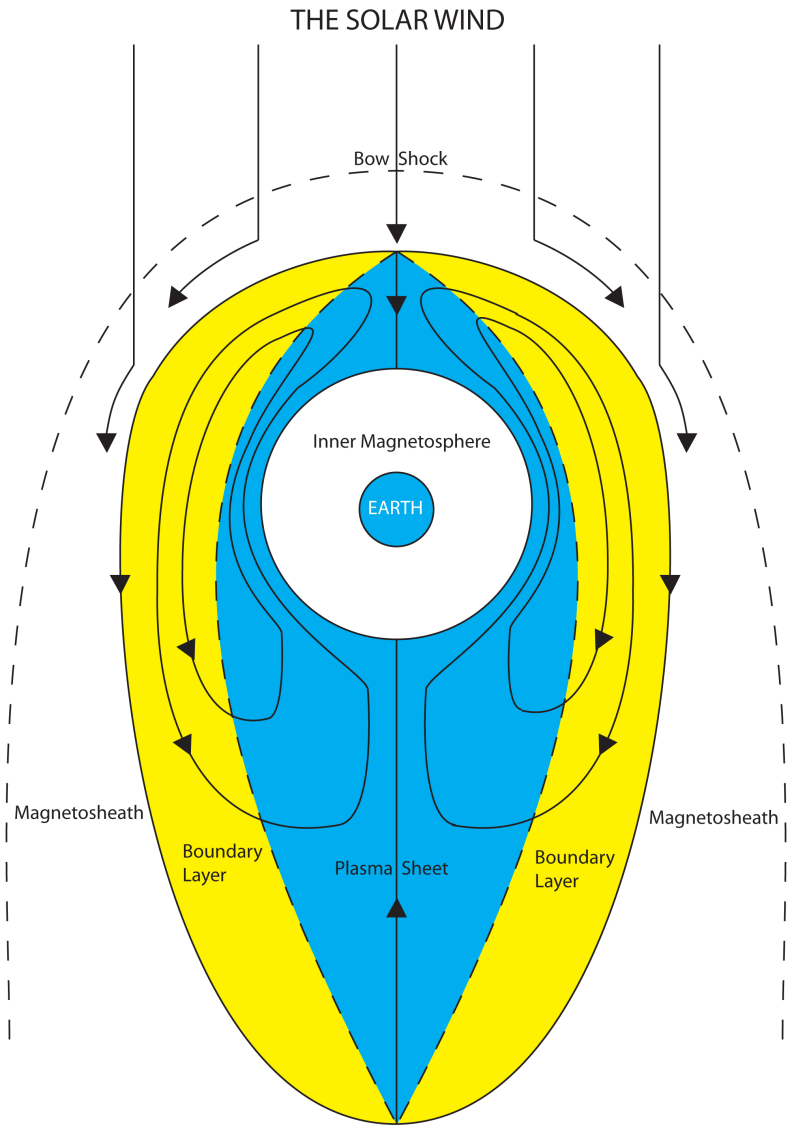

Figure 1.8: Plasma convection in the magnetosphere driven by viscous-like interactions (*Axford and Hines*, 1961)

1.3 The Earth's Ionosphere

The convection in the magnetosphere maps along equipotential field lines into the polar ionosphere. In order to understand how this coupling works, it is crucial to understand the electrodynamics in the high latitude ionosphere. Most importantly, one must understand how the ionospheric plasma is formed, and how the interaction

of particles effects its conductivity.

1.3.1 Formation of the Ionosphere

The main mechanisms for ionization in the Earth's upper atmosphere are photoionization and particle precipitation. With photoionization, high energy UV photons collide with molecules to separate electrons from the nucleus. The three primary photoionization reactions are given by Equations (1.9) through (1.11) (*Rees*, 1989).

$$N_2 + h\nu(< 796\mathring{A}) \longrightarrow N_2^+ + e^- \tag{1.9}$$

$$O_2 + h\nu(< 1026\mathring{A}) \longrightarrow O_2^+ + e^- \tag{1.10}$$

$$O + h\nu(< 911\mathring{A}) \longrightarrow O^+ + e^- \tag{1.11}$$

Where the photon wavelength corresponds to the ionization threshold from the molecule's ground state (*Rees*, 1989). These ions can also collide to form other ions, such as NO^+ (*Carlson and Egeland*, 1995). Another ionization mechanism is the impact of "energetic" electrons, usually with energy greater than 1 keV, precipitating along magnetic field lines from the magnetosphere (*Luhmann*, 1995). Ions can also be lost due to various forms of recombination (*Luhmann*, 1995).

The ionosphere is often categorized in three layers, based on the density of ions and electrons in the gas. These are the D (altitude below 90km), E (altitude between 90 and 130 km) and F (altitude above 130 km) regions (*Luhmann*, 1995). These regions are listed in order of increasing charged particle density.

1.3.2 Ionospheric Conductivity

Collisions between ions and neutrals limit the speed of ions while the electrons can move unimpeded. Thus, electric currents can be induced in the ionosphere. It

is well known that the ionosphere has anisotropic conductivity, which can be seen in the ionospheric Ohm's law, given by equation (1.12) (*Richmond and Thayer*, 2000).

$$\mathbf{J} = \sigma_P \mathbf{E}_\perp + \sigma_H \mathbf{b} \times \mathbf{E}_\perp + \sigma_\parallel \mathbf{E}_\parallel \mathbf{b} \tag{1.12}$$

Where $\mathbf{E}$ is the ionospheric electric field, and $\mathbf{b}$ is a unit vector in the direction of the Earth's geomagnetic field. The subscripts $\perp$ and $\parallel$ indicate components perpendicular to and parallel to the geomagnetic field, respectively. σ_P, σ_H, and $\sigma_\parallel$ are called the Pederson, Hall and parallel conductivities respectively. As can be seen in Figure 1.10, the Pederson current, $\mathbf{J}_P$, is in the direction of the polar cap electric field and the Hall Current, $\mathbf{J}_H$, is in the opposite direction of plasma convection in the ionosphere. The expression for the conductivity components are given by equations (1.13) through (1.15) (*Richmond and Thayer*, 2000).

$$\sigma_\parallel = \frac{N_e e^2}{m_e \left(\nu_{en\parallel} + \nu_{ei\parallel}\right)} \tag{1.13}$$

$$\sigma_P = \frac{N_e e}{B}\left(\frac{\nu_{in}\Omega_i}{\nu_{in}^2 + \Omega_i^2} + \frac{\nu_{en\perp}\Omega_e}{\nu_{en\perp}^2 + \Omega_e^2}\right) \tag{1.14}$$

$$\sigma_H = \frac{N_e e}{B}\left(\frac{\Omega_e^2}{\nu_{en\perp}^2 + \Omega_e^2} - \frac{\Omega_i^2}{\nu_{in}^2 + \Omega_i^2}\right) \tag{1.15}$$

Where N_e is the ionospheric electron density; e is the electron charge; B is the magnetic field magnitude; Ω_j is the frequency at which a charged particle of species j gyrates around a magnetic field line and is called the cyclotron frequency; ν_{jk} is the collision frequency between particle species j and k; the subscripts $\perp$ and $\parallel$ correspond to directions perpendicular to and parallel to the geomagnetic field respectively; and the subscripts i, e, and n correspond to the ions, electrons and neutral molecules respectively. A full derivation of Equations (1.13) through (1.15) can be found in *Richmond and Thayer* (2000).

As can be seen from Equations (1.14) and (1.15), if the collision frequency between charged particles and neutrals is much smaller than their cyclotron frequency, the Hall conductivity becomes zero. Therefore, at higher altitudes such as the F-region where the charged particle density is high, the Pederson conductivity will dominate.

Often, Ohm's law is written using a conductivity tensor given by Equations (1.16) and (1.17) (*Gurnett and Bhattacharjee*, 2005).

$$\mathbf{J} = \overleftrightarrow{\sigma}(\mathbf{E} + \mathbf{v} \times \mathbf{B}) \tag{1.16}$$

$$\overleftrightarrow{\sigma} = \begin{bmatrix} \sigma_P & \sigma_H & 0 \\ -\sigma_H & \sigma_P & 0 \\ 0 & 0 & \sigma_\parallel \end{bmatrix} \tag{1.17}$$

Understanding how currents are directed through the ionosphere is crucial to understanding the coupling between the solar wind, magnetosphere and ionosphere.

1.4 Magnetosphere-Ionosphere Coupling

1.4.1 Field Aligned Currents

The Earth's ionosphere, being a conducting plasma, can have electrodynamic interactions with the magnetosphere. The electric field in the ionosphere can thus be used as a metric of how much energy is transferred in the solar wind-magnetosphere-ionosphere system.

The Earth's magnetic field lines are directed out of the south pole and into the north pole. When a large scale interaction such as magnetic reconnection with the solar wind occurs, the movement of the magnetic field lines and the resulting plasma convection will be mapped to the high latitude ionosphere (*Dungey*, 1961). This

is shown in Figure 1.9, where the high latitude trace lines correspond to magnetic field lines being pulled along the center of the magnetosphere back to the Earth on the night side (*Dungey*, 1961). A similar convection pattern arises in the absence of reconnection due to viscous-like interactions (*Axford and Hines*, 1961).

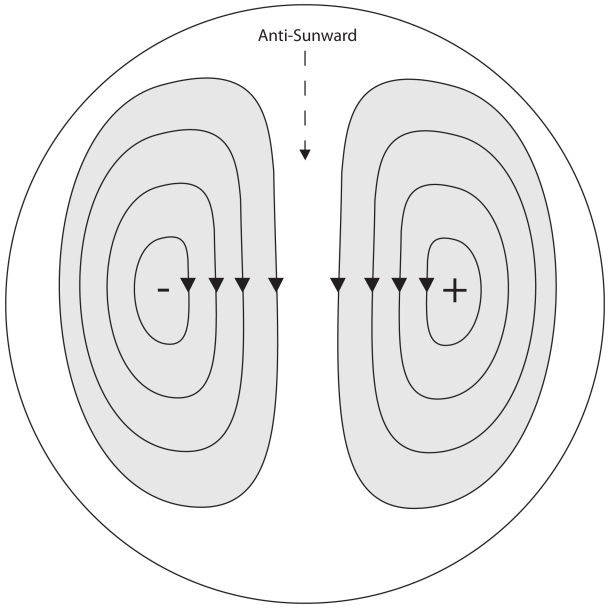

Figure 1.9: The streamlines of ionospheric convection as a result of magnetic reconnection (*Dungey*, 1961). The picture is viewed from above the north magnetic pole looking down. The top of the figure is local noon.

The convection shown in Figure 1.9 is associated with a phenomenon called "field-aligned currents" (FACs). Since magnetic field lines can be approximated as good conductors (*Chen*, 1974), electric currents move along magnetic field lines into and out of the polar ionosphere called "region 1 currents," leading to a net electric field oriented across the polar cap. Although there are debates about small scale generation of field aligned currents, large-scale FACs are thought to result from magnetic reconnection, field-aligned vorticity, and the compression of plasma (*Friis-Christensen and Wilhjelm*, 1975; *Song and Lysak*, 1995).

When ionospheric plasma is in the presence of an electric field and a magnetic field, it will have a bulk drift velocity called the $\mathbf{E} \times \mathbf{B}$ drift, given by Equation (1.18) (*Chen*, 1974).

$$\mathbf{v}_{\mathbf{E}\times\mathbf{B}} = \frac{\mathbf{E} \times \mathbf{B}}{B^2} \tag{1.18}$$

Where $\mathbf{v}_{\mathbf{E}\times\mathbf{B}}$ is the drift velocity of the plasma particles and B is the magnitude of the magnetic field. In the northern hemisphere, the magnetic field is directed into the poles, and therefore the $\mathbf{E} \times \mathbf{B}$ drift of the Ionospheric plasma at high latitudes flows in the anti-sunward direction, or from local noon to local midnight. Applying this analysis to lower latitude field aligned currents that close the system known as "region 2 currents", one gets the opposite motion, resulting in the plasma flow vortices shown in Figure 1.10. Applying the same principles, there will be plasma flow vortices in the magnetosphere where the currents close as well.

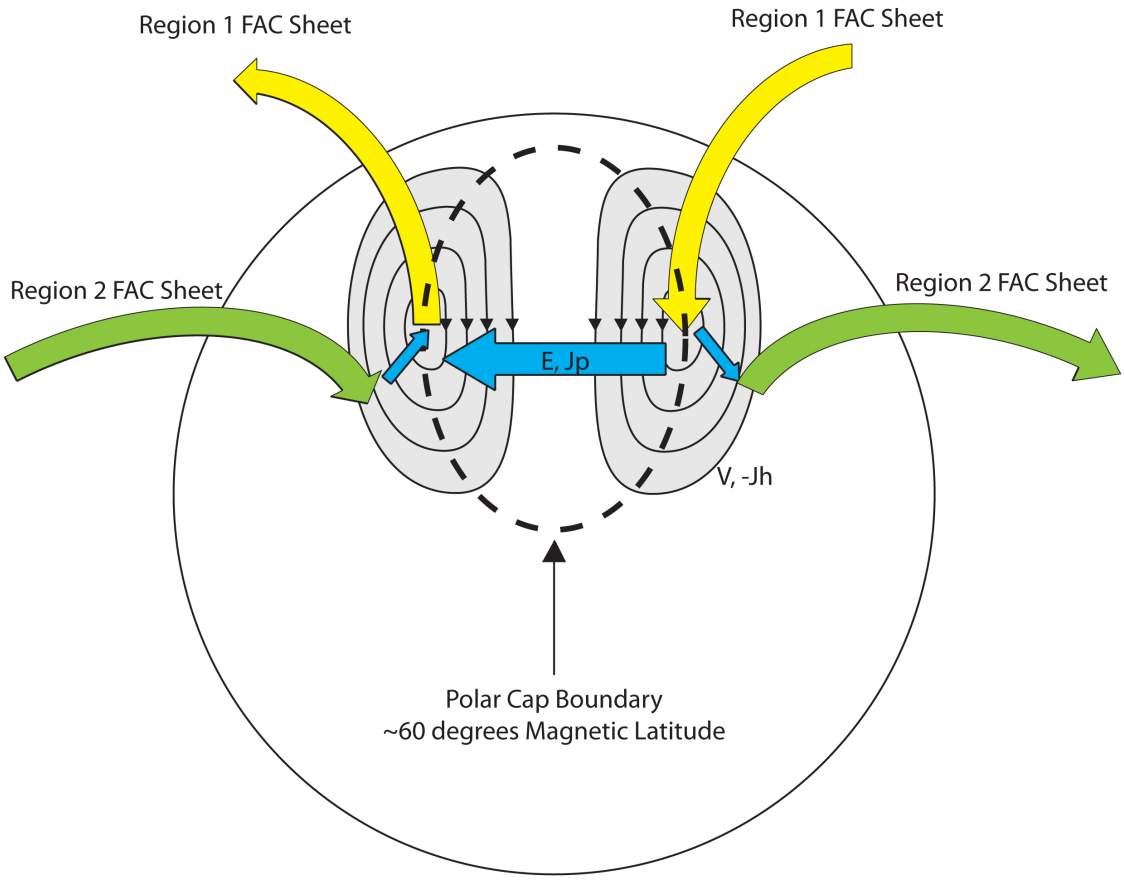

Figure 1.10: An illustration of the current systems coupling the magnetosphere and ionosphere under southward IMF. The yellow and green arrows are the region 1 and region 2 FACs, respectively. The blue arrows represent the polar cap electric field (E) and ionospheric Pederson currents (Jp). The black streamlines represent the plasma convection velocity (V) as well as the opposite direction of the ionospheric Hall currents (Jh). The dashed line represents the polar cap boundary.

It has been known for quite some time that different orientations of the IMF will result in different FAC systems. *Friis-Christensen and Wilhjelm* (1975) demonstrated that there are different current systems and convection patterns in the polar cap ionosphere depending on the orientation of the IMF in the Y-Z plane. When

the IMF Z component is negative (southward IMF), the two cell pattern shown in Figures 1.9 and 1.10 occurs. When the IMF Z component is zero, and there is a non-zero IMF Y component, then the convection pattern is skewed in either an east or west direction. These skewed patterns are associated with what *Friis-Christensen and Wilhjelm* (1975) termed the "DPY" currents. When the IMF Z component is positive, a new set of FACs form due to reconnection on the nightside of the cusp which close into the ionosphere on the dayside high latitude. These FACs were termed "NBZ" by *Iijima et al.* (1984).

When the IMF is oriented northward and the NBZ currents are generated, the current system is more complicated and is shown in Figure 1.11. Region 1 and 2 currents still feed into the ionosphere due to viscous-like interactions, but they are further coupled with the NBZ currents to generate a four cell convection pattern, with two high latitude convection cells exhibiting sunward convection in the center, sometimes called "reverse convection" (*Crooker*, 1992).

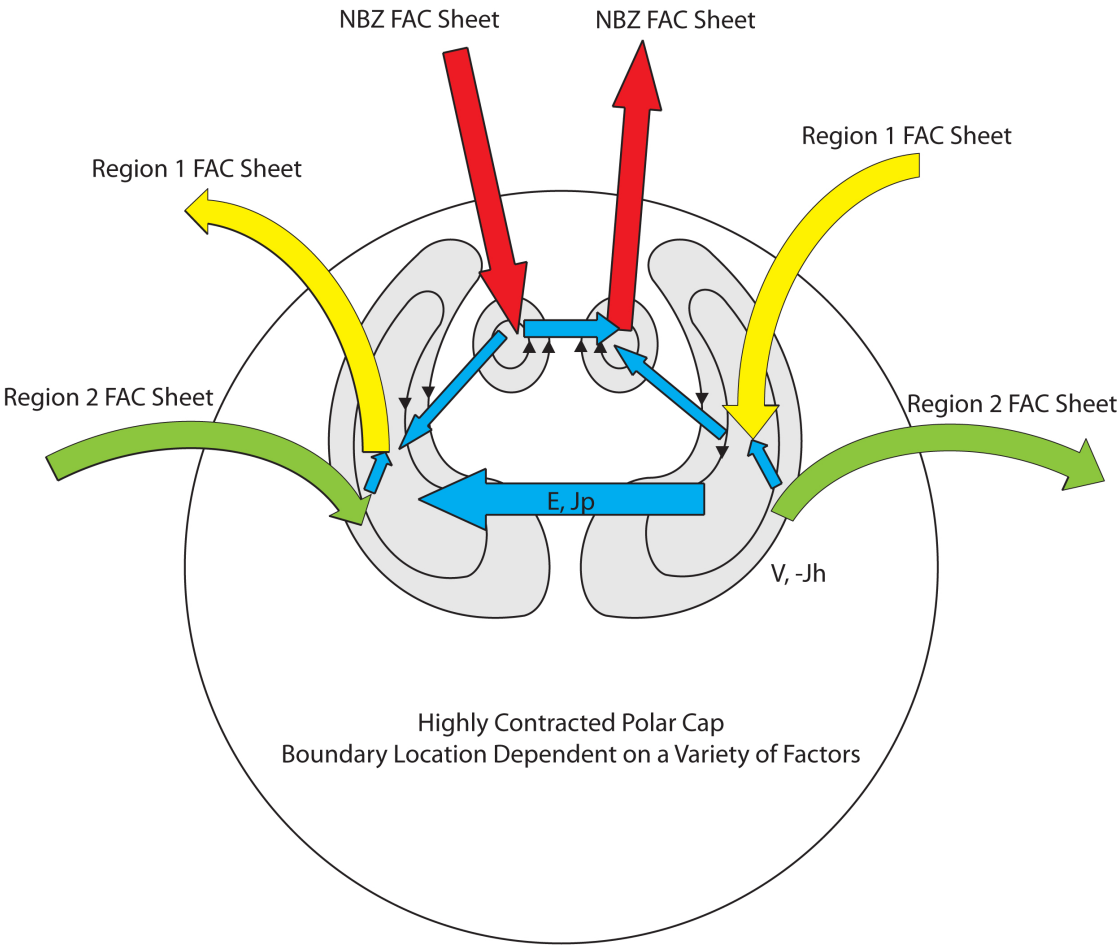

Figure 1.11: An illustration of the current systems coupling the magnetosphere and ionosphere under northward IMF. The red, yellow and green arrows are the NBZ, Region 1 and Region 2 FACs, respectively. The blue arrows represent the polar cap electric field (E) and ionospheric Pederson currents (Jp). The black streamlines represent the plasma convection velocity (V) as well as the opposite direction of the ionospheric Hall currents (Jh).

In summary, the field-aligned currents associated with various IMF orientations are shown in Figure 1.12, taken from *Weimer* (2001b). For northward IMF, the NBZ currents as well as the Region 1 and 2 currents due to viscous-like interactions can be seen, with skewing in the east or west direction when the IMF-Y component is non-zero.

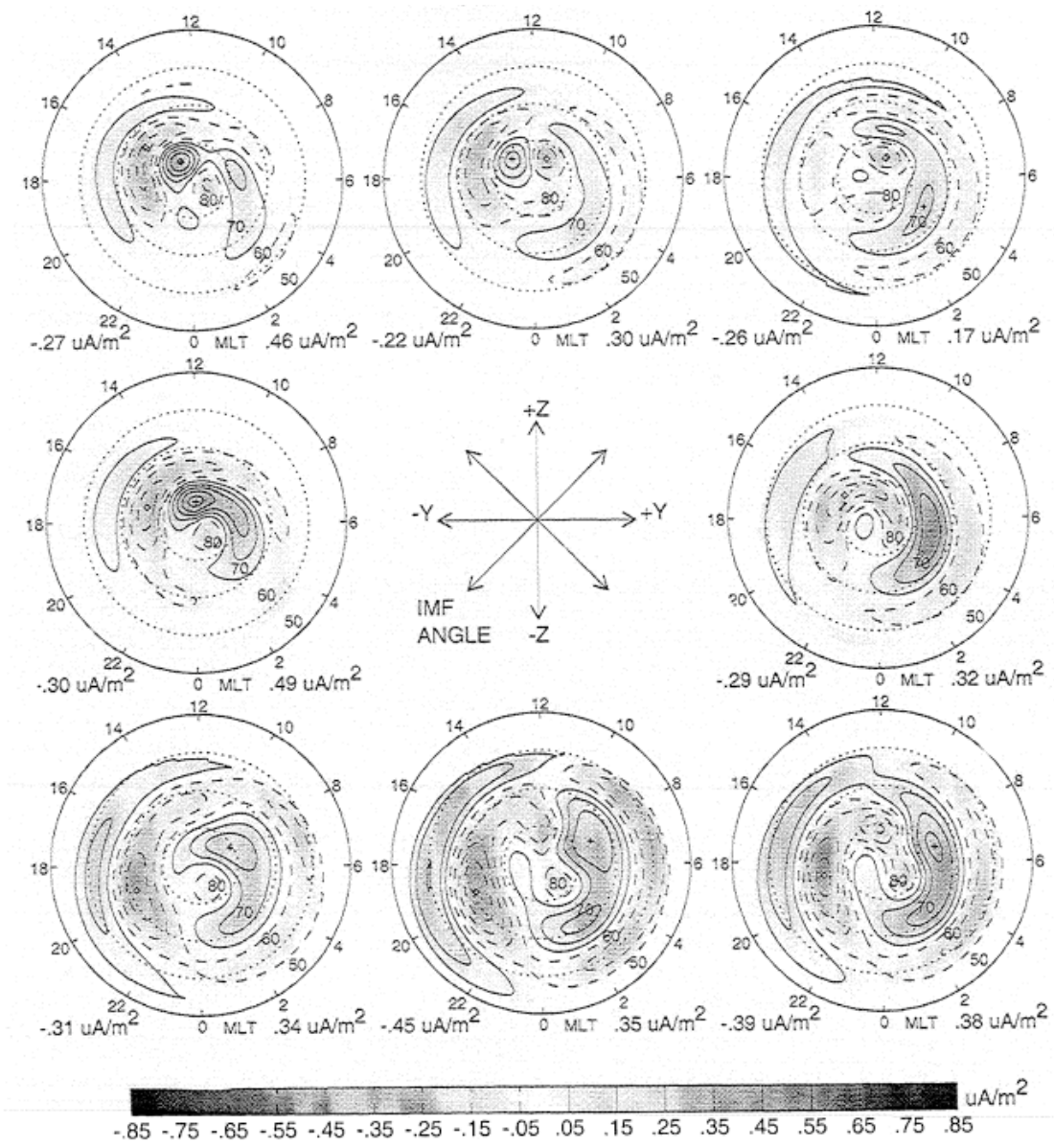

Figure 1.12: Field aligned current maps in the polar ionosphere based on eight different IMF orientations in the Y-Z plane. "The magnitude of the IMF in the GSM Y-Z plane B_T is fixed at 5nT, the solar wind velocity V_{SW} is $400 kms^{-1}$... contours around negative currents are drawn with dashed lines, and solid lines are used for positive currents, with the convention that positive currents are into the ionosphere. The magnitude of the current is also indicated with the intensity of the grey scale shading"(*Weimer*, 2001b).

1.4.2 The Cross Polar Cap Potential

Because convecting plasma in a magnetic field has an associated electric field, and because the Earth's magnetic field can largely be assumed to be static, an ionospheric electric potential pattern [$\mathbf{E} = -\nabla\Phi$] is generated. The potential drop across the polar ionosphere is called the cross polar cap potential, Φ_{PC}, and is an important metric in the solar wind-magnetosphere-ionosphere system.

In the case of reconnection with southward IMF as well as viscous-like interactions, the electrodynamic coupling between the magnetosphere and ionosphere can be seen in Figure 1.10. At high altitudes, Pederson currents close the current in the ionosphere, related by Ohm's law to the electric field. If the over-all geomagnetic field is assumed to be static, then $\nabla \times \mathbf{E} = 0$ and the electric field can be expressed as the negative gradient of a potential, Φ (*Jackson*, 1975). The drift velocity of the ionospheric plasma can then be expressed by Equation (1.19).

$$\mathbf{v} = -\frac{\nabla\Phi \times \mathbf{B}}{B} \tag{1.19}$$

It can be seen from Equation (1.19) that Φ is a stream-function of $\mathbf{v}$. It follows that equipotential lines given by [$\Phi = constant$] represent streamlines of ionospheric plasma flow (*Wolf*, 1995; *Reiff and Luhmann*, 1986). A more detailed discussion of streamlines and stream-functions can be found in *Karemcheti* (1966).

For a long time, it was thought that when the IMF was oriented northward, reconnection didn't occur and the magnetosphere system "shut off," making the coupling a half wave rectifier. It was later found that when the IMF is northward, two additional convection vortices appear on the dayside at high latitudes with reversed sunward convection near noon due to magnetic reconnection at the cusp (*Crooker*, 1992). The typical pattern that arises is shown in Figure 1.13. The potential across

the reverse convection vortices on the dayside will be hereafter referred to as the "reverse convection potential," or Φ_{RC}. The potential across the two larger cells due to viscous interaction will be hereafter referred to as the "viscous potential." The streamlines-as-equipotentials approximation still holds for the convection pattern under northward IMF.

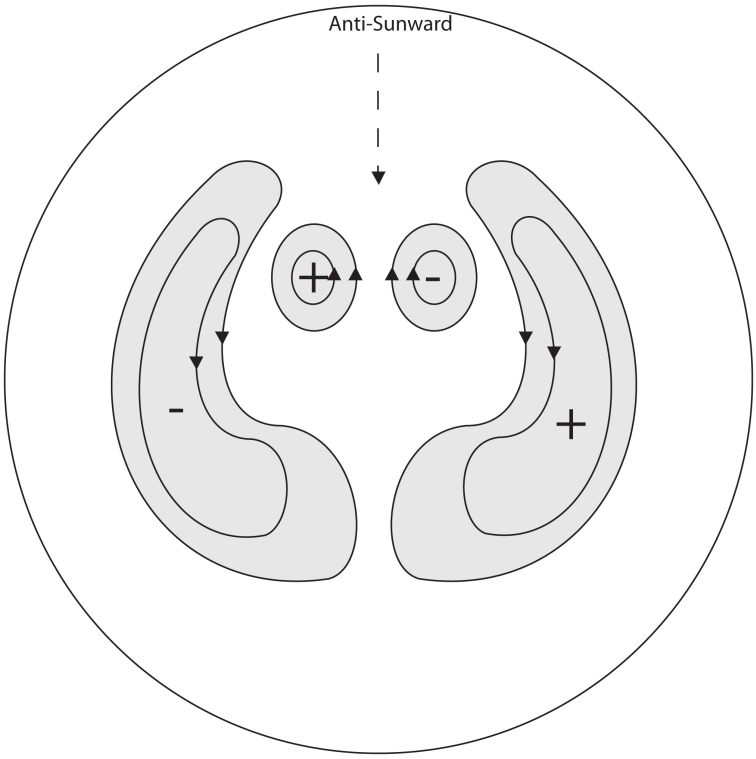

Figure 1.13: An illustration of the convection pattern under northward IMF. The larger cells are the background convection pattern due to viscous-like interactions, and the smaller high latitude cells are due to reconnection near the cusp.

Further, under northward IMF at solstice, it has been proposed that reconnection operates differently between the winter and summer hemisphere, as in Figure 1.7. This can impact the reverse convection pattern under northward IMF. Figure 1.14 shows the different type of reverse convection cells for (a) summer and (b) winter. The dotted lines are the open-closed magnetic field line boundary, and the dashed

lines indicate regions of magnetosheath ion precipitation. The important thing to note is that in the winter, there is circulation on closed field lines (through what is referred to as "reciprocal" cells). These reciprocal cells are thought to be due to internal reconnection (*Watanabe et al.*, 2005, 2006). The impact that these different forms of reverse convection will have on the reverse convection potential has yet to be determined.

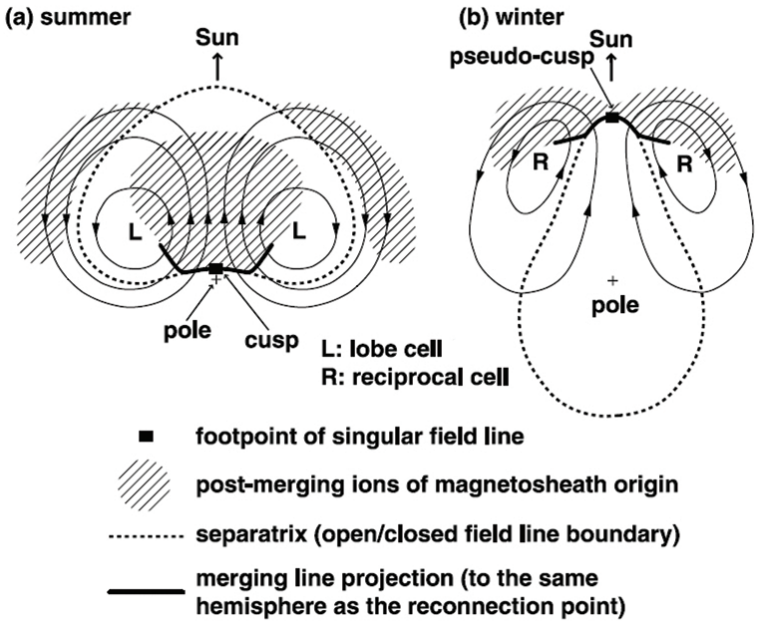

Figure 1.14: Edited from *Watanabe et al.* (2006).

1.5 Cross Polar Cap Potential Saturation

It was originally thought that when the IMF turned increasingly southward, Φ_{PC} would increase linearly with the interplanetary electric field (IEF). The idea was that a fraction of the solar wind electric field would be impressed upon the magnetosphere, generating a magnetospheric convection potential, Φ_m. This large scale potential would then map along magnetic field lines into the polar ionosphere, with Φ_{PC} being approximately equal to Φ_m (*Hill et al.*, 1976; *Reiff and Luhmann*, 1986; *Siscoe et al.*,

2002b).

Linear models of the polar cap potential tended to work fairly well, except that they would over-predict the value of the polar cap potential when the IEF was greater than approximately 3 mV/m (*Reiff et al.*, 1981). This tendency for the polar cap potential to approach a limiting value was referred to as cross-polar cap potential "saturation." The basic equation for polar cap potential saturation is given by Equation (1.20) (*Siscoe et al.*, 2002b).

$$\Phi_{PC} = \frac{\Phi_m \Phi_S}{\Phi_m + \Phi_S} \tag{1.20}$$

Where Φ_m is the potential across the magnetosphere and Φ_S is called the "saturation potential." When $\Phi_m << \Phi_S$, then the polar cap potential is approximately equal to the magnetospheric potential. When $\Phi_m >> \Phi_S$, the polar cap potential will be approximately equal to the saturation potential. Empirical studies using both satellite and ground-based data have demonstrated the saturation model to be more accurate than the linear model, with Φ_S found to be between 100 and 200 kV (*Siscoe et al.*, 2002b; *Shepherd et al.*, 2002; *Hairston et al.*, 2003, 2005; *Russel et al.*, 2001). An example set of measurements that demonstrates polar cap potential saturation is given by Figure 1.15. Several hypothetical models for the saturation of the polar cap potential have been presented based on both theoretical calculations and MHD simulations.

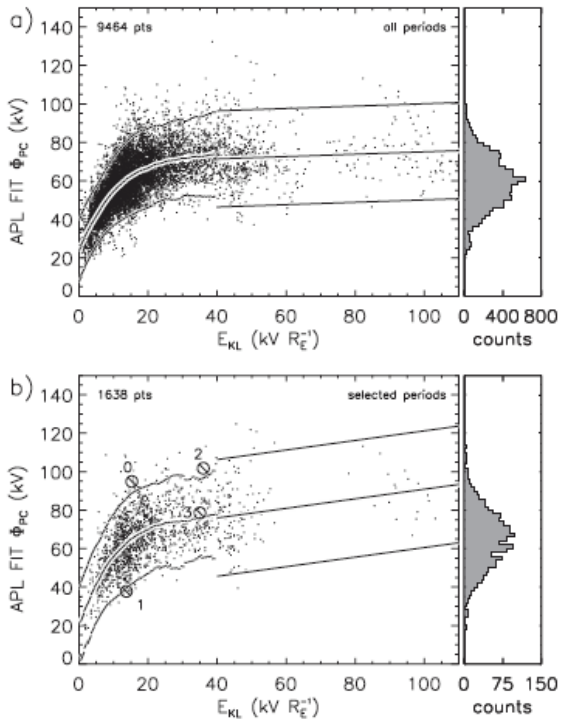

Figure 1.15: A demonstration of Φ_{PC} saturation as a function of E_{KL}, a coupling metric which represents the portion of the interplanetary electric field (IEF) which is coupled into the magnetosphere via reconnection. APL FIT is the technique used by the dataset known as the SuperDARN radar to determine the potential across the polar cap (explained in detail in Chapter 3). "Counts" demonstrates the number of measurements at each polar cap potential value. From *Shepherd et al.* (2002).

1.5.1 The Siscoe-Hill Model of Polar Cap Potential Saturation

The oldest and most commonly referenced hypothesis for polar cap potential saturation is the Hill model, first presented by *Hill et al.* (1976). In the Hill model, a feedback mechanism via the region 1 field aligned currents is what causes the polar cap potential to saturate. The region 1 currents generate a magnetic field which opposes the Earth's magnetic field at the dayside magnetopause. As the region 1 currents increase in strength, the Earth's magnetic field becomes increasingly weakened to the point where the region 1 currents reach a threshold, I_s, where the

reconnection rate and the polar cap potential saturate.

During this saturation regime, the solar wind-magnetosphere-ionosphere becomes like a current generator with an internal resistance (the solar wind-magnetosphere dynamo) driving an external resistance (the ionosphere), with a linear current-voltage relationship given by (1.21) (*Siscoe et al.*, 2002b).

$$\Phi_{PC} = \Phi_M - (\frac{\Phi_M}{I_S})I_1 \tag{1.21}$$

Where I_1 is the strength of the region 1 currents. *Siscoe et al.* (2002b) tested and verified the Hill model using MHD simulations, and expanded on it theoretically to obtain an expression for the polar cap potential based on solar wind parameters. Using the Biot-Savart law to determine the strength of I_S needed to saturate the polar cap, as well as empirical formulae for the reconnection rate at the magnetopause, they showed that the polar cap potential could be expressed by (1.22) (*Siscoe et al.*, 2002b).

$$\Phi_{PC} = \frac{57.6 E_{SW} p_{SW}^{1/3} D^{4/3} F(\theta)}{p_{SW}^{1/2} D + 0.0125 \zeta \Sigma_0 E_{SW} F(\theta)} \tag{1.22}$$

Where E_{SW} is the magnitude of the IEF, p_{SW} is the solar wind dynamic pressure, D is the Earth's dipole field scaled to its present value, $F(\theta)$ is a geometric coupling factor based on the orientation of the IMF in the y-z plane, θ is the IMF clock angle in the y-z plane, ζ is an empirically derived scaling factor based on the geometry of the region 1 currents, and Σ_0 is the height-integrated Pederson conductivity.

Siscoe et al. (2002a) traced region 1 FACs in MHD simulations of polar cap potential saturation to the bow shock of the solar wind. They found that when the region 1 currents are strong enough to saturate the polar cap, they usurp the Chapman-Ferraro currents as the standoff against solar wind dynamic pressure. Ac-

cording to this update to the Siscoe-Hill model of polar cap potential saturation, the maximum region 1 current is the amount of current necessary to (1) provide the standoff with the solar wind dynamic pressure and (2) account for the magnetic shear between the IMF (which is southward) and the magnetotail (which is in the sunward/anti-sunward direction).

There are several other models of polar cap potential saturation which are subtly different than the Siscoe-Hill model, but make the same overall predictions of the region 1 current system limiting the reconnection rate on the dayside (*Siscoe et al.*, 2004).

1.5.2 The Alfvèn Wing Model

Another model for polar cap potential saturation was first proposed by *Ridley* (2007) and expanded upon by *Kivelson and Ridley* (2008). This model is commonly called the "Alfvèn wing" model. The argument begins with the fact that, by equation (1.7), as the IMF magnitude increases, the Alfvèn speed increases while the Alfvènic Mach number decreases.

In order to understand what happens as a sub-Alfvènic plasma passes a conducting body, one can look to the moons of Jupiter. The Galileian satellites Io and Ganymede are embedded in plasma co-rotating with Jupiter within its magnetosphere (*Kopp and Ip*, 2002; *Ip and Kopp*, 2002). As a result, when the sub-Alfvènic plasma containing a frozen-in magnetic field encounters these obstacles, the magnetic field bends and Alfvèn waves are launched along magnetic field lines. The combination of a bent magnetic field and Alfvèn waves forms tubes of plasma above and below the satellite where the flow characteristics are significantly altered. These tubes are called "Alfvèn wings" (*Neubauer*, 1980; *Linker et al.*, 1998). It should be

noted that in the original formulation of the Alfvèn wing problem, it was assumed that $M_A << 1$ (*Drell et al.*, 1965).

Ridley (2007) used the BATS-R-US MHD code to demonstrate that when M_A in the solar wind dropped significantly, Alfvèn wings could form at the Earth's magnetosphere as well. Figure 1.16 show's a diagram of what Alfvèn wings might look like at the Earth's magnetosphere. The tail of the magnetosphere has split and formed into Alfvèn wings, and the IMF field lines are bent within the wings.

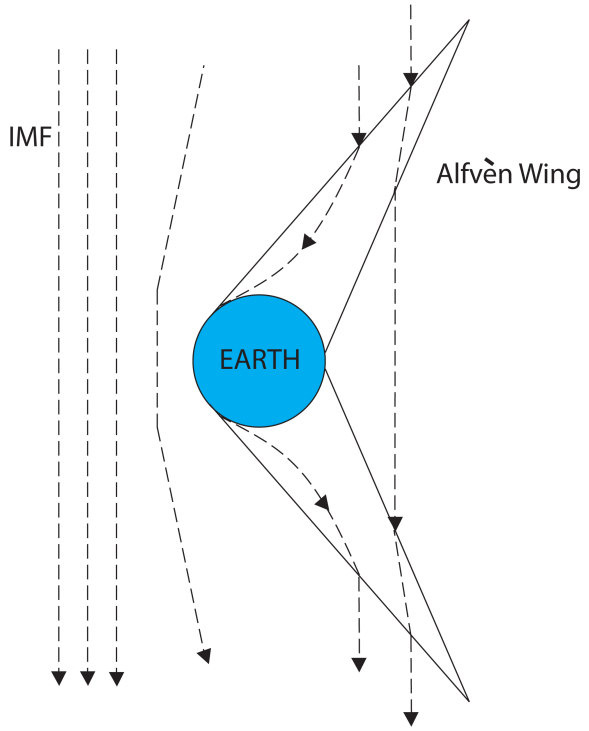

Figure 1.16: Alfvèn wings in the Earth's magnetosphere under Southward IMF conditions. The dashed lines are magnetic field lines, and the solid lines define the boundary of the Alfvèn wings.

The impact Alfvèn wings would have on the polar cap potential depends on their conductivity. *Neubauer* (1980) showed that the conductivity of an Alfvèn wing can be given by (1.23).

$$\Sigma_A = (\mu_0 V_A)^{-1} \tag{1.23}$$

Where Σ_A is the Alfvèn wing conductivity and V_A is the Alfvèn speed of the plasma passing by the conducting obstacle. *Kivelson and Ridley* (2008) deals with the partial reflection of the reconnection electric field by the polar ionosphere. When a normally incident Alfvèn wave changes impedance from Σ_A to Σ_P, the electric field partially reflects, with a transmission coefficient given by (1.24) (*Kivelson and Ridley*, 2008).

$$Q_A = \frac{\Sigma_A}{\Sigma_A + \Sigma_P} \tag{1.24}$$

Where Q_A is half the transmission coefficient. Thus, the transmitted field for an incident field, E_i, is given by $E_t = 2Q_A E_i$. The formulation for the polar cap potential using Alfvèn wing arguments is therefore given by (1.25) (*Kivelson and Ridley*, 2008).

$$\Phi_{PC} = \frac{2E_{SW}^R D \Sigma_A}{\Sigma_P + \Sigma_A} \tag{1.25}$$

Where E_{SW}^R is the effective IEF which merges into the magnetosphere via reconnection and D is the reconnection line length.

1.5.3 The Sheath Control Mechanism

As discussed in section 1.2, the solar wind is usually at a speed several times larger than its magnetosonic speed. When it encounters the Earth's magnetic field, it is decelerated and compressed, forming a shock (*Burgess*, 1995). The shocked solar wind then flows around the Earth's magnetosphere in a region called the magnetosheath. It is in the magnetosheath that reconnection occurs. In recent years, a

hypothesis has been proposed that when the polar cap potential saturates, it is due to the dynamics of the sheath limiting the reconnection rate (*Lopez et al.*, 2010).

In order to understand the dynamics of the sheath, the behavior of the bow shock must be understood. No matter what the structure of the shock, it is well known that mass, energy and momentum must be conserved. The electromagnetic boundary conditions which are a consequence of Maxwell's equations must also be met. These conditions are sometimes called the "MHD jump conditions" (*Burgess*, 1995). Using the governing equations for MHD and the conservation relations across the shock, the MHD jump conditions are given by (1.26) through (1.31) (*Burgess*, 1995).

$$[\rho u_n] = 0 \tag{1.26}$$

$$[\rho u_n^2 + P + \frac{B^2}{2\mu_0}] = 0 \tag{1.27}$$

$$[\rho u_n \mathbf{u}_t - \frac{B_n}{\mu_0}\mathbf{B}_t] = 0 \tag{1.28}$$

$$[\rho u_n(\frac{1}{2}u^2 + \frac{\gamma}{\gamma-1}\frac{P}{\rho}) + u_n\frac{B^2}{\mu_0} - \mathbf{u}\cdot\mathbf{B}\frac{B_n}{\mu_0}] = 0 \tag{1.29}$$

$$[B_n] = 0 \tag{1.30}$$

$$[u_n\mathbf{B}_t - B_n\mathbf{u}_t] = 0 \tag{1.31}$$

Where ρ is the plasma density, u_n is the velocity component normal to the shock surface, $\mathbf{u}_t$ is the velocity component transverse to the shock normal, P is the plasma thermal pressure, B is the magnitude of the magnetic field, B_n is the component of the magnetic field normal to the shock, $\mathbf{B}_t$ is the component of the magnetic field transverse to the shock normal, and γ is related to the number of degrees of freedom in the plasma. The operator, $[F] = F_u - F_d$, corresponds to the difference between

the upstream and downstream values of parameter, F. This assumes that the shock structure is like a "black box" and that the plasma both upstream and downstream of the shock has an adiabatic equation of state ($P\rho^{-\gamma} = constant$) (*Burgess*, 1995).

Often, shocks are classified by the orientation of the frozen in magnetic field of the upstream plasma with respect to the shock normal. For the exactly perpendicular shock, if one assumes the plasma velocity is parallel to the shock normal, then plasma parameters in the magnetosheath can be related to parameters in the solar wind by (1.32) through (1.36) (*Burgess*, 1995).

$$(r-1)\{r^2\frac{2-\gamma}{M_A^2} + r(\frac{\gamma}{M_A^2} + \frac{2}{M_{CS}^2} + \gamma - 1) - (\gamma+1)\} = 0 \tag{1.32}$$

$$P_s = \rho_0 V_0^2(1-\frac{1}{r}) + (1-r^2)\frac{B_0^2}{2\mu_0} + P_0 \tag{1.33}$$

$$B_s = rB_0 \tag{1.34}$$

$$\rho_s = r\rho_0 \tag{1.35}$$

$$V_s = \frac{1}{r}V_0 \tag{1.36}$$

Where r is called the "compression" ratio of the shock, and the subscripts "0" and "s" correspond to the values in the solar wind and magnetosheath, respectively. As the plasma is compressed over the bow shock, the density increases while the velocity decreases. The magnetic field also becomes stronger in the magnetosheath.

For a parallel shock, the magnetic field doesn't have an effect on the structure of the shock from a fluid perspective. The MHD jump conditions become conservation relations for a simple shock. While it would appear that the field is unchanged and doesn't effect the shock, there are still kinetic dissipation processes occuring that make the shock structure difficult to study (*Burgess*, 1995).

Figure 1.17 show's a possible configuration of currents and magnetic fields on the dayside magnetosphere, and the magnetosheath in particular. There is a magnetic shear across the bow shock as the plasma is compressed, which induces a current parallel to the shock. This current closes with the Chapman-Ferraro currents at the magnetopause, which in turn closes into the region 1 currents and the ionosphere. The resulting force due to these currents and the sheath magnetic field diverts plasma around the flanks of the magnetosphere and towards the tail (*Lopez et al.*, 2010).

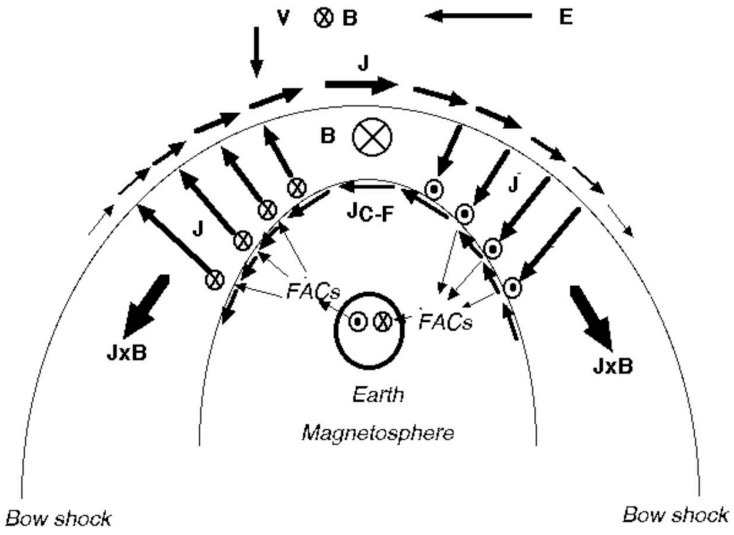

Figure 1.17: A diagram of the dayside magnetosphere and the current systems involved. J_{C-F} corresponds to the Chapman-Ferraro currents, and $\mathbf{J} \times \mathbf{B}$ is the force exerted on the magnetosheath plasma by the sheath magnetic field. From *Lopez et al.* (2010)

The dynamics shown in Figure 1.17 relates to polar cap potential saturation based on the strength of the sheath magnetic field. If the IMF is significantly strong, there is likely to be a large magnetic shear across the bow shock due to the compression ratio. It is therefore possible that the sheath could be dominated by magnetic pressure over thermal and dynamic pressure. In this case, less plasma will flow into the

reconnection site at the nose of the magnetosphere, and plasma will be accelerated along the flanks. This would in turn reduce the reconnection rate and the resulting reconnection electric potential, causing the polar cap potential to saturate (*Lopez et al.*, 2010). The key parameter in polar cap potential saturation would thus be the plasma-β in the sheath. At low beta, more flow would be diverted around the flanks, reducing the amount of plasma pushed into the reconnection region. It is worth noting, however, that previous research has demonstrated that low-β plasma tends to have a faster reconnection rate than high-β plasma, and the exact thresholds of these have yet to be determined (*Scurry et al.*, 1994). The Alfvènic Mach number may also play a role, since it tends to be lower at higher IMF magnitude. It does not need to be as low as in the Alfvèn wing model.

1.5.4 Ionospheric Influence on Saturation

The influence of the ionosphere on polar cap potential has also been suggested by various studies. *Winglee et al.* (2002), for example, demonstrated that during strong geomagnetic storms, there is an increase in O+ outflow from the ionosphere. This can cause mass loading in the magnetospheric plasma and limit the momentum of the convection.

Conductivity can also play a role in the polar cap potential. A variety of statistical models of the polar ionospheric potential pattern as well as the distribution of field aligned currents show different intensities in the summer and winter hemisphere (*Weimer*, 1995, 1996, 2001a,b; *Papitashvili et al.*, 1994, 1999, 2002; *Papitashvili and Rich*, 2002; *Christiansen et al.*, 2002; *Dremukhina et al.*, 1998). As an example, *Christiansen et al.* (2002) showed that region 1 FACs had an intensity that was 1.5 times larger in the summer hemisphere than in the winter hemisphere. At solstice, the

summer polar ionosphere is illuminated by the sun while the winter polar ionosphere is not. This results in a higher conductivity in the summer ionosphere. There is also a natural asymmetry in the polar magnetic field even in equinox conditions, with the geomagnetic poles being shifted by about 9^o away from the Earth's rotation axis in the northern hemisphere, and by 15^o in the southern hemisphere. It is worth noting that all MHD simulations of the saturation phenomenon have at present had uniform conducting ionospheres of equal conductivity in both hemispheres.

Also, with the exception of the (*Kivelson and Ridley*, 2008) hypothesis, most models of polar cap potential saturation involve limiting the reconnection rate at the magnetopause. It would be interesting to see how the ionospheric potential patterns under strong driving respond to different levels of ionospheric conductivity.

1.6 Motivation

The saturation problem has several questions that have been left unanswered. First, most discussions of polar cap potential saturation tend to focus on the large scale convection pattern formed under Southward IMF. While some papers such as *Ridley* (2007) and *Lopez et al.* (2010) mention the reverse convection cells under northward IMF in passing, minimal attention is given to whether the potential across these cells saturate. Also, in empirical studies of polar cap potential saturation, most previous research has demonstrated that saturation occurs without much work put into explaining why it occurs (*Shepherd et al.*, 2002; *Hairston et al.*, 2003, 2005). Many models of polar cap potential saturation express specific parameters in the solar wind which could impact the saturation of the polar cap potential.

The purpose of this study is to empirically investigate the polar cap potential phenomenon at a level of detail which could provide clues as to the mechanism by

which the polar cap potential saturates. First, it will be demonstrated that the reverse convection potential under northward IMF also saturates. Second, the response of the reverse convection potential in the saturation regime to various interplanetary parameters will be investigated. The average electric field across the reverse convection cells under saturation will then be compared to the average saturated polar cap electric field under southward IMF under winter, equinox and summer conductivity conditions. Fourth, the reverse convection electric field and how it relates to the open-closed field line boundary will be examined in both hemispheres simultaneously in order to investigate the impact of internal reconnection on the reverse convection potential. Finally, a statistical examination of the "saturation" regime of driving for southward IMF will be done in order to determine possible relationships between various interplanetary and geospace parameters and the extent of polar cap potential saturation.

CHAPTER II

INSTRUMENTS AND MEASUREMENT TECHNIQUES

In order to study the polar cap potential saturation phenomenon, instruments making measurements in the solar wind and the ionosphere will be used. Solar wind data is used to calculate the interplanetary electric field (IEF) and various interplanetary parameters which might impact the saturation of the polar cap potential. Ionospheric data will primarily be from instruments which measure plasma drift in the polar ionosphere. These data-sets allow one to calculate convection patterns in the ionosphere, as well as derive the ionospheric electric field and cross polar cap potential.

2.1 Solar Wind Data Analysis

2.1.1 The ACE Satellite

A majority of the solar wind and IMF data were taken from the Advanced Composition Explorer (ACE) satellite. This satellite orbits around the L1 point, which is one of the Lagrange points where the gravitational fields of the Earth and the sun cancel. The L1 point is upstream in the solar wind between the Earth's day side and the sun. For this reason, it is a prime location to measure solar wind parameters before they reach the Earth. There are two instruments on ACE. MAG measures the

components of the magnetic field vector and SWEPAM measures plasma parameters such as composition, density, velocity and temperature (*Stone et al.*, 1998).

A complication in using ACE satellite data is the delay between a measurement the satellite makes and the time it takes for that measurement to reach the Earth's magnetopause. As can be seen from Figure 2.1, depending on the position of the ACE satellite in its orbit around the L1 point, it will see a different point on the Parker spiral. Thus, the Earth's magnetopause might see the measurement earlier or later than the expected time of travel between the L1 point and the magnetopause (*Ridley*, 2000). There are several methods to calculate when a measured parameter will be seen at the magnetopause, but the data used in this study was pre-propagated using the minimum variance technique outlined by *Weimer et al.* (2003). Two data-sets of particular interest is the pre-propagated OMNI database, which contains pre-propagated solar wind data from multiple sources (*King and Papitashvili*, 2005), as well as pre-propagated ACE data which has been analyzed at UCLA. The error of propagation time estimates can be on the order of a few minutes, and thus will impact time selection criteria when the effects of changes in the solar wind are measured (*Ridley*, 2000).

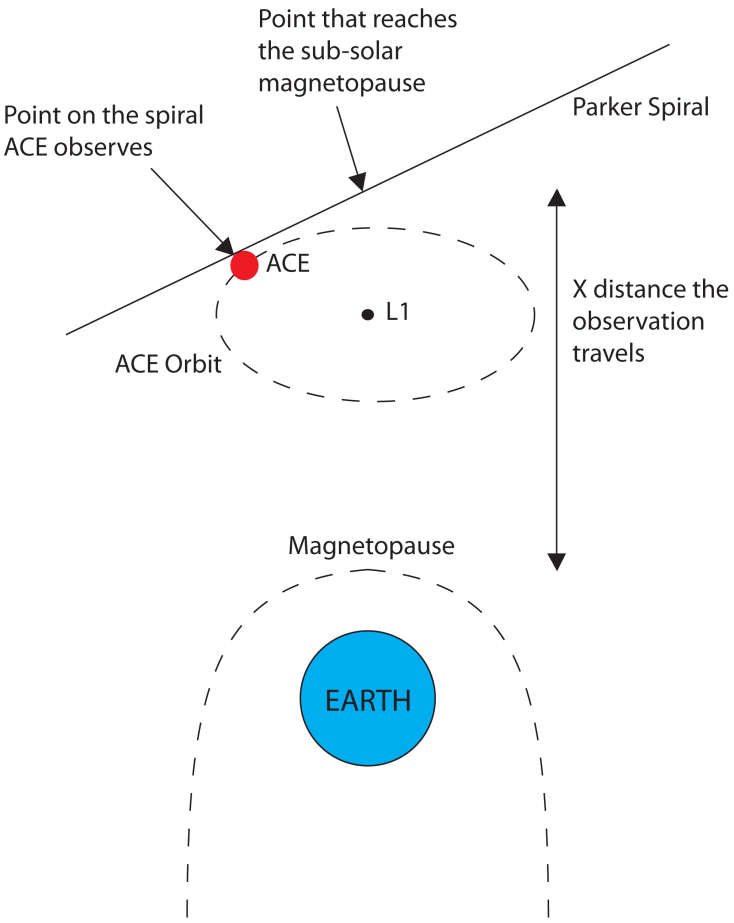

Figure 2.1: A picture of the ACE orbit with respect to the magnetopause and the parker spiral.

2.1.2 The Electric Field Coupling Functions

When studying the saturation of the polar cap potential and the reverse convection potential, we are working with a system that responds to the direction of the interplanetary electric and magnetic fields in addition to the magnitude. For example, the more southward the IMF is oriented, the larger the reconnection potential on the dayside magnetopause. In order to account for this, "coupling functions" are often used which give the measure of the effective interplanetary electric field coupled into the magnetosphere.

For southward IMF, *Sonnerup* (1974) proposed a geometric coupling function which could serve as a metric for the the effective interplanetary electric field (IEF) coupled into the magnetosphere during sub-solar magnetic reconnection, E_{KL}, given by Equation (2.1).

$$E_{KL} = V B_T \sin^2 \frac{\theta}{2} \tag{2.1}$$

Where V is the anti-sunward component of the solar wind velocity, $B_T = \sqrt{B_Z^2 + B_Y^2}$ is the IMF transverse to V, and $\theta = \cos^{-1} \frac{B_Z}{B_T}$ is the IMF clock angle in the (Y-Z) plane (*Kan and Lee*, 1979; *Sonnerup*, 1974). Several studies have used this parameter to correlate the interplanetary electric field with the polar cap potential (*Reiff et al.*, 1981; *Weimer*, 1995; *Shepherd et al.*, 2002).

When the IMF is purely northward, there will be a clock angle of zero degrees, and the sine term in equation (2.1) will be zero. Thus, in order to study the behavior of reverse convection cells, another metric must be used. Since the sine term is a non-physical geometric scaling factor, it can be altered to look for events where high latitude reverse convection cells would form. If one assumes that a pure y IMF would not generate reverse convection and that the y-component of the IMF only effects the skew of the reverse cells, the energy coupling function can be modified as shown in Equation (2.2).

$$E_{RC} = -V_x B_T cos^n \theta \tag{2.2}$$

This will always be positive as long as the value of n is an even integer and the clock angle is between -90^o and 90^o. The value of the exponent will directly effect how much the y component of the IMF impacts the value of E_{RC}. The larger n is, the more the y component will reduce the coupling function's magnitude. Plots of these functions for $n = 2$ and $n = 4$ can be seen in Figures 2.2 and 2.3.

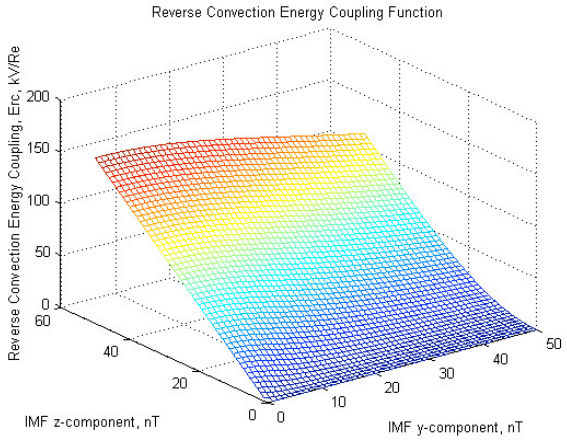

Figure 2.2: E_{RC} versus the IMF y and z component for solar wind with a bulk velocity of 500 km/s and $n = 2$

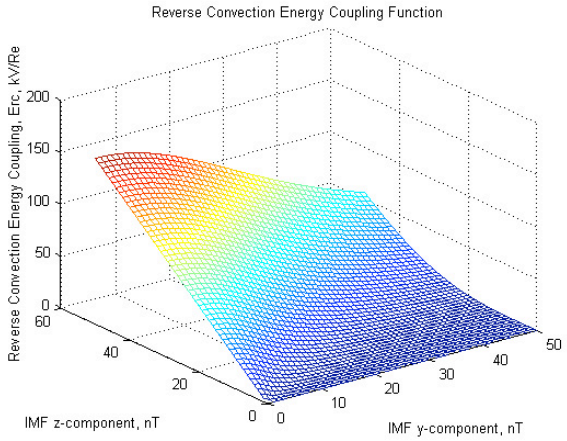

Figure 2.3: E_{RC} versus the IMF y and z component for solar wind with a bulk velocity of 500 km/s and $n = 4$

In this study, $n = 4$ will be used. As seen in Figure 2.3, an exponent of four limits the influence of the IMF-y component when selecting events for study. Also, $n > 4$ was not used because it would cause the function to increase rapidly with clock angle, and the main ionospheric data-set in the present study, SuperDARN, would be difficult to bin for events with larger values of E_{RC}. Figure 2.4 shows a

comparison between E_{RC} and E_{KL} versus IMF clock angle, θ. It is evident that E_{RC} maximizes at $\theta = 0$, at which value E_{KL} is at a minimum.

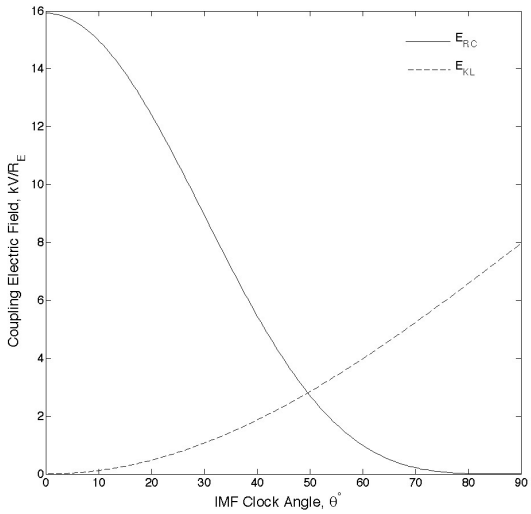

Figure 2.4: A comparison between E_{RC} and E_{KL}, represented by the solid line and dashed line respectively. For both cases, the IMF magnitude was set to 5 nT and the anti-sunward velocity was 500 km/s as the IMF clock angle was varied.

2.2 Ionospheric Electric Potential Mapping

2.2.1 The Super Dual Auroral Radar Network

The Super Dual Auroral Radar Network (SuperDARN) is a network of high latitude coherent scatter radars which work in conjunction to produce large scale convection patterns in the polar ionosphere. As of 2007 there were 11 radars in the northern hemisphere and 7 radars in the southern hemisphere, with a diagram of the locations and overlap given in Figure 2.5. Additional radars have been constructed since 2007, but their doppler measurements have not been used in the present study.

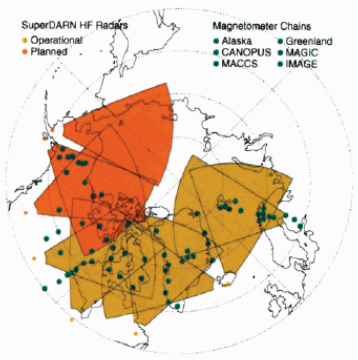

Figure 2.5: Coverage of the SuperDARN radars in the northern hemisphere. From *Ruohoniemi and Baker* (1998).

A SuperDARN radar operates at the high frequency (HF) band of the radio spectrum, and is typically capable of transmitting at center frequencies between 8 and 20 MHz (*Chisham et al.*, 2007). The major mechanism by which the radar calculates line of sight (LOS) plasma drift velocities is by backscatter from ionization density irregularities aligned with the geomagnetic field. At 10.8 MHz, the signal is sensitive to irregularities with a wavelength of 13.9 m and studies have shown that in the F region, the irregularities which produce backscatter convect with the $\mathbf{E}\times\mathbf{B}$ drift of the plasma (*Ruohoniemi et al.*, 1987). They have also been demonstrated to be a common occurrence in the high-latitude regions of the ionosphere (*Ruohoniemi et al.*, 1987). The signal incident on the irregularities must be approximately orthogonal to the geomagnetic field lines, and thus the scatter is actually assisted by the refraction of the signal in the ionosphere (*Ruohoniemi et al.*, 1987; *Ruohoniemi and Greenwald*, 1996; *Chisham et al.*, 2007).

In order to obtain the large scale convection pattern, several steps must be taken. First, the line of sight velocities calculated by the each radar are placed into spatial bins with a width of 1 degree of latitude and 10 degree increments of magnetic

azimuth, and the values are averaged within each bin (*Ruohoniemi and Baker*, 1998). An example of these bins and the resulting average line of sight velocities for a specific event are given by Figures 2.6 and 2.7.

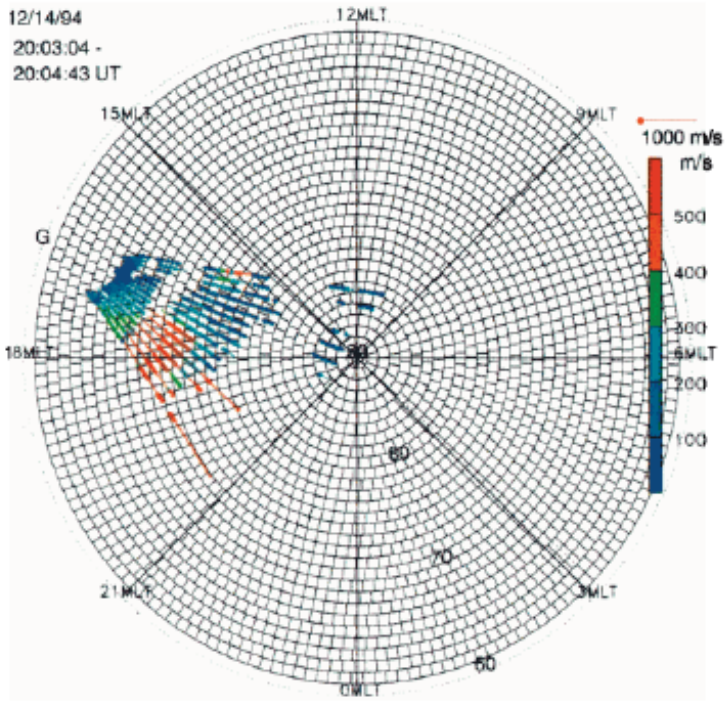

Figure 2.6: An example of the grid used for averaging the line of sight velocity vectors. The velocity data is taken from the Goose Bay radar on December 14, 1994, from 2003-2004:43 UT. From *Ruohoniemi and Baker* (1998).

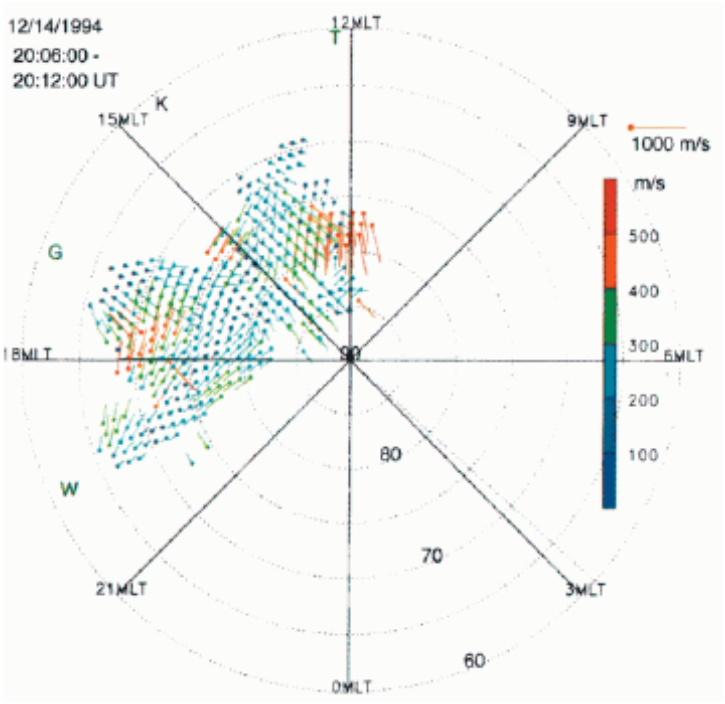

Figure 2.7: Averaged line of sight velocities from SuperDARN radars in Saskatoon, Kupaskasing, Goose Bay and Stokkseyri on December 14, 1994, 2006-2012 UT. Taken from *Ruohoniemi and Baker* (1998)

Once the spatially averaged line of sight velocities are calculated, line of sight velocities in areas where the fields of view of two or more radars can be resolved into convection velocity vectors. If more than two radars overlap, a least square error fit is used (*Ruohoniemi and Baker*, 1998). Figure 2.8 shows the result when the LOS velocity vectors given in Figure 2.7 are resolved. Areas with no overlap are not included in this figure (*Ruohoniemi and Baker*, 1998).

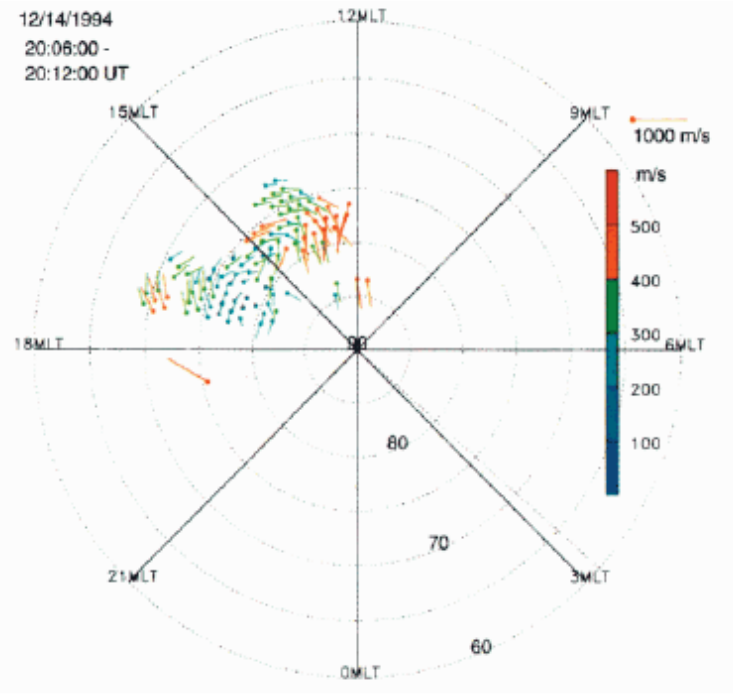

Figure 2.8: The velocity vectors resolved from the LOS vectors in Figure 2.7. From *Ruohoniemi and Baker* (1998)

2.2.2 Spherical Harmonic Mapping of the Ionospheric Electric Potential

Once ionospheric LOS velocity measurements have been spatially gridded, one can proceed to calculate the ionospheric potential pattern, Φ. This is done by assuming that the geomagnetic field is stationary and that the net charge density in the ionosphere is zero. In this case, the ionospheric electric potential can be found using Laplace's equation (2.3) (*Jackson*, 1975).

$$\nabla^2 \Phi = 0 \tag{2.3}$$

If the potential is assumed to exist on the surface of a spherical Earth, then the solution of Laplace's equation is a spherical harmonic expansion given by Equation (2.4) (*Weimer*, 1995; *Jackson*, 1975).

$$\Phi(\theta,\phi) = \sum_{l=0}^{\infty} \sum_{m=-l}^{+l} A_{lm} \sqrt{\frac{2l+1}{4\pi} \frac{(l-m)!}{(l+m)!}} P_l^m(\cos\theta) e^{im\phi} \tag{2.4}$$

Where θ is the co-latitude and ϕ is the azimuthal angle on the surface of an arbitrary sphere, and P_l^m is the Legendre polynomial. For the ionospheric potential, θ and Φ can be explained in terms of geomagnetic coordinates by Equations (2.5) and (2.6) (*Weimer*, 1995).

$$\theta = (90 - MLAT)\frac{pi}{45} \tag{2.5}$$

$$\phi = MLT\frac{pi}{12} \tag{2.6}$$

Where MLAT is the magnetic latitude and MLT is the magnetic local time. MLAT is the latitude based on the location of the magnetic north pole, not the geographic one. MLT is a magnetic meridian where it is at a certain local time. For example, MLT noon would be the magnetic longitude line which directly faces the sun and MLT midnight would be the magnetic longitude line facing opposite the sun.

Since it was shown by Equation (1.19) that the plasma convection velocity in the ionosphere flows on equipotential lines, an electric potential pattern can be fit to convection data (*Weimer*, 1995; *Ruohoniemi and Baker*, 1998).

To calculate the polar cap potential pattern, a routine which fits velocity vectors to a spherical harmonic expansion is used. Coefficients are calculated to minimize the χ^2 value for the LOS component of the velocity vectors (*Ruohoniemi and Baker*, 1998). Because χ^2 is defined for the LOS component, even measurements where there is no overlap between radar fields of view may be used in the spherical harmonic fit.

Also, to fill in spaces with no coverage, velocity vectors from statistical patterns based on IMF orientation are used (*Ruohoniemi and Greenwald*, 1996). The result of the fit applied to the velocity LOS vectors given in Figure 2.7 is shown in Figure 2.9.

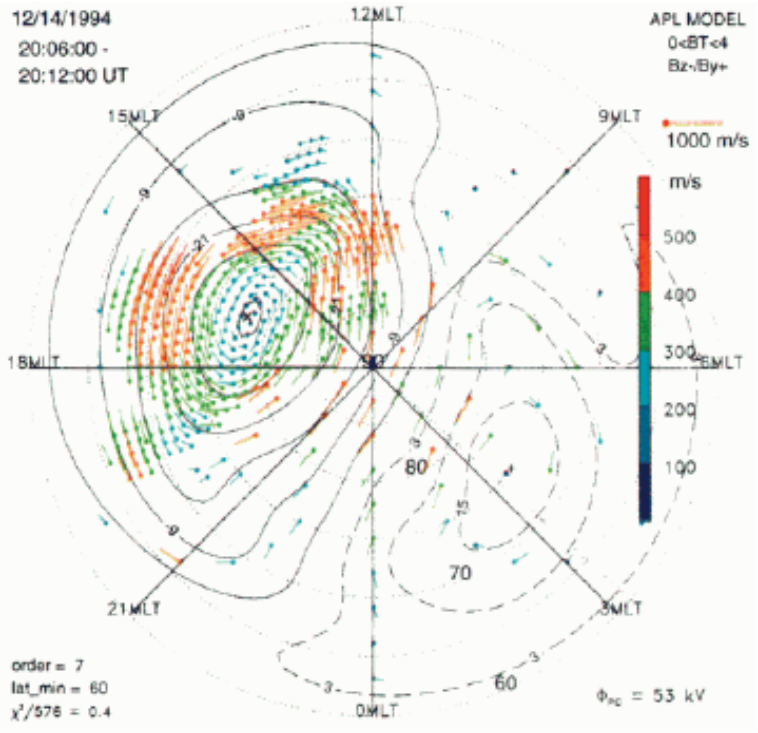

Figure 2.9: The convection and potential pattern fit to the LOS vectors in Figure 2.7. The order of the expansion is 7. From *Ruohoniemi and Baker* (1998)
.

2.3 The Defense Meteorological Satellite Program

The Defense Meteorological Satellite Program (DMSP) is a collection of satellites with circular, sun-synchronous, polar orbits that make measurements of various plasma parameters in the ionosphere (*Rich and Hairston*, 1994). The instrument contained within the DMSP satellites which is used in the present study is the SSIES thermal plasma monitor, which contains an ion drift meter (IDM) as well as the SSJ/4 energetic particle detector.

The SSJ/4 particle detector measures the energy flux of precipitating electrons

and ions within the 0.3 to 30 keV range (*Hardy et al.*, 1984). These particles precipitate along geomagnetic field lines to form the aurora, and determining the energy flux at a specific point, one can determine whether the measurement is on open or closed field lines (*Hardy et al.*, 1985, 1989). The SSJ/4 particle detector will be used extensively in Chapter 6 in order to observe the different modes of reconnection under northward IMF in the "saturation" regime of driving.

The IDM measures the angle of arrival of ions to collector plates which are on an aperture facing forward along the satellite track (*Rich and Hairston*, 1994). Drift along the satellite track, as well as drift perpendicular to the track can be inferred. For the present study, only the cross-track drift will be used, since these measurements are the most reliable (*Rich and Hairston*, 1994).

There are several advantages to using DMSP satellites when measuring ionospheric convection and the polar cap potential. The foremost is that during events of extreme magnetospheric driving by the solar wind, the polar cap convection boundary expands equatorward and a large portion of the pattern is no longer visible to the SuperDARN radars (*Hairston et al.*, 2005). This lack of coverage can cause a reduction in the strength of the polar cap potential pattern measured. The DMSP satellites will still observe the zero-potential boundary (called the Heppner-Maynard boundary) even when the polar cap potential pattern has expanded. In the present study, DMSP measurements will be used to augment SuperDARN potential patterns in areas where there is poor to non-existant coverage by the radars.

The main weakness of DMSP drift measurements is that a pass over the polar cap takes approximately 20 minutes to complete. Thus, to infer the polar cap potential from DMSP measurements, one must assume that the ionospheric convection pattern was steady over the entire pass. Often, when the potential is integrated over the

satellite track, it will not return to zero. This offset is usually distributed throughout the potential pattern when DMSP data is processed alone. In the present study, care was taken to ensure the stability of the potential pattern whenever DMSP measurements were included in SuperDARN patterns.

CHAPTER III

REVERSE CONVECTION POTENTIAL SATURATION UNDER NORTHWARD IMF

While it has been demonstrated that during strongly southward IMF, the polar cap potential exhibits a non-linear saturation effect, the same has not been done for the reverse convection potential under northward IMF (*Shepherd et al.*, 2002; *Hairston et al.*, 2005). One challenge which arises is that it is very difficult to measure the reverse convection potential for individual events, especially using radar measurements. The purpose of this chapter is to use a statistical method to determine if the reverse convection potential under northward IMF does, in fact, exhibit non-linear saturation behavior.

3.1 Event Selection Criteria and Convection Map Averaging

3.1.1 Solar Wind and IMF Stability Criteria

Using E_{RC} as defined in Chapter 2, events were found using ACE MAG and SWEPAM data from 1998 to 2005 propagated to the magnetopause using the technique developed by *Weimer et al.* (2003). Events of quasi-stable E_{RC} were then placed into bins containing a minimum and maximum E_{RC} value. The criteria for quasi-stability was that the event stayed within the bin's maximum and minimum E_{RC} value for a minimum of 40 minutes. The E_{RC} range for each bin was selected to

maximize the spatial coverage of Doppler measurements within each bin, but at the same time provide enough discretization in the curve in Figure 3.3 to see a saturation effect if it occurs. Table 3.1 shows the range and number of events in each E_{RC} bin, and Figure 3.1 shows the statistics on B_Z and B_Y for each bin. From Figure 3.1, it is clear that while the value of B_Z varies over the bins, the value of B_Y does not vary significantly, demonstrating that any saturation effect measured would be influenced most by the northward direction of the IMF.

Table 3.1: Bins of E_{RC} Used To Generate Figure 3.3

Range (kV/R_E)	Events	Range (kV/R_E)	Events	Range (kV/R_E)	Events
0-2	4,286	19-23	33	31-38	10
2-4	175	20-24	38	31-40	25
4-6	79	21-25	31	32-36	11
10-16	65	22-26	26	32-39	15
12-15	54	23-27	20	37-47	13
13-16	45	24-28	15	40-50	15
14-18	27	25-30	23	43-53	10
16-19	22	27-32	21	46-56	8
16-21	26	28-36	26		
18-22	33	30-36	11		

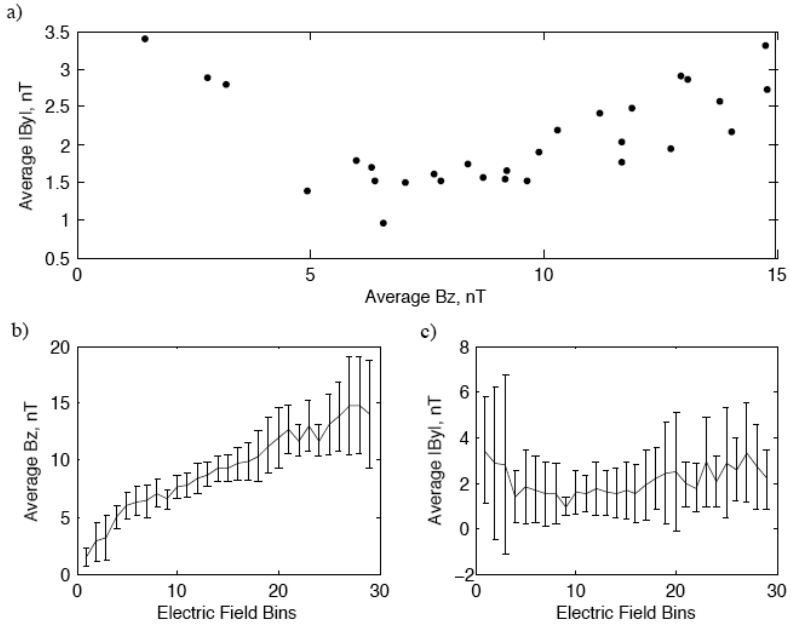

Figure 3.1: Statistics on the IMF for each bin: a) scatter plot of the average B_Z and corresponding average By magnitude for each bin, b) average B_Z and its standard deviation represented as error bars for each bin, c) average $|B_Y|$ magnitude and its standard deviation represented as error bars for each bin.

3.1.2 Convection Map Averaging

Global convection patterns from which Φ_{RC} was found were then calculated using the Super Dual Auroral Radar Network (SuperDARN) (*Chisham et al.*, 2007). It is difficult to measure the reverse convection potential for individual events using SuperDARN radar data. Oftentimes, coverage of the reverse convection cells can be spotty in an individual event, resulting in a fitted potential pattern based primarily on statistical model vectors. Because of this, averaging the potential patterns of all events in an E_{RC} bin will result in either weak or non-existent reverse convection patterns, which could even misleadingly force a saturation result. The method in this study relies on the principle of superposition, as well as pre-processing the line of sight velocity vectors (VLOS) in order to generate the most likely convection pattern

for an E_{RC} bin. This method requires no model vectors to fill in the pattern, and could be viewed as a spatial analogue to the superposed epoch technique. The steps taken to generate the reverse convection potential are as follows.

- The map of the polar cap is divided into 100 km by 100 km spatial bins. These spatial bins are then divided further into bins of VLOS directions in ten degree increments of magnetic azimuth from -90 to 90 degrees.

- VLOS vectors from the SuperDARN for all events within the E_{RC} bin were then placed in their respective spatial bin. This allows patterns with coverage in different parts of the reverse convection potential cells to be superposed.

- For each spatial bin, it is determined whether the majority of measurements are positive or negative. The median positive or negative value is then chosen based on which dominates. This reduces data going into the spherical harmonic fitter, and smooths out large positive and negative values which cancel in the fitter at convection reversal boundaries (*Ruohoniemi and Baker*, 1998).

- A spherical harmonic fitting technique is then applied to the resulting gridded velocity measurements. Here, the electric field in the ionosphere is assumed to be the gradient of the electric potential, with equipotential lines that are the streamlines of the plasma convection. A potential pattern is then determined using a least squares fit of coefficients of a spherical harmonic expansion to the convection data (*Ruohoniemi and Baker*, 1998).

- Once an E_{RC} bin's potential pattern is determined, the reverse convection potential is measured by taking the difference between the minimum and maximum potential of the high latitude reverse cells. This is done manually to

ensure that the potential across the reverse cells is measured instead of the potential between a reverse cell and a lobe cell.

Figure 3.2, for example, shows four convection patterns as the IMF turns increasingly northward. These patterns are generated using the statistical fitting method described above. Each pattern is presented in AACGM MLAT-MLT format with the magnetic pole at the center and magnetic noon directed up the page. The lowest latitude shown is 60 degrees and the contour spacing is 1kV. Color-coding shows the number of gridded SuperDARN measurements that contributed to the calculation of each pattern. The four convection patterns in Figure 3.2 correspond to the following bins of E_{RC}: (a) 2-4, (b) 10-13, (c) 19-23, and (d) 32-39 kV/Re. The values of the reverse convection potential, Φ_{RC}, are 2.85, 10.66, 17.44, and 19.36 kV respectively. As E_{RC} increases, the reverse convection potential cells become more prominent and then saturate at the largest values of E_{RC}.

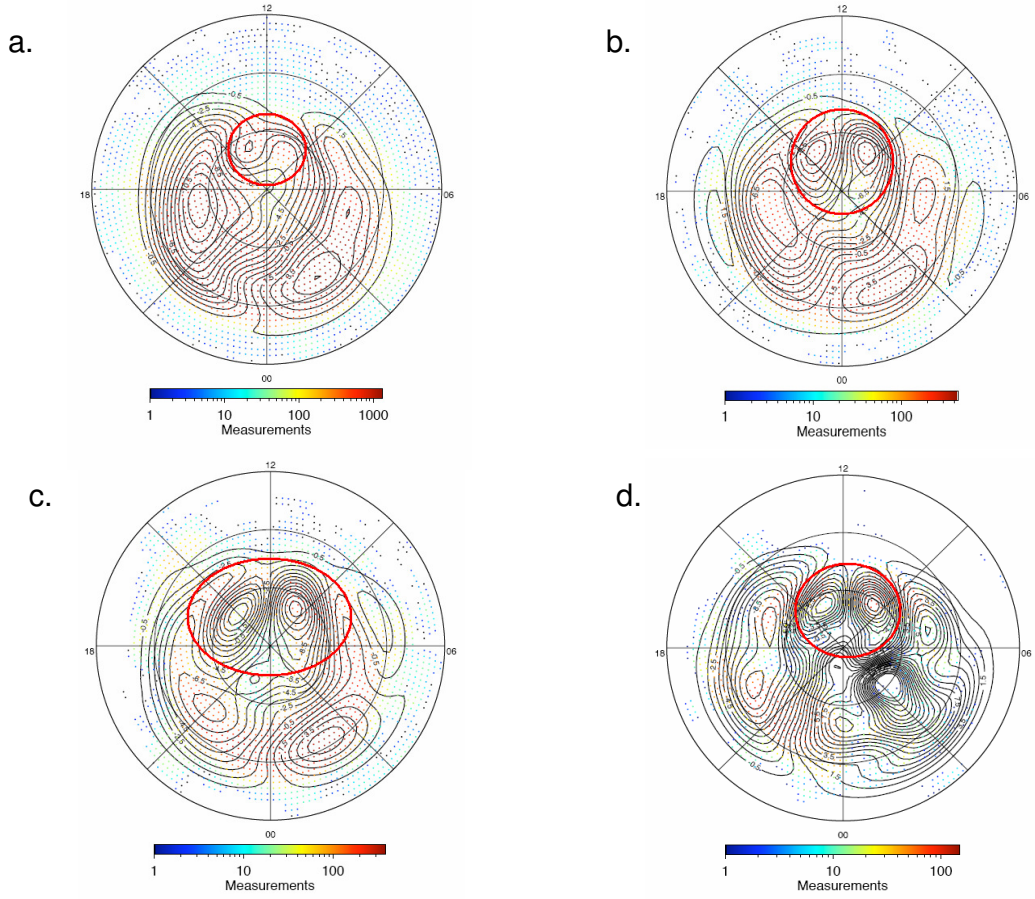

Figure 3.2: Calculated four cell convection pattern for four E_{RC} bins: a) 2 to 4 kV/Re, b) 10 to 13 kV/Re, c) 19 to 23 kV/Re and d) 32 to 39 kV/Re. The dayside convection cells are circled in red. Corresponding reverse convection potentials are a) 2.85 kV, b) 10.66 kV, c) 17.44 kV and d) 19.36 kV.

3.2 Saturation of the Reverse Convection Potential

Figure 3.3 shows a plot of the reverse convection potential for E_{RC} values up to 60 kV/RE. The horizontal bars show the range of values in each E_{RC} bin used to calculate each convection pattern. For low values of E_{RC} (i.e. 0-18 kV/RE) the reverse convection potential exhibits linear characteristics but as E_{RC} increases the reverse potential starts to saturate, similar to what has been identified previously for

southward IMF (*Shepherd et al.*, 2002).

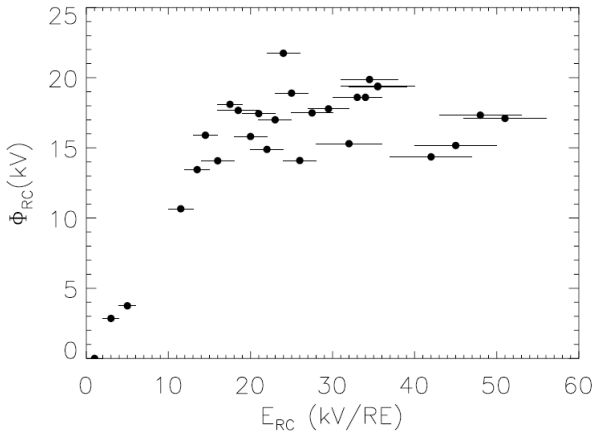

Figure 3.3: The reverse convection potential, Φ_{RC}, as a function of E_{RC}. The marks represent the center of the bins, and the horizontal lines represent the width of each bin in kV/Re

It is still unclear at this time why the NBZ currents and the potential across the vortices they generate should saturate. In the case of southward IMF, there are several models that account for saturation of Φ_{PC}. The Siscoe-Hill model of polar cap potential saturation involves the strengthening of region 1 field aligned currents to the point where their $\mathbf{J} \times \mathbf{B}$ force replaces the Chapman-Ferraro currents as the main counter to solar wind ram pressure and the erosion of the magnetopause magnetic field which limits reconnection (*Siscoe et al.*, 2004). Since the NBZ currents are driven by reconnection at the cusp, it is unclear how this hypothesis could also be applied to saturation of the reverse convection cells. The sheath-control mechanism and the Alfven wing hypothesis both propose that the reverse convection potential should saturate. One thing that hasn't been investigated is whether or not there is a limit to the amount of current the ionosphere can carry. If it is the case that the ionospheric conductivity plays a role, then it could help explain the saturation

phenomenon for both the southward and northward IMF cases.

For further study, analysis of the reverse convection potential saturation in response to various driving conditions will be done. Bins of more extreme driving will also be added to better resolve the saturation trend and the saturation potential. Also, comparing electric fields with the southward IMF case and looking for seasonal asymmetries would help to determine how much current can pass through the ionosphere at a given time.

CHAPTER IV

REVERSE CONVECTION POTENTIAL SATURATION UNDER NORTHWARD IMF AND VARIOUS DRIVING CONDITIONS

In the previous chapter, it was demonstrated that the reverse convection potential under northward IMF does, in fact, exhibit non-linear saturation behavior. This is a result that had not yet been demonstrated. While the phenomenon of reverse convection potential saturation has been investigated, the cause has not. For southward IMF, studies have suggested the effect of various driving parameters such as dynamic pressure and Alfvènic Mach number on the saturation of the polar cap potential (*Siscoe et al.*, 2002a; *Ridley*, 2007). There have not yet been any studies to our knowledge on the response of the four cell pattern formed under northward IMF to various driving conditions. Also, there is a difference in ionospheric conductivity between the winter and summer hemispheres due to the lack of photoionization in the winter. Separating out events of strong northward IMF by season should shed light on the response of the four cell pattern to variations in ionospheric conductivity (*Fujii et al.*, 1981).

The purpose of this study is to build upon the previous chapter's results and investigate the effects of various solar wind driving conditions as well as ionospheric

conductivity on the saturation potential and electric field of the NBZ cells. The relationship between the saturation of Φ_{PC} and Φ_{RC} will also be discussed. We expand on the results presented in Chapter 3, showing the saturation of the reverse convection electric field under northward IMF, as well as the dependence of Φ_{RC} on Alfvènic Mach number and solar wind β. It will be demonstrated that there is a clear seasonal dependance of the reverse convection potential pattern, and that the reverse convection potential still saturates even when the Alfvènic Mach number is nominal. Also, there is a clear dependance of the reverse convection potential under strong northward IMF driving on solar wind plasma β.

4.1 Methodology

In Chapter 2, a reverse convection coupling function, E_{RC}, was defined. This coupling function will continue to be used in the present study. In order to increase the resolution of the previous chapter's results, events were found using propagated 1-minute data from the OMNI database between 1998 and 2007 (*King and Papitashvili*, 2005). This new data-set adds 2 more years of solar wind data to the study. Using data from 2006 and 2007 was also beneficial for the overall study because it allowed for the use of the higher latitude PolarDARN radars (*Chisham et al.*, 2007). Stability criteria for bins of E_{RC} are the same as the previous chapter. In the present study, the effect of interplanetary parameters other than coupling functions on the reverse convection potential will also be examined. For these parameters, similar criteria will be used.

In order to calculate the polar cap potential, the same method of averaging potential patterns was used as in Chapter 3. For a given bin of solar wind and geophysical conditions, gridded SuperDARN data from each event was superposed and median

filtered, and a spherical harmonic fit was applied to obtain the potential pattern and the reverse convection potential.

4.2 Reverse Convection Potential and Electric Field Saturation

Figure 4.1 demonstrates the non-linear behavior of the reverse convection potential as E_{RC} increases, using the same bins as Chapter 3 in addition to several more bins in order to make the trend in the reverse convection potential more apparent. These bins include 40 to 60 kV/Re and 50 to 70 kV/Re. A bin ranging from 50 to 150 kV/Re was also examined with a potential found to be 20.49 kV. For the bins of E_{RC}, saturation occurs when the reverse convection reaches approximately 20 kV and when E_{RC} reaches above 18 kV/Re. It should be noted that this is by no means a maximum potential, as these are statistical patterns.

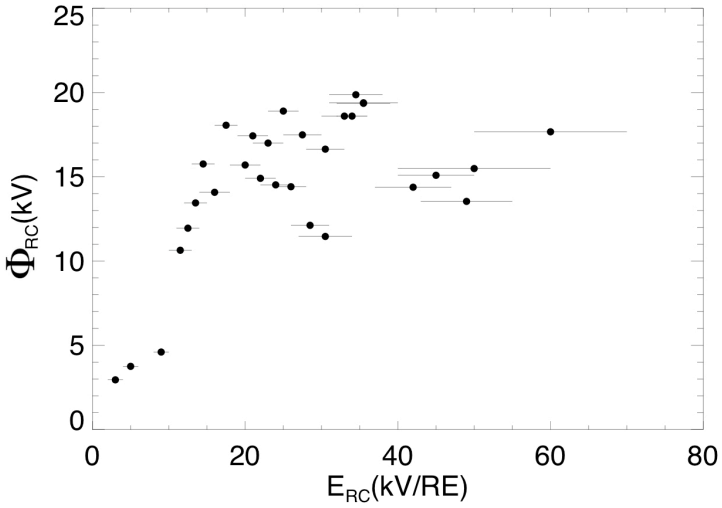

Figure 4.1: The reverse convection potential, Φ_{RC}, as a function of E_{RC}. The marks represent the center of the bins, and the horizontal lines represent the width of each bin in kV/Re.

In order to validate the result, one can measure the potential across the lobe

cells, also known as the viscous potential, in the four cell pattern and ensure that the method yields the expected result. Figure 4.2 shows the behavior of the viscous potential, Φ_{PC}, as E_{RC} increases. The viscous potential remains around 20 kV, with larger values that are not unreasonable for viscous interactions (*Papitashvili et al.*, 1981). The bins where the viscous potential exceeded 25 kV contained a larger amount of events in the winter months when the ionospheric conductivity is lower, which can lead to larger polar cap potentials. Values of exceedingly low viscous potential are found in bins where the viscous convection cells had significantly less coverage than the NBZ cells.

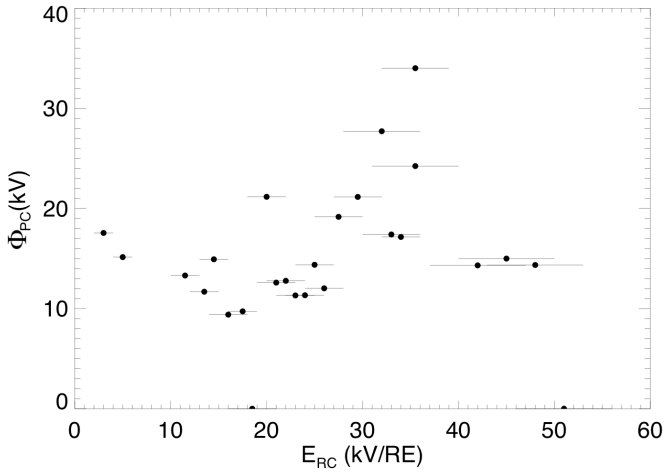

Figure 4.2: The potential across the viscous cells, Φ_{PC} as a function of E_{RC}. The marks represent the center of the bins, and the horizontal lines represent the width of each bin in kV/Re.

Figure 4.1 shows that the saturation potential in this study for Φ_{RC} is around 20 kV. This is very small in comparison to the southward IMF saturation potential of Φ_{PC}, which has been shown to be approximately 100 kV using SuperDARN measurements (*Shepherd et al.*, 2002). It should be noted, however, that during events of

extreme driving under southward IMF, the size of the polar cap becomes significantly larger than the distance between the centers of the NBZ cells under northward IMF. This difference in polar cap size makes comparison between saturated Φ_{RC} and Φ_{PC} as well as the determination of the saturation Φ_{PC} more difficult. It should be noted, however, that the electric field across two potential cells is inversely proportional to the distance across them, as noted by an electrostatic approximation of Faraday's Law (*Jackson*, 1975). Therefore, while the maximum potential across the reverse convection cells is significantly smaller than the saturation potential for southward IMF, the difference between the distance across the reverse convection cells and the polar cap size under extreme southward IMF can lead to comparable electric fields.

In order to calculate the electric field from Φ_{RC}, the great circle distance formula, given by equation (4.1), was used based on magnetic latitude and magnetic longitude of the center of each NBZ cell.

$$d = Re \cos^{-1} \left[\sin\theta_1 \sin\theta_2 + \cos\theta_1 \cos\theta_2 \cos\Delta\phi\right] \tag{4.1}$$

Where d is the great circle distance, Re is the earth's radius, θ_1 and θ_2 are the longitudes of the center of each cell, and $\Delta\phi$ is the difference in latitude between the centers of the NBZ cells (*Pearson*, 1990). In order to obtain the electric field across the cells, the potential is divided by the great circle distance, which on average tends to be approximately 1000 km. This distance is approximately a quarter of the polar cap diameter measured by imaging satellites during storm time southward IMF intervals (*Rastatter et al.*, 2005).

Figure 4.3 shows the behavior of the electric field across the reverse convection cells. E_{RC} is expressed in mV/m in order to directly compare with the electric field of the NBZ cells ($1mV/m \approx 6.4kV/Re$). The electric field of the reverse cells be-

gins to saturate at approximately 20 mV/m. It is likely that individual events can have larger and smaller electric fields, as these are statistical patterns. It should be noted that since the distance across the reverse convection cells is approximately one-fourth the polar cap size under southward IMF, and that the Φ_{RC} saturates at approximately one-fourth the saturated Φ_{PC} measured by *Shepherd et al.* (2002), then the electric field across both the saturated reverse cells and the saturated southward IMF potential pattern should be comparable. This hypothesis shall be tested and expanded upon in the next chapter.

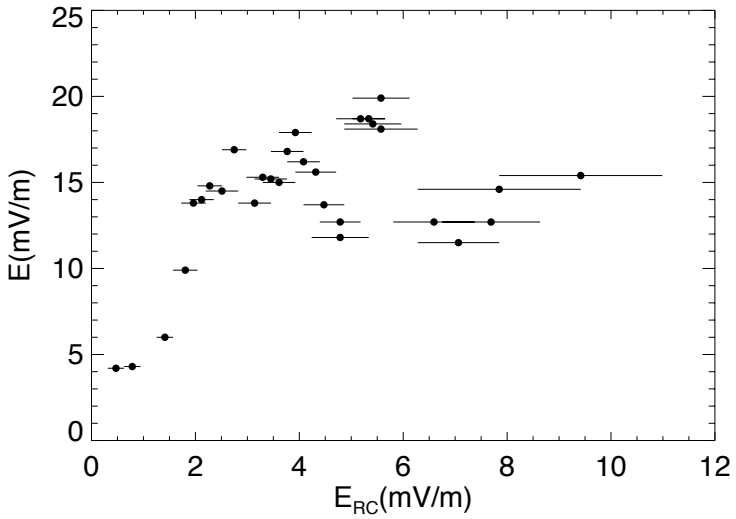

Figure 4.3: The electric field across the reverse convection cells as a function of E_{RC} The marks represent the center of the bins, and the horizontal lines represent the width of each bin in mV/m

It is worth noting at this point that there is a discrepancy between the saturation potentials measured by SuperDARN and DMSP under Southward IMF (*Shepherd et al.*, 2002; *Hairston et al.*, 2005). In the past, this has been explained by the fact that the polar cap expands equatorward during increasingly strong driving, which could mean that the potential pattern is outside the SuperDARN radars' fields of view

(*Hairston et al.*, 2005). Recent studies, however, have pointed to additional factors which can cause DMSP and SuperDARN to measure different polar cap potentials under extreme driving. *Drayton et al.* (2005) compared raw LOS measurements from SuperDARN with DMSP cross track plasma drift and fount they were related linearly with SuperDARN being smaller by a factor between 0.8 and 0.9. This mostly can be accounted for by difference in altitude between the measurements. Another study demonstrated that when SuperDARN velocity measurements were bin averaged and then converted to vectors, the scaling factor got as low as 0.3 to 0.5 (*Xu et al.*, 2007). The most plausible explanation is that when velocity measurements are averaged over large volumes, the more extreme spikes in velocity that exist adjacent to convection reversal boundaries tend to get smoothed over. This should not, however, impact the overall trend of potential measurements. *Sundberg et al.* (2009) showed saturation of Φ_{RC} using DMSP and also showed a saturation reverse convection potential which was approximately one fourth the saturation Φ_{PC} under southward IMF observed by *Hairston et al.* (2005). This is in agreement with what is seen using average convection patterns. The relationship between saturation measurements made by DMSP and SuperDARN will be discussed in more detail in chapters 5 and 7.

4.3 Seasonal Dependence

To help determine the effect of ionospheric conductivity on the four cell convection pattern which is formed under northward IMF, a comparison of statistical patterns from both the summer and winter ionosphere can be used. It is expected that during winter months, the ionospheric conductivity is lower due to reduced ionization from solar photons, thus increasing the electric potential according to Ohm's law. One can determine how the saturation of the reverse convection potential varies based on

conductivity by examining the average Φ_{RC} under strong driving.

In order to generate these patterns, two bins of E_{RC} from 18 to 60 kV/Re were used: one where all events were within 30 days of the winter solstice, and one where all events were within 30 days of the summer solstice. Statistical patterns were then generated using the convection map averaging technique described in Chapter 3. Figure 4.4 shows the E_{RC} behavior for the events used to generate a statistical pattern for the summer ionosphere, and Figure 4.5 demonstrates the E_{RC} behavior for the winter ionosphere. Comparison between the two figures shows that there is little significant difference in the distribution of solar wind electric field driving for either pattern. If anything, there may be slightly stronger coupling for the winter pattern than the summer pattern.

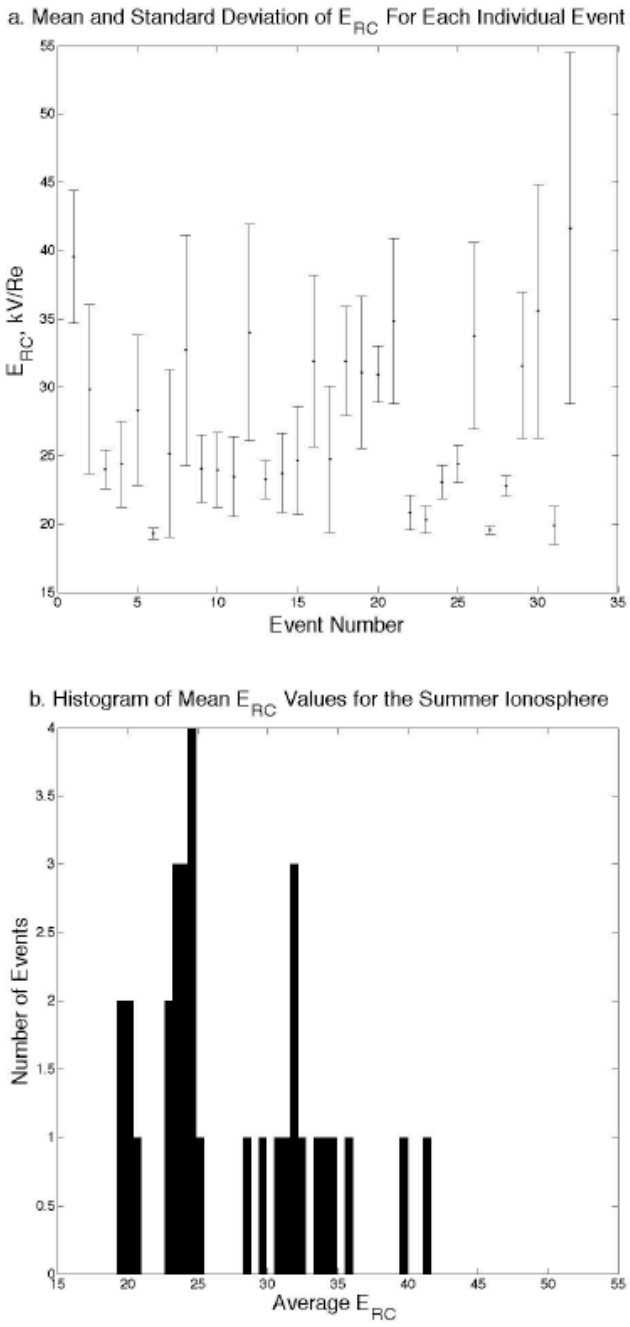

Figure 4.4: Statistics for the events within 30 days of the summer solstice. a) Each point on the x axis is an individual event within the summer bin, with the marks indicating the mean value of E_{RC} and the error bars along the y axis the standard deviation of E_{RC} b) A histogram demonstrating the distribution of mean E_{RC} values over the entire summer bin.

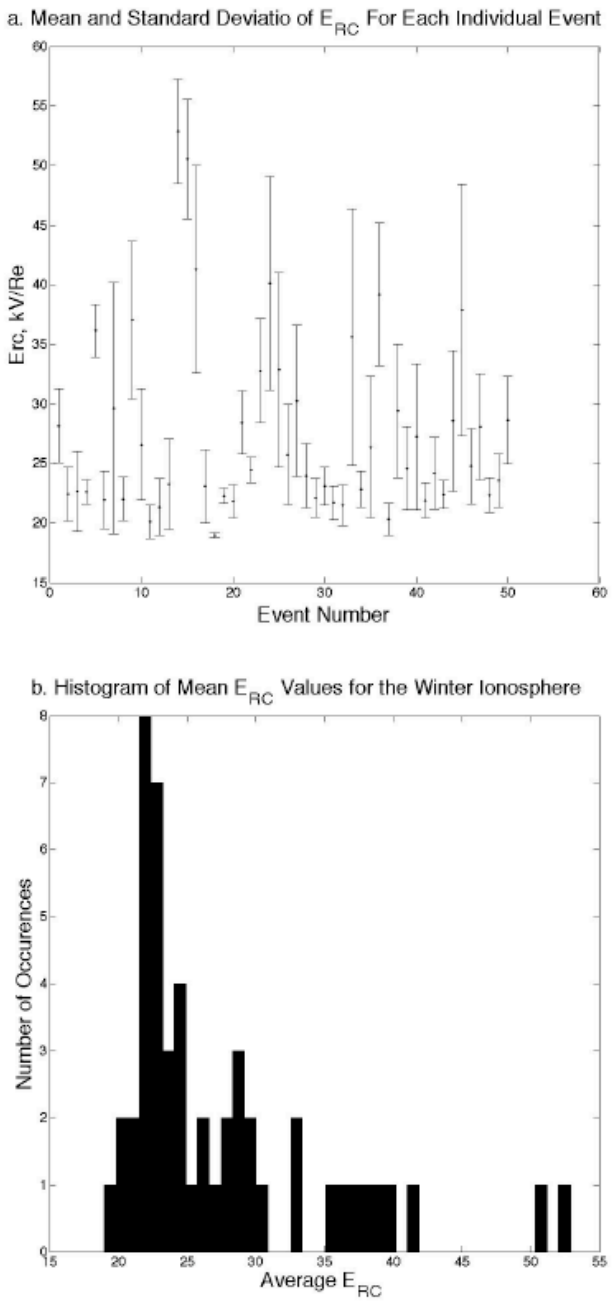

Figure 4.5: Statistics for the events within 30 days of the winter solstice. a) Each point on the x axis is an individual event within the winter bin, with the marks indicating the mean value of E_{RC} and the error bars along the y axis the standard deviation of E_{RC} b) A histogram demonstrating the distribution of mean E_{RC} values over the entire winter bin.

Figure 4.6 shows four cell convection patterns for both the winter and summer

seasons. It can be seen that the resulting reverse convection potentials show the opposite of what would be expected. Φ_{RC} is 11.45 kV in the winter and 16.5 kV in the summer, with electric fields of 11.5 mV/m and 19 mV/m respectively. With a winter ionosphere at a lower conductivity than summer, one would expect Φ_{RC} to be larger from Ohm's law. The opposite occurs for the NBZ cells. It should be noted, however, that the viscous cells do exhibit the expected behavior, with far more prominent potential cells and stronger anti-sunward flow in the winter ionosphere. It seems while the anti-sunward convection due to viscous interactions becomes increasingly strong during winter due to low conductivity, the sunward convection in the NBZ cells seems to be weaker, leading to less prominent reverse convection potential cells. This implies that the NBZ currents under saturation may not be a constant current generator, though the reason this occurs is yet to be determined.

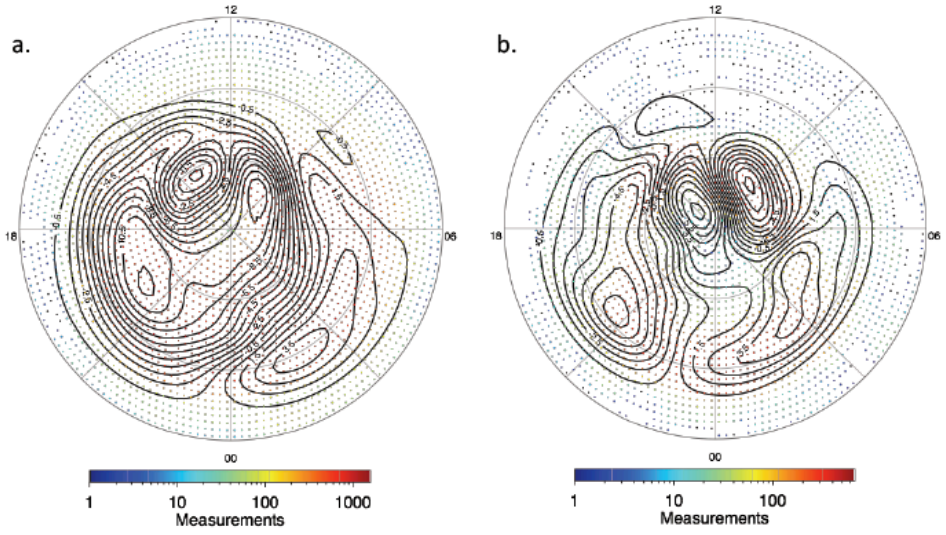

Figure 4.6: Calculated four cell convection patterns for both the (a) winter and (b) summer ionospheres within the saturation regime (E_{RC} greater than 18 kV/Re). The corresponding reverse convection potentials are a) 11.45 kV and b) 16.75 kV, with electric fields of a) 11.5 mV/m and b) 19 mV/m.

4.4 Alfvènic Mach Number Dependence

Since *Ridley* (2007) suggests Alfvèn wings can lead to saturation of polar cap potentials under both northward and southward IMF, it is useful to test the effect of Alfvènic Mach number on the reverse convection potential under northward IMF. In order to do this, first it will be useful to see the distribution of M_A for events within the linear and saturation regimes of Figure 4.1. If Alfvèn wings are a fundamental cause of saturation under northward IMF, then one would expect to see significantly lower M_A in the solar wind for the saturation regime of Figure 4.1. Events were organized based on whether they were stable within 8-17 kV/Re for the linear regime or within 25 to 60 kV/Re for the saturated regime of Figure 4.1. The mean M_A was then calculated for each event.

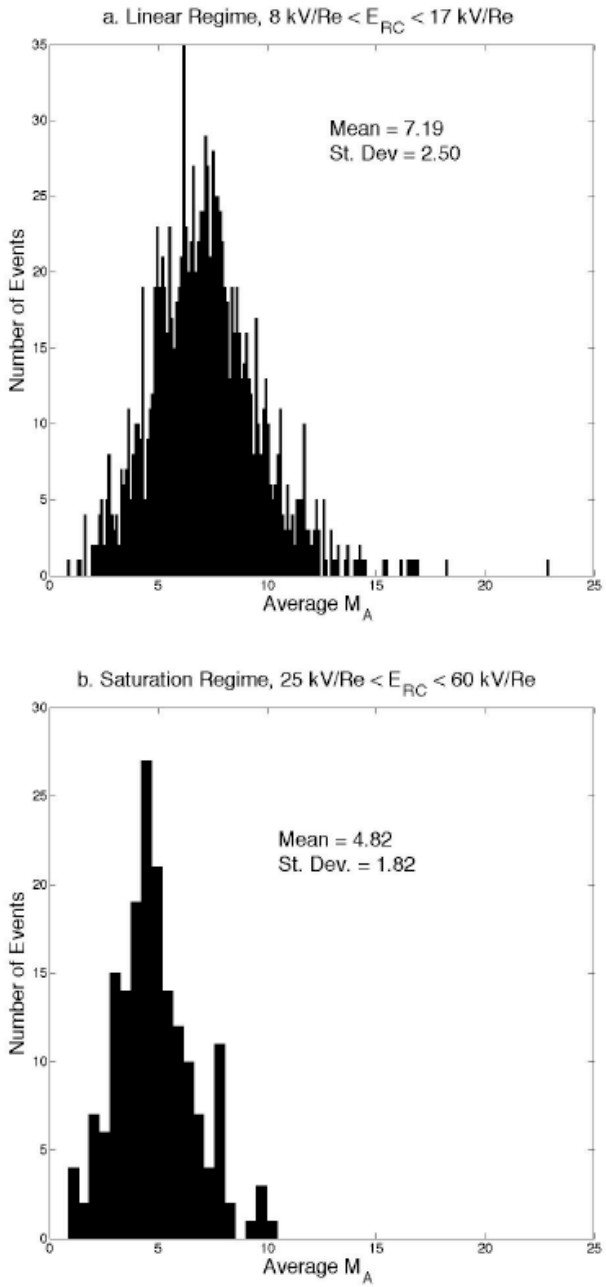

Figure 4.7: Histograms showing the M_A distribution for the the E_{RC} ranges of a) $8kV/Re < E_{RC} < 17kV/Re$ and b) $25kV/Re < E_{RC} < 60kV/Re$. The mean values of M_A in each are a) 7.19 and b) 4.82 with a standard deviation of a) 2.50 and b) 1.82.

Figure 4.7 shows the histograms for (a) the linear regime and (b) the saturation regime. The linear regime does tend to have events with a larger M_A value than

the saturation regime. This is to be expected, since as the IMF magnitude grows larger, the IMF's M_A grows smaller. This does not mean, however, that the value of M_A plays a role in the mechanism by which Φ_{RC} saturates. There is still a large amount of overlap between the linear and saturation regimes in Figure 4.7, with both containing events with very small values of M_A as well as events with nominal values of M_A.

Table 4.1: Bins of E_{RC} used to examine the reverse convection potential trend when $M_A > 5$

E_{RC}(kV/Re)	Mean M_A	St. Dev. M_A	E_{RC}(kV/Re)	Mean M_A	St. Dev. M_A
2-4	11.50	4.90	17-26	7.16	1.70
4-6	10.29	3.59	18-25	6.98	1.38
6-8	9.43	2.89	19-26	7.11	1.83
8-10	8.66	2.64	20-30	6.95	1.60
10-14	7.92	1.91	20-40	7.00	1.70
11-15	7.75	1.67	23-33	6.67	1.33
12-16	7.45	1.61	25-35	6.69	1.32
13-17	7.52	1.81	25-40	6.80	1.27
14-18	7.40	1.66	30-45	6.54	1.25
15-20	7.11	1.60	30-50	6.61	1.20
16-21	7.08	1.67	30-60	6.82	1.28
17-22	6.72	1.42	35-50	6.68	0.92
40-70	6.99	1.23			

In order to determine if the events with nominal M_A are also contributing to the overall saturation trend of Φ_{RC}, the method for generating Figure 4.1 was repeated, but with an additional restriction on M_A in the event selection criteria. Not only were all events required to stay within the minimum and maximum E_{RC} value of a

particular driving bin, but only events where M_A was at least 5 were used. The M_A minimum of 5 was chosen for several reasons. First, it provided the best amount of doppler measurements to ensure that any trend in Φ_{RC} with increasing E_{RC} would be apparent. It also excludes very small values of M_A, where simulations have shown Alfvèn Wings could become more apparent (*Ridley*, 2007). Table 1 shows the E_{RC} bins used, along with the mean and standard deviation of M_A in each bin.

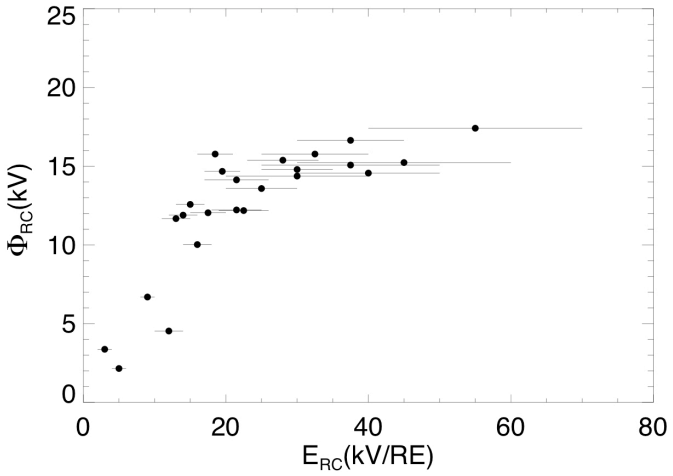

Figure 4.8: The reverse convection potential, Φ_{RC}, as a function of E_{RC}, for $M_A > 5$. The marks represent the center of the bins, and the horizontal lines represent the width of each bin in kV/Re.

Figure 4.8 shows the behavior of the reverse convection potential as E_{RC} increases. Φ_{RC} still demonstrates saturation behavior, with a peak potential of approximately 17 kV. Since the reverse convection potential still saturates at nominal M_A, it is unlikely that Alfvèn Wings are a fundamental cause of reverse convection potential saturation under northward IMF.

As a final way to examine the dependance of Φ_{RC} on M_A, events with E_{RC} ranging between 18 and 60 kV/Re were binned based on solar wind M_A. The stability

criteria was that the E_{RC} stay between 18 and 60 kV/Re and that M_A stay between its specified maximum and minimum value. Overlapping bins were used to ensure the best possible view of the behavior of Φ_{RC}. Figure 4.9 shows how the reverse convection potential varies with respect to M_A, as well as the mean E_{RC} for each M_A bin. The potential patterns used in this curve can be found in Appendix A. While at first it may seem that Φ_{RC} is decreasing with increasing M_A, the mean E_{RC} in each M_A bin is also decreasing. While this study was done in the E_{RC} driving regime where saturation occurs, variations in E_{RC} still could have a small impact on Φ_{RC}. It therefore appears that M_A has little impact on the value of Φ_{RC}.

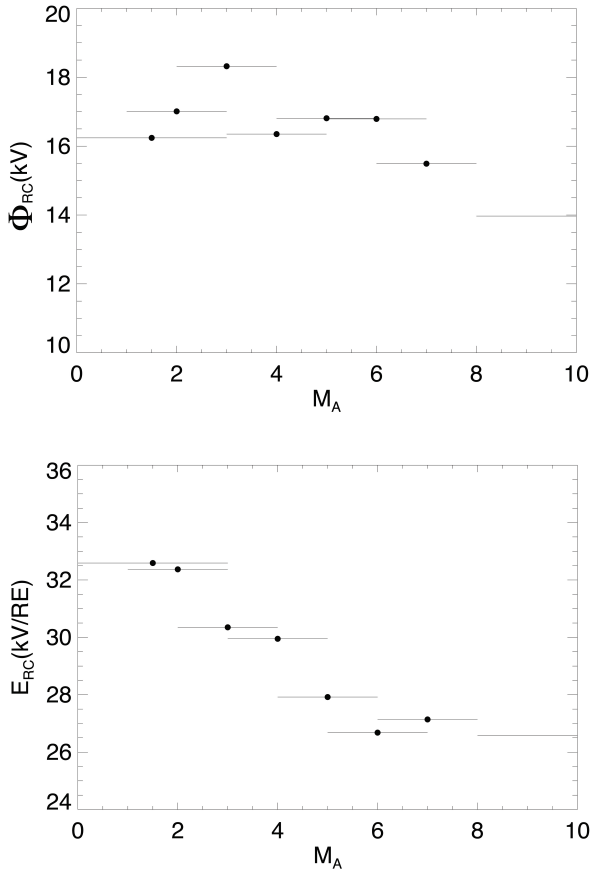

Figure 4.9: Statistics on the reverse convection potential for E_{RC} driving in the saturation regime and varying M_A. Top is the reverse convection potential and bottom is the mean E_{RC} for each M_A bin.

4.5 Solar Wind Plasma Beta Dependence

Another solar wind driving parameter which is useful for understanding magnetospheric behavior is the plasma β. This is the ratio between thermal pressure and magnetic pressure in the solar wind and is given by equation (4.2).

$$\beta = \frac{nkT_i}{B^2/2\mu_0} \tag{4.2}$$

Where β is the solar wind plasma beta, n is the number density, k is Boltzmann's constant, T_i is the ion temperature, and B is the magnitude of the IMF. *Scurry et al.* (1994) demonstrated that a low-β solar wind tended to lead to a higher reconnection rate on the dayside magnetopause for southward IMF. This also indicates that the upstream β in the solar wind influences the β in the magnetosheath. Therefore, understanding the effect of β on the reverse convection potential may shed light onto the effect of both reconnection and the shape of the magnetosphere. At low β, there is a high magnetic pressure, which leads to stiff frozen-in magnetic field lines and, theoretically, a faster reconnection rate. At high β, there is high thermal pressure, which accelerates plasma more in the ∇P direction. If β in the solar wind impacts β in the sheath, then by the sheath-control model of polar cap potential saturation, Φ_{RC} should be larger for higher β. It is also unclear whether the low-β regime is dominated by the higher reconnection rate predicted by *Scurry et al.* (1994) or by the plasma diversion predicted by *Lopez et al.* (2010), the former of which would lead to larger potentials in the ionosphere.

The first thing examined was the distribution of solar wind plasma β for both the linear and saturation driving regimes in Figure 4.1. Once again, events were organized based on whether they were stable within 8-17 kV/Re for the linear regime or within 25 to 60 kV/Re for the saturation regime of Figure 4.1. The mean value

of β was then calculated for each event. Figure 4.10 shows the distribution of solar wind plasma β for the linear and saturation regimes. The distributions seem to be comparable, with slightly lower β in the saturation regime. This is to be expected, since plasma β is inversely proportional to the IMF magnitude squared.

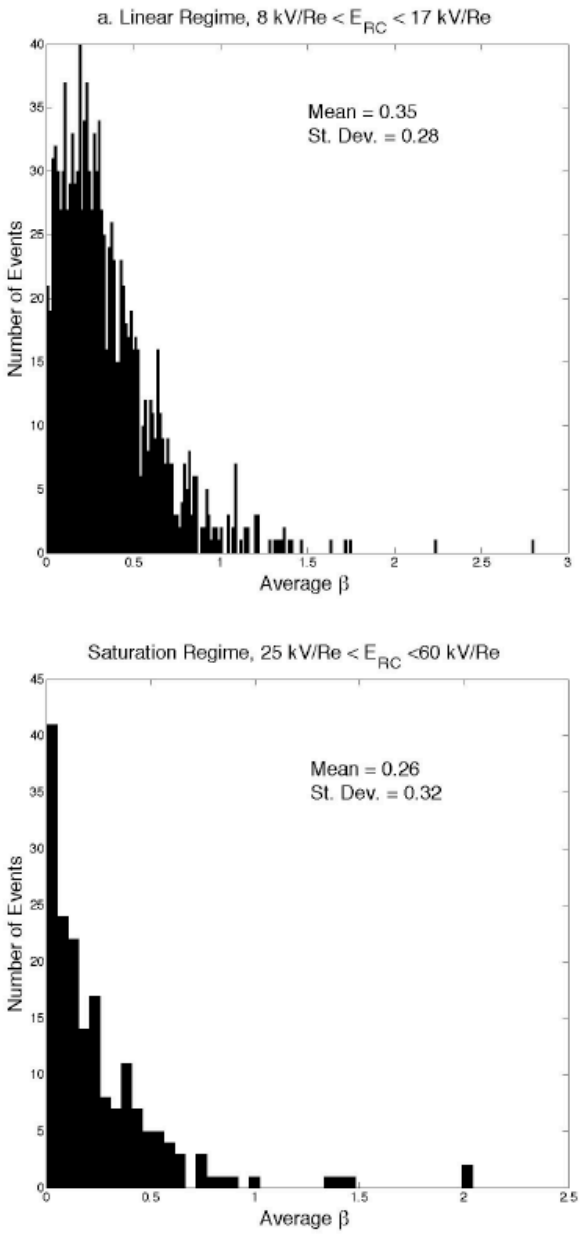

Figure 4.10: Histograms showing the β distribution for the the E_{RC} ranges of a) $8kV/Re < E_{RC} < 17kV/Re$ and b) $25kV/Re < E_{RC} < 60kV/Re$. The mean values of β in each are a) 0.35 and b) 0.26 with a standard deviation of a) 0.28 and b) 0.32.

To investigate the effect of plasma β on Φ_{RC} during strong driving, events with E_{RC} between 18 and 60 kV/Re were binned based on solar wind plasma β. The stability criteria was that the E_{RC} stay between 18 and 60 kV/Re and that β stay

between its specified maximum and minimum value. Overlapping bins were used to ensure the best possible view of the behavior of Φ_{RC}. Figure 4.11 shows how the reverse convection potential varies with respect to β, as well as the mean E_{RC} for each β bin. The average patterns used to generate this plot are given in Appendix A. While the mean E_{RC} in each bin stays constant, as β increases, there is an apparent increasing trend for Φ_{RC}. At extremely low β, there also seems to be larger Φ_{RC} values, but with the significantly stronger E_{RC} for the $0 < \beta < 0.05$ bin, no definite conclusions can be made.

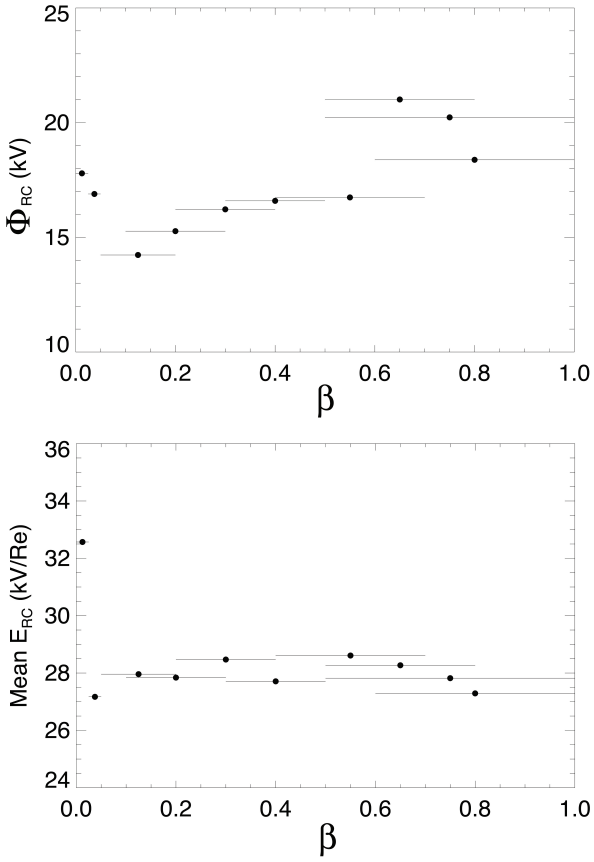

Figure 4.11: Statistics on the reverse convection potential for E_{RC} driving in the saturation regime and varying beta. Top is the reverse convection potential and bottom is the mean E_{RC} for each β bin.

It should also be noted that for $\beta > 1.0$, the potential pattern gets too distorted to

discern a reverse convection potential. This is most likely due to the magnetosphere being highly compressed during high-β events, as high-β often corresponds with a high solar wind density and therefore larger dynamic pressure.

4.6 Summary and Discussion

The results presented in this study elucidate on the behavior of the four cell convection pattern under northward IMF. It is apparent that while Φ_{RC} under northward IMF is much smaller than Φ_{PC} under southward IMF, their respective electric fields are likely comparable. It is therefore useful to discuss transpolar potential saturation in terms of polar cap electric field in addition to potential. It also indicates that there may be a connection between the saturation phenomena under northward IMF and southward IMF, as they seem to have a similar polar cap electric field limit.

The seasonal variation of the four cell convection pattern under northward IMF was also investigated. While the viscous potential cells in the pattern become much stronger under low conductivity winter months, the opposite seems to occur for the NBZ cells. This indicates that the NBZ currents under "saturated" conditions do not act like a constant current generator, as is often suspected for the saturated region 1 system under southward IMF. The reason for this has yet to be determined.

In recent years, several possible explanations for the saturation of Φ_{PC} under southward IMF have been put forth. One such explanation is that the strength of region 1 field aligned currents increase until their $\mathbf{J}X\mathbf{B}$ force replaces that of the Chapman-Ferraro current system as the main counter to solar wind ram pressure (*Siscoe et al.*, 2002a). Similar models also rely on strong region 1 field aligned currents which erode the magnetopause, limiting reconnection (*Siscoe et al.*, 2004). Since NBZ currents are generated by lobe reconnection on the night side of the cusp,

these two mechanisms are unlikely candidates to be the source for the saturation of the reverse convection potential.

Another hypothesis relates to the idea that saturation occurs at low solar wind Alfvènic Mach number. In this model, Alfvèn wings form in the magnetosphere, and their conductivity reduces the electric potential across the polar cap (*Ridley*, 2007; *Kivelson and Ridley*, 2008). Since the solar wind Alfvèn speed depends on the magnitude of the IMF and not the direction, Alfvèn wings should form under northward IMF and have the same effect on Φ_{RC}.

It was demonstrated through Figures 4.7, 4.8 and 4.9 that saturation of the reverse convection potential still occurs at nominal M_A. While this does not discount the possibility of Alfvèn wings forming in the magnetosphere under northward IMF, it does indicate that they are not the fundamental mechanism by which the reverse convection potential saturates.

With regards to solar wind plasma β, its distribution is comparable in both the linear and saturated regimes of Φ_{RC}. However, as β increases, the average Φ_{RC} over the saturated regime also seems to increase. If the β in the solar wind impacts the β in the magnetosheath, as suggested by *Scurry et al.* (1994), then it could point to the sheath control mechanism relating to the reverse convection potential. It will therefore be worthwhile to investigate how the polar cap potential saturation phenomenon overall is related to plasma β, most especially in the magnetosheath.

It is evident that at present there is much to learn about the behavior of the magnetosphere and ionosphere under northward IMF. It appears that coupling can be just as strong as in southward IMF, but that its effects are much more localized. Also, many of the hypotheses presented for saturation under southward IMF do not apply to the reverse convection potential. Future studies should be implemented

to compare these two orientations of the IMF, as well as to determine the cause of electric field saturation in the polar cap.

CHAPTER V

POLAR CAP ELECTRIC FIELD SATURATION DURING IMF Bz NORTH AND SOUTH CONDITIONS

In the previous chapter, it was demonstrated that while the reverse convection potential, on average, saturates at approximately one fifth to one fourth of the saturation potential under southward IMF, there is reason to believe that the electric field across the reverse convection cells is the same as the saturation electric field across the polar cap during periods of southward IMF. This implies that the polar cap electric field may be a more useful metric than potential in a unified understanding of Solar Wind-Magnetosphere-Ionosphere coupling.

It was also demonstrated that the average reverse convection electric field during the saturation regime of driving was 11.5 mV/m for winter and at 19 mV/m for the summer hemisphere. This is the opposite of what has been expected if it is assumed that the NBZ current magnitude is solely a function of solar wind-magnetosphere coupling, and is the opposite of what has been observed for southward IMF. Since the previous chapter only used a single statistical potential pattern from which to derive this conclusion, further study is needed to observe the overall trend. However, it is speculated that NBZ reconnection efficiency is reduced in the northern hemisphere

during winter since the cusp is tilted away from the sun.

Further, the saturation polar cap and reverse convection potentials discussed in Chapter 4 are smaller than what have been measured by DMSP Satellites (*Hairston et al.*, 2005; *Sundberg et al.*, 2009). Since the method for calculating the potential is much different for SuperDARN, it will prove useful to look at the radars velocity measurements as a proxy for the polar cap electric field and see how those compare with observations made by DMSP.

The purpose of this study is to build upon the previous results and compare the statistical saturation electric fields of northward and southward IMF. SuperDARN line of sight velocity (VLOS) measurements in the dayside high latitude ionosphere near magnetic noon will be analyzed for both northward and southward IMF for winter, summer and equinox conditions in order to determine how the saturation trends compare for both northward and southward IMF.

5.1 Methodology

5.1.1 Solar Wind Selection Criteria

For southward IMF, the Kan-Lee coupling function described in Chapter 2, E_{KL}, was used as an approximation of the effective interplanetary electric field (IEF) coupled into the polar cap via magnetic reconnection. For northward IMF, E_{RC} from chapter 2 was used. Using E_{KL} and E_{RC}, events can be found that fit specific criteria. In order to compare VLOS measurements for northward and southward IMF, events were found using propagated 1-minute data available through the OMNI database from 1998 to 2007 (*King and Papitashvili*, 2005). For both IMF orientations, stability criteria were placed on E_{KL} and E_{RC} such that the following condition was satisfied.

$$\frac{|\Delta E_i|}{\tilde{E}_i} < 0.25 \tag{5.1}$$

Where E_i is E_{KL} for southward IMF or E_{RC} for northward IMF, $|\Delta E_i|$ is the range in E_i and $\tilde{E}_i$ is the mean E_i over an event. For all events from which VLOS measurements were obtained, the stability criteria given in Equation 5.1 was required to be met for at least 50 minutes.

It should be noted that under northward IMF, the IMF B_Y component can drastically impact the prominence of reverse (sunward) convection. The reader is referred to chapters 2 and 3 to see that the choice of n=4 for E_{RC} allows one to minimize the effect of B_Y while increasing B_Z during event selection.

5.1.2 SuperDARN Line of Sight Measurements

If the convection in the F-region of the ionosphere is assumed to be mostly due to $\mathbf{E} \times \mathbf{B}$ drift and the geomagnetic field is assumed to be roughly constant, the polar cap electric field can be assumed to be directly proportional to the ionospheric convection velocity. In order to obtain the convection velocity in the polar cap, line of sight velocity measurements using the Super Dual Auroral Radar Network (SuperDARN) will be used (*Chisham et al.*, 2007). The major mechanism by which these VLOS measurements are obtained is through backscatter from field-aligned density irregularities which convect with the $\mathbf{E} \times \mathbf{B}$ drift of the plasma in the F region of the ionosphere (*Ruohoniemi et al.*, 1987). An advantage to using SuperDARN is that the radars operate continuously and provide substantial spatial coverage of the polar cap, and thus one can perform a significant statistical study.

In order to get a good comparison between the VLOS measurements under northward and southward IMF, restrictions on both the location of the measurements and

the LOS direction had to be placed. For northward IMF, all velocity measurements were restricted to between 11:15 and 12:45 MLT, with a northward LOS direction (within $\pm 10^{\circ}$ magnetic azimuth). This restriction increases the likelihood that the velocity vectors are located in the region of sunward flow under northward IMF. Under southward IMF, these velocity vectors should still be located in region of large scale anti-sunward flow, and the restriction on the LOS direction was extended to within $\pm 30^{\circ}$ magnetic azimuth to get wider coverage. For each 50 minute interval which met the stability criterion given in Equation 3, velocity measurements were taken for the last 30 minutes of the interval. This is to account for both error in the propagation time for solar wind data, as well as to allow the ionosphere time to respond to the solar wind driving.

To demonstrate the reason for this restriction on measurement location, average convection patterns for northward IMF and southward IMF are shown in Figures 5.1 and 5.2. These figures were calculated using the potential averaging method outlined in Chapter 3.

Figure 5.1 shows potential patterns for northward (left) and southward (right) IMF for events within 30 days of the summer solstice with E_{RC} and E_{KL} between 18 and 60 kV/Re, respectively. They are presented in AACGM MLAT-MLT format with the magnetic pole at the center and magnetic noon directed upward. The lowest latitude is 60 degrees for northward IMF and 50 degrees for southward IMF. The contour spacing is 1 kV for northward IMF and 3 kV for southward IMF. Color coding shows the number of gridded SuperDARN measurements that contributed to the calculation of each pattern. Figure 5.2 shows patterns in a similar format for events within 30 days of the winter solstice with E_{RC} or E_{KL} between 18 and 60 kV/Re. The saturation regime for northward and southward IMF are defined

based on northward IMF reverse (sunward) convection and southward IMF polar cap potential curves given in Chapter 3 and *Shepherd et al.* (2002) repectively. It should be noted that because these are spatially superposed and median filtered patterns, the polar cap and reverse convection potentials will be relatively low compared to other methods by which the potential can be measured. For this reason, these patterns are more useful for visualization and extracting overall trends than they are for precise quantitative measurement.

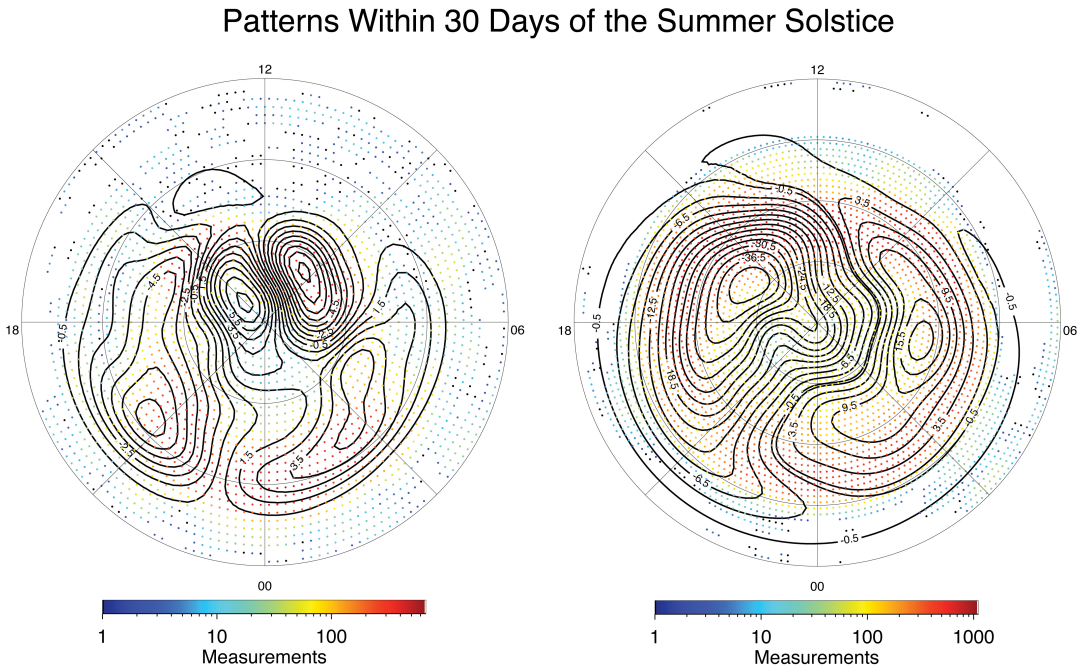

Figure 5.1: Calculated polar ionospheric convection patterns for the saturation regimes of northward IMF (left) and southward IMF (right) for binned events within 30 days of the summer solstice. The minimum magnetic latitude shown is 60 degrees for northward IMF and 50 degrees for southward IMF. The contour intervals are 1 kV for northward IMF and 3 kV for southward IMF.

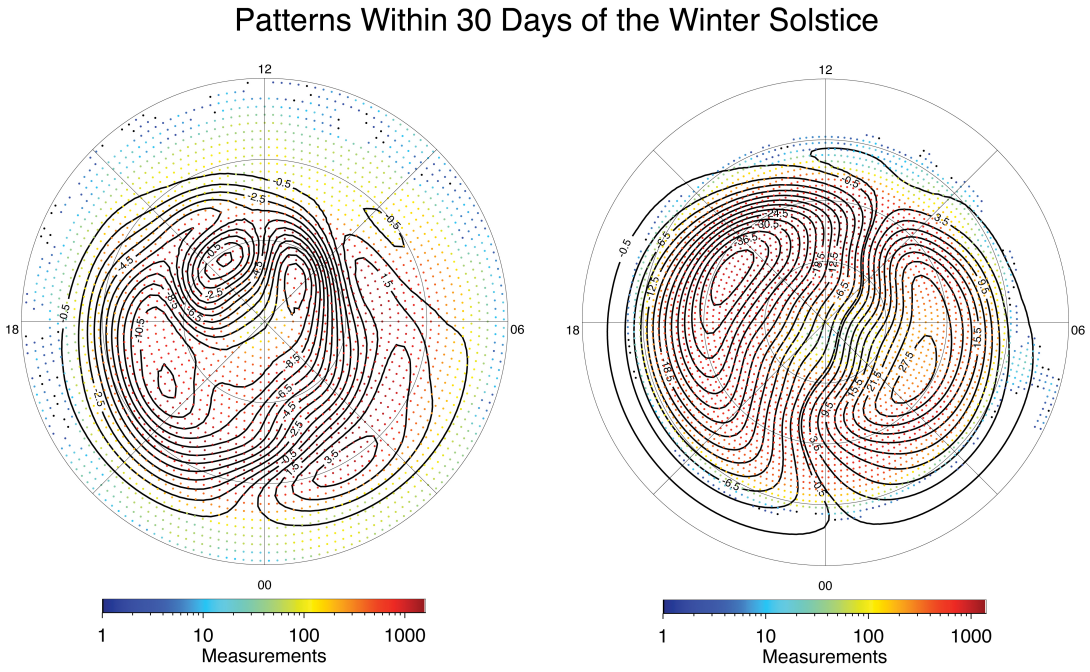

Figure 5.2: Calculated polar ionospheric convection patterns for the saturation regimes of northward IMF (left) and southward IMF (right) for binned events within 30 days of the winter solstice. The minimum magnetic latitude shown is 60 degrees for northward IMF and 50 degrees for southward IMF.

From both Figures 5.1 and 5.2 it can be seen that for both Summer and Winter, selecting velocity measurements at a latitude greater than 80 degrees and close to local noon will place measurements in the anti-sunward flow region for southward IMF and the sunward flow region for northward IMF. Its important to acknowledge, however, that the exact locations of these cells will likely vary from event to event due to factors such as changes in dynamic pressure and the value of IMF B_Y. It is therefore reasonable to expect that even with radar beams looking straight down the noon meridian in the anti-sunward direction, there will still be a wide amount of variation in velocity measurements.

Figure 5.3 shows a histogram of the distribution of gridded line of sight (LOS) velocity vectors used in the present study under (a) southward and (b) northward

IMF. The maximum anti-sunward LOS velocity measured for southward IMF is 1401 m/s, while the maximum sunward LOS velocity measured for northward IMF is 1622 m/s. Lower values likely come from measurements where the radar beam was not exactly parallel to the flow. Velocities in the opposite direction to that expected (sunward for southward IMF and anti-sunward for northward IMF) come from smaller values of the IEF coupling functions where the IMF By component has more of an impact. These flows could also be due to small scale flow structures which appear in the field of view of the radars. One explanation for the less smooth distribution in the northward IMF histogram is that the NBZ cells are competing with flows due to viscous convection in the opposite direction. Under northward IMF, the SuperDARN radars with the specified measurement position and beam direction see sunward flow 87.4% of the time. Under southward IMF, the radars see anti-sunward flow 88.6% of the time. This demonstrates that for northward IMF, reverse (sunward) convection is highly significant, and is observed for a majority of the time. For the remainder of this study, only sunward flows for northward IMF and anti-sunward flows for southward IMF will be examined.

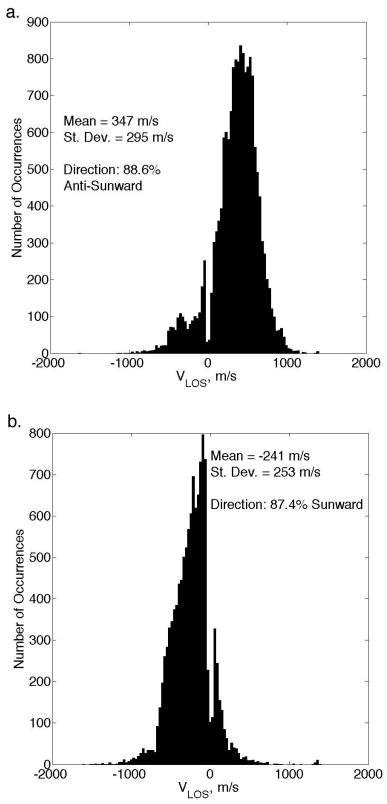

Figure 5.3: Histograms of SuperDARN gridded LOS velocity magnitude measurements for (a) southward and (b) northward IMF. Measurements were take at locations northward of 80 degrees magnetic latitude using radar beams with an anti-sunward LOS direction between 11:15 and 12:45 MLT.

Both distributions of velocity measurements are well within SuperDARN's measurement capabilities. For the maximum interpulse period used by SuperDARN (2.4 ms) and a carrier frequency of 14.6 MHz, the aliasing velocity of a SuperDARN radar will be around 2140 m/s. With a carrier frequency usually between 12 and 14 MHz and an interpulse separation which can be as low as 1.8 ms, SuperDARN typically can measure even larger LOS velocities if they exist.

5.2 Saturation of the Average Polar Cap Electric Field for Northward and Southward IMF

In order to obtain an understanding of polar cap electric field saturation under both southward and northward IMF, studies will be done by season. There are several reasons to do this. First, the region of reverse (sunward) convection under northward IMF are on the dayside of the high latitude ionosphere. Due to increased photo-ionization, the average conductivity around the sunward flow for northward IMF could be significantly larger than the average conductivity across the center of the polar cap under southward IMF. Thus, in order to better compare the saturation average electric field (AEF) for northward IMF, seasonal variations must be taken into account.

Further, Chapter 4 demonstrated that average reverse convection potential in the "saturation" regime of driving under northward IMF was significantly smaller near the winter solstice than it was near the summer solstice. If one assumes that lobe reconnection under northward IMF is equally effective for all seasons, leading to equal strength in NBZ currents, this result is counter intuitive. By Ohm's law, in the higher conductivity summer hemisphere, there should be a weaker electric field than in the low conductivity winter hemisphere given the same magnitude of electric current. This is not the case observed here. Thus, examining the overall trend of the reverse convection electric field for all seasons will be especially useful. We will divide our measurements into three seasons. We define summer as the months of May through August, winter as the months of November through February, and equinox as the months of March, April, September and October.

In order to obtain trends in convection velocity under northward IMF for each season, several bins of solar wind-magnetosphere coupling were used. Tables 5.1 and 5.2 at the end of this chapter show the number of VLOS measurements used in the present study for southward and northward IMF, respectively. The first column

is the range of coupling function (E_{KL} and E_{RC}) for each bin, and the subsequent columns are the number of measurements contributing for winter, equinox and summer. Entries with a dashed line indicate that the particular bin for the row was not used in the figure for that column's season. It can be seen that a large number of velocity measurements were used in this study.

Figure 5.4 shows plots of VLOS binned by IEF coupling function for (a) southward IMF and (b) northward IMF for the months of may through august. While there is a lot of variation in the saturation regime of driving, on average the maximum seems to be around 400 m/s for southward IMF and around 500 m/s for northward IMF. If the geomagnetic field at the point of measurement is assumed to be roughly constant at a value of 60,000 nT, then the saturation AEF is approximately 30 mV/m for northward IMF and approximately 24 mV/m for southward IMF. SuperDARN tends to get less coverage during summer months, and therefore several steps had to be taken to improve statistics. For northward IMF, the stability criteria given by Equation 3 was relaxed to allow 30% variation in E_{RC} per event for the "saturation" regime (E_{RC} between 30-35, 25-35, 35-40, and 30-40 kV/Re). For Southward IMF, the stability was relaxed to 30% for all values of E_{KL}.

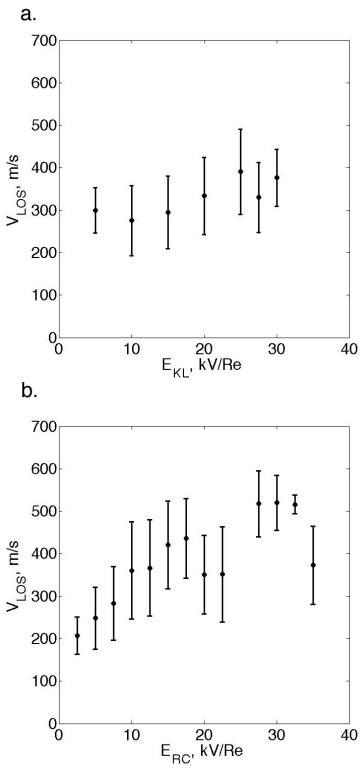

Figure 5.4: VLOS measurements with events in the months of May through August. (a) Plot of anti-sunward VLOS measurements for southward IMF plotted against E_{KL}. (b) Plot of sunward VLOS measurements for northward IMF plotted against E_{RC}. The dots represent the average VLOS for each bin of E_{KL} and E_{RC} and the overall length of the error bars are the standard deviation in VLOS. The numbers attached to each error bar indicate the number of line of sight measurements which contributed to the data point.

In order to further examine the seasonal discrepancy first observed in Chapter 4, plots of VLOS binned by IEF coupling function for (a) southward IMF and (b) northward IMF are given for the months of November, December, January and February in Figure 5.5. For southward IMF, the average velocity reaches 500 m/s, with the standard deviation stretching well beyond 600 m/s. This is the expected result for a constant current generator, as the average electric field is larger in the winter than in the summer. For northward IMF, the average velocity is closer to 300 m/s in the "saturation" regime, and doesn't seem to have a lot of variation.

These velocities correspond approximately to a saturation AEF of 30 mV/m for southward IMF, and a saturation AEF of 18 mV/m for northward IMF. This is in agreement with the result in Chapter 4. It is interesting to note that in Chapter 4, it was shown that the viscous potential was more prominent in the winter than in the summer under strong northward IMF. This seems to demonstrate that the viscous potential under northward IMF behaves in a similar manner to the polar cap potential under southward IMF. This brings up the question of why high latitude, sunward convection under northward IMF behaves differently.

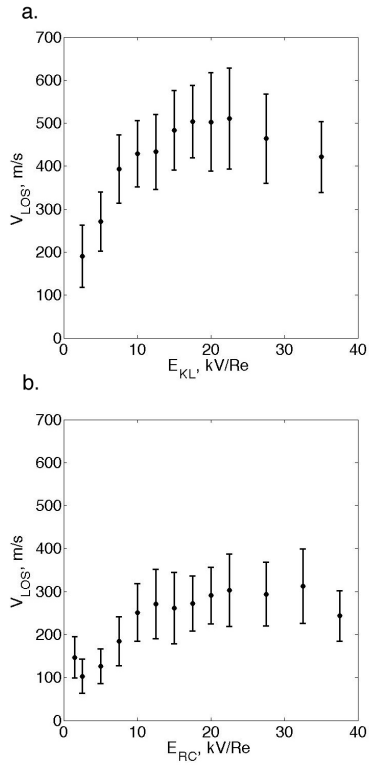

Figure 5.5: VLOS measurements with events in the months of November, December, January and February. (a) Plot of anti-sunward VLOS measurements for southward IMF plotted against E_{KL}. (b) Plot of sunward VLOS measurements for northward IMF plotted against E_{RC}. The dots represent the average VLOS for each bin of E_{KL} and E_{RC} and the overall length of the error bars are the standard deviation in VLOS. The numbers attached to each error bar indicate the number of line of sight measurements which contributed to the data point.

One thing to consider is how the AEF behaves at approximately equinox conditions. Figure 5.6 shows plots of VLOS binned by IEF coupling function for (a) southward IMF and (b) northward IMF for the months March, April, September and October. The average VLOS for Southward IMF seems to peak around 500 m/s with the flows as strong as 650 m/s within the standard deviation, while the average reverse convection VLOS for northward IMF peaks around 420 m/s with flows up to 500 m/s within the standard deviation. This corresponds to an approximate saturation AEF of 30 mV/m for southward IMF and 25 mV/m under northward IMF.

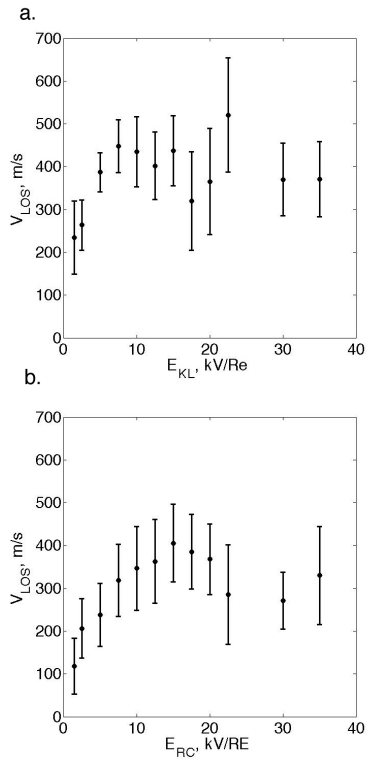

Figure 5.6: VLOS measurements with events in the months of March, April, September and October. (a) Plot of anti-sunward VLOS measurements for southward IMF plotted against E_{KL}. (b) Plot of sunward VLOS measurements for northward IMF plotted against E_{RC}. The dots represent the average VLOS for each bin of E_{KL} and E_{RC} and the overall length of the error bars are the standard deviation in VLOS. The numbers attached to each error bar indicate the number of line of sight measurements which contributed to the data point.

One hypothetical explanation for the seasonal behavior of the reverse convection cells would relate to the tilt of the earth as it varies by season. Near a solstice, the earth is tilted so that the summer hemisphere is facing more towards the sun than the winter hemisphere. It is possible that the geometry of reconnection under northward IMF is drastically effected by this difference, reducing the effectiveness of lobe reconnection in the winter hemisphere. The sunward convection electric field thus maximizes as the north pole is tilted to face the Sun, or near the summer solstice. This is also demonstrated by the fact that under equinox conditions, the reverse (sunward) convection magnitude under northward IMF is on average smaller than the convection under southward IMF in the saturation regime of driving. The reduced effectiveness of lobe reconnection as the polar region tilts away from the sun could explain this discrepancy.

5.3 Discussion and Summary

Hairston et al. (2005) performed a study of polar cap potential saturation under Southward IMF using DMSP satellite drift-meter measurements and found the polar cap saturated at approximately 200kV. If one looks at the northern hemisphere DMSP passes during the October 29 and November 20, 2003 storms that *Hairston et al.* (2005) used to calculate the saturation potential, one can come up with an approximation for the average electric field across the potential patterns for each pass. By finding the two times when the DMSP Vy measurements change sign (the convection reversal boundaries) and multiplying the time change by the approximate DMSP speed (7.4 km/s), one can find the distance across the cells. In order to approximate the average electric field across the polar cap, one then divides the potential measured by DMSP by the distance across the cells. For 6 passes where

DMSP F13 saw potentials greater than 140 kV during these time periods, the approximate average electric field ranged from 20 to 42 mV/m. These electric field values correspond to an average convection velocity in the polar cap between 333 and 700 m/s for a geomagnetic field of 60,000 nT. Both of these convection velocities are comparable to the VLOS measurements obtained in the present study.

The results in this study demonstrate that the seasonal behavior for northward IMF and southward IMF are opposite. The reverse (sunward) convection AEF under northward IMF is stronger in the summer, and the cross polar cap AEF under southward IMF is stronger in the winter. In equinox conditions, the reverse (sunward) convection AEF under northward IMF is slightly smaller than the cross polar cap AEF under southward IMF. One possible explanation for this is that as the polar cap tilts away from the sun, the effectiveness of lobe reconnection under northward IMF decreases.

It is also apparent that while there is a stark difference between Φ_{RC} for northward IMF and Φ_{PC} for southward IMF, the drastically larger size of the polar cap under southward IMF allows for the corresponding electric fields to be comparable. While there is a large amount of variation by season, Figure 5.3 shows that the maximum observed reverse (sunward) convection velocity under northward IMF is comparable to the maximum observed anti-sunward convection velocity under southward IMF. Figure 5.3 also demonstrates that sunward convection on the dayside at high latitudes is observed by the SuperDARN radars 87.4% of the time the IMF B_Z component is greater than or equal to zero. This shows that reverse (sunward) convection under northward IMF is a statistically significant phenomenon, and is just as likely to be observed as the two cell pattern under southward IMF.

Several hypotheses for the saturation of Φ_{PC} have been presented in recent years.

The most well known is the Siscoe-Hill model of polar cap saturation, in which the strength of region 1 field aligned currents increase until their $\mathbf{J} \times \mathbf{B}$ force replaces that of the Chapman-Ferraro current system as the Earth's stand off against the solar wind ram pressure (*Siscoe et al.*, 2002a). Other hypotheses propose an effect of magnetopause erosion on the dayside reconnection rate, which in turn limits the polar cap potential (*Siscoe et al.*, 2004). Since both of these involve reconnection on the dayside of the magnetopause, it is unclear how they can be translated to northward IMF, where reconnection occurs in the lobes on the night-side of the cusp.

Other models have been proposed, including the Alfvèn wing hypothesis put forth by *Kivelson and Ridley* (2008). In the Alfvèn Wing model, saturation occurs under strong IMF magnitude and low Alfvènic mach number. Under these conditions, the tail vanishes and forms a wing-like structure, similar to those discussed by *Neubauer* (1980) for the Galilean satellite Io. These "wings" have a conductivity which is mismatched with the ionospheric conductivity, causing a partial reflection of the electric field imposed on the ionosphere. *Lyatsky et al.* (2010) also proposes that the saturation of the polar cap potential is related to the reflection of the merging electric field from the polar cap along open field lines via Alfvèn waves. Both of these models of saturation would imply that the saturation is actually due to a reflection of the electric field imposed on the ionosphere.

Koustov et al. (2009) found that for southward IMF, the saturation potential was up to 10 kV larger in the summer than in the winter. In the present study, for southward IMF, the average electric field across the winter pattern was actually larger than the average electric field across the summer pattern. Since the patterns derived in the present study come from direct line of sight velocity measurements near the center of the polar cap, and *Koustov et al.* (2009) used scatter plots of fitted

polar cap potentials for individual events, it is likely that the disagreement is an artifact of the difference in methods used.

The saturation effect can also depend on the coupling function chosen, and it is important to recognize that our selection of E_{KL} and E_{RC} were to keep our study consistent with previous studies of polar cap potential saturation. *Shepherd et al.* (2002) used the E_{KL}, and *Hairston et al.* (2005) and *Sundberg et al.* (2009) both used VBz. In recent years, there have been coupling functions developed which take into account for saturation effects, such as those given by *Kivelson and Ridley* (2008) and *Lyatsky et al.* (2010). The present study is not intended to examine these functions; however, future studies could take them into account to assist in testing the various models of polar cap potential saturation.

The result that the northward IMF reverse convection cells and the southward IMF convection pattern have the potential to reach the same average electric field points to the idea that the mechanism for polar cap electric field saturation leads to a limit on the amount of current which can be passed through the magnetosphere-ionosphere system before the system begins to resist increases in solar wind driving. In other words, polar cap potential saturation can be explained by a collective limitation in either the solar wind-magnetosphere coupling process and/or the magnetosphere-ionosphere coupling process. The present results suggest that the latter may be more important than previously realized. Detailed study of the overall current systems and the state of the magnetosphere during both northward and southward IMF will be necessary to determine the precise nature of the saturation phenomenon.

Table 5.1: Number of VLOS Measurements by Season and E_{KL} for Southward IMF

E_{KL}, kV/Re	Winter	Equinox	Summer
0-3	-	48	-
0-5	253	146	-
2.5-7.5	1183	752	-
5-10	2435	1486	-
5 - 15	-	-	673
7.5-12.5	4567	1688	-
10-15	4709	1389	-
10-20	-	-	1040
12.5-17.5	3348	672	-
15-20	2607	474	-
15-25	-	-	513
17.5-22.5	1762	586	-
20-25	1505	316	-
20-30	-	-	119
25-30	688	-	-
25-35	-	601	97
30-40	224	541	-
25-40	-	-	115

Table 5.2: Number of VLOS Measurements by Season and E_{RC} for Northward IMF

E_{RC}, kV/Re	Winter	Equinox	Summer
0-3	75	32	-
0-5	489	337	49
2.5-7.5	1060	591	196
5-10	1125	617	211
7.5-12.5	1337	743	374
10-15	1512	541	417
12.5-17.5	1181	875	318
15-20	764	1110	330
17.5-22.5	575	419	373
20-25	370	164	271
25-30	162	-	80
25-35	-	264	117
30-35	-	-	39
30-40	106	559	188
35-40	-	-	149

CHAPTER VI

INTER-HEMISPHERIC OBSERVATIONS OF DAYSIDE CONVECTION UNDER NORTHWARD IMF

In chapters 4 and 5, it was shown that under northward IMF, there was a drastic difference between the winter and summer saturation reverse convection electric fields. Near solstice, it has been hypothesized that direct merging between the IMF and lobe field lines only occurs in the summer hemisphere (*Crooker*, 1992). This reconnection leads to lobe field lines which drape over the dayside of the magnetosphere and extend past the winter hemisphere and into the solar wind. These over-draped field lines then merge with lobe field lines in the winter hemisphere through a process called "internal reconnection" (*Crooker*, 1992). *Watanabe et al.* (2005) predicted different geometric features for the reverse convection cells in the summer and winter hemisphere, as well as different particle precipitation features. In the summer hemisphere, where lobe field lines directly merge with the IMF, the traditional round NBZ cells called "lobe cells" form which circulate on open field lines. In the winter hemisphere, where lobe field lines merge with overdraped lobe field lines from the summer hemisphere, tilted NBZ cells centered on closed field lines form convection features called "reciprocal cells." The present study will also

use this terminology.

Using data from the Super Dual Auroral Radar Network (SuperDARN) and energetic particle spectrograms from the Defense Meteorological Satellite Program (DMSP), *Watanabe et al.* (2006) demonstrated these differences in ionospheric convection and magnetic field line topology under northward IMF by investigating one event in winter and one event in summer. They did not, however, provide a quantitative simultaneous comparison of the effectiveness of each form of magnetic merging due to lack of radar measurements from the southern hemisphere.

Chapter 4 statistically demonstrated that the electric field across the NBZ cells saturates in response to increasingly strong northward IMF. It was also found that the statistical saturated reverse convection electric field was significantly stronger in the summer than in the winter. Chapter 5 demonstrated that this is the opposite to the seasonal behavior of the ionospheric convection under southward IMF. It also is counter-intuitive if one assumes that lobe reconnection is equally effective for both seasons.

This chapter expands upon the work done by *Watanabe et al.* (2006) and myself in Chapter 5 by investigating, in detail, the simultaneous development of reverse convection in both hemispheres for a case of strongly northward IMF near the northern winter solstice during December 5, 2004. SuperDARN radar measurements are used to determine time series of the reverse convection velocity magnitude, and DMSP particle precipitation data is used to demonstrate how open-closed boundaries correspond to dayside convection in each hemisphere. It is shown that the features of lobe cells and reciprocal cells are observed, including a narrower "polar cap" and circulation on closed field lines for the winter (northern) hemisphere. It is also shown that the sunward (reverse) convection near MLT noon is approximately three times

as strong in the summer (southern) hemisphere. This suggests that internal reconnection with over-draped field lines is less effective in transmitting the solar wind dynamo electric field to the ionosphere than direct merging between lobe field lines and the IMF.

6.1 Methodology

6.1.1 Instruments and Data Sets

The polar cap convection measurements used in this study are obtained from the Super Dual Auroral Radar Network (SuperDARN) (*Chisham et al.*, 2007). SuperDARN radars measure the line-of-sight velocity ($\mathbf{V}_{LOS}$) of field-aligned plasma density irregularities which convect with the $\mathbf{E} \times \mathbf{B}$ drift of the plasma in the F region of the ionosphere (*Ruohoniemi et al.*, 1987). The network contains several continuously operating radars in the northern and southern polar regions, allowing for simultaneous study of the development of polar ionospheric convection in both hemispheres. In the present study, potential patterns will be derived from SuperDARN $\mathbf{V}_LOS$ data by using the "map-potential" method described in Chapter 2.

In order to determine appropriate open-closed field line boundaries for the NBZ cells, precipitating particle flux data from the Defense Meteorological Satellite Program (DMSP) are used (*Hardy et al.*, 1984). The present study uses the F13 and F15 satellites, which regularly pass over the polar cap in both hemispheres. Each of these satellites has the capability to measure the flux of precipitating electrons and ions within the 0.3 to 30 keV range (*Hardy et al.*, 1984). By observing where the energetic particle flux returns to values seen equatorward of the auroral zone, one can determine open-closed boundaries. This will be done in a manner consistent with the methodology used by *Watanabe et al.* (2006) to determine the open-closed

boundary features within the two different forms of NBZ cells.

6.1.2 Event Selection

The event being studied is on December 5, 2004, and it was chosen for several reasons. First, the IMF was strongly northward with a B_Z component greater than 20 nT for several hours. Second, there was good simultaneous coverage of the NBZ cells in both hemispheres by SuperDARN. Third, in both hemispheres, there was a pass by the DMSP F13 satellite which crossed over the NBZ cells and a pass by the DMSP F15 satellite which passed near the NBZ cells. Finally, the event occurred during a period where the dipole tilt was strong enough to have asymmetries in both conductivity and reconnection geometry between the hemispheres. These conditions allow one to investigate, in detail, both the dayside convection and particle precipitation characteristics during a period having both strongly northward IMF and a strong asymmetry between the conductivity and magnetic reconnection topology.

6.2 Results

6.2.1 Solar Wind and IMF Conditions

Figure 6.1 shows the IMF and solar wind bulk speed propagated to the Earth's bow shock (∼17 Re) using data from the OMNI database for the afternoon of December 5, 2004 (*King and Papitashvili*, 2005). The IMF B_Z component is strongly northward and greater than 20 nT for a majority of the period shown. The IMF B_Y component fluctuates between 0 and -10 nT throughout the duration of the event, but given that the magnitude is usually half of the IMF B_Z component, there shouldn't be too much impact on the formation of reverse convection in the polar ionosphere.

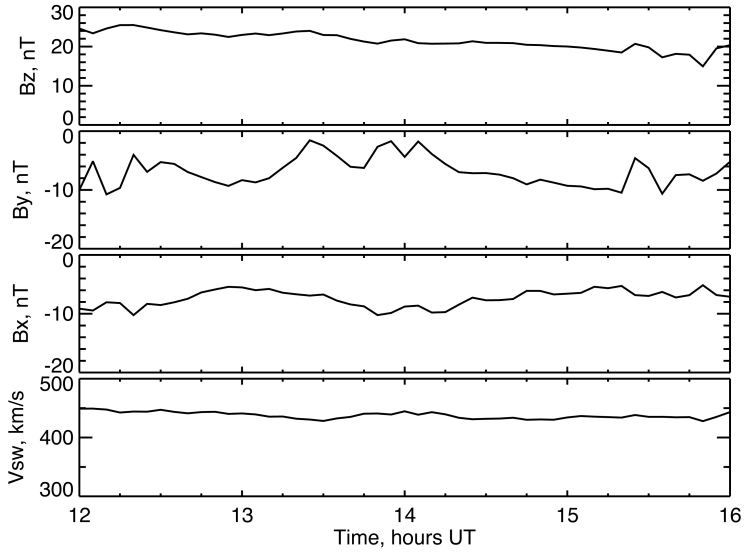

Figure 6.1: Propagated OMNI measurements of the upstream solar wind on December 5, 2004. The traces are, from the top: IMF B_z, B_y, B_x and the solar wind bulk speed, V_{sw}.

Finally, the IMF B_X component is consistently negative, which means that given no dipole tilt, the IMF field lines would reach the northern hemisphere before the southern. In the present event, however, the angle between the YZ plane and the IMF is between 14 and 21 degrees, which will result in a quasi-perpendicular geometry at the nose of the Earth's bow shock. Under normal solar wind conditions, this corresponds to a bow shock compression ratio greater than three, which amplifies the IMF B_Y and B_Z component in the magnetosheath, while B_X remains approximately constant across the shock (*Burgess*, 1995). This further reduces the angle between the IMF and the YZ plane in the magnetosheath to closer to 6.5 degrees. Combining this scenario with the fact that the IMF in the magnetosheath will drape over the magnetosphere, it is reasonable to assume that the IMF B_X component should not offset any dipole tilt effect, especially near solstice conditions where the dipole tilt is greater than 20 degrees.

Given the solar wind bulk speed, V_{SW}, and IMF B_Z in Figure 6.1, the component of the interplanetary electric field (IEF) which will merge with lobe field lines at the cusp of the magnetosphere can be approximated by $E_{SW} \sim V_{SW} B_Z$. Given a bulk speed of approximately 450 km/s and a northward component of the IMF of approximately 20 nT, this leads to an approximate merging E_{SW} of 9 mV/m or 58 kV/Re. This electric field strength is well above the approximate threshold of 3 mV/m or 20 kV/Re where the reverse convection electric field has been shown to saturate (*Sundberg et al.*, 2009, Chapter 3). This event will therefore be optimal for observing the seasonal asymmetry in reverse convection electric field saturation observed statistically in Chapters 4 and 5.

6.2.2 Ionospheric Convection Observed by SuperDARN

Around 13:15 UT, the SuperDARN radars in the southern hemisphere moved into a position where they had good coverage of the NBZ cells. This allowed for the simultaneous observation of the reverse convection potential pattern for both hemispheres. Figure 6.2 shows the dayside polar cap potential patterns for both hemispheres at 15 minute cadence for 13:15-14:00 UT. Each plot is presented in AACGM MLT-MLAT format with magnetic noon directed up the page. The lowest latitude shown is 60 degrees and contour spacing is 3 kV. The grey dots indicate positions of gridded SuperDARN $\mathbf{V}_{LOS}$ measurements.

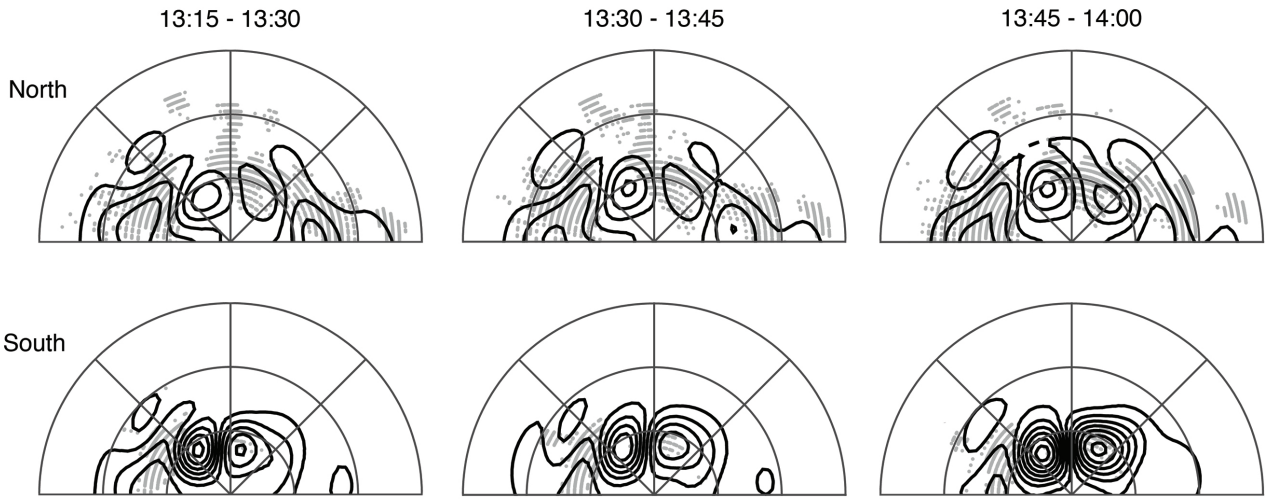

Figure 6.2: Dayside convection patterns for the northern (top) and southern (bottom) hemispheres during December 5, 2004, determined using SuperDARN ionospheric plasma velocity measurements. The plots are presented in AACGM MLT-MLAT format with magnetic noon directed up the page. The lowest latitude shown is 60 degrees. Contour spacing is 3 kV. The grey dots indicate positions of gridded SuperDARN $\mathbf{V}_{LOS}$ measurements.

From Figure 6.2, it is immediately apparent that the reverse convection potential is stronger in the southern hemisphere. This is particularly clear in the 13:45-14:00 pattern, where coverage of the reverse convection cells has increased in the southern hemisphere. During this time period, the northern hemisphere had a reverse convection potential of 14.3 kV while the southern hemisphere had a reverse convection potential of 38.2 kV. This observation is consistent with past studies which found that the reverse convection potential saturates at a larger value in the summer hemisphere than in the winter [Chapter 4, 5].

Further, there is an apparent difference in the MLT extent of the NBZ cells between hemispheres. This feature could be related to a process which has been discussed in the past by *Watanabe et al.* (2006), who proposed different types of reconnection geometry in each hemisphere. The larger "lobe cells" in the southern

(summer) hemisphere were thought to be a consequence of direct merging between the IMF and the geomagnetic lobe field lines. This merging results in lobe field lines from the summer hemisphere being "draped" over the dayside magnetosphere, where they can merge with lobe field lines originating in the winter hemisphere. Merging between over-draped summer lobe field lines and winter lobe field lines will theoretically produce "reciprocal cells" in the northern (winter) hemisphere. Whether or not the convection in the northern hemisphere contains reciprocal cells can be tested using particle precipitation data from DMSP, and which is done in section 6.2.3.

Polar cap potential patterns such as those in Figure 6.2 are calculated by performing a spherical harmonic fit on SuperDARN velocity data. While this is excellent for visualization purposes, actual quantitative comparisons of convection between hemispheres should be done using the velocity measurements themselves. Using SuperDARN, there are several different velocity measurements that can be made. Within each grid cell, there is a median line of sight velocity, $\mathbf{V}_{LOS}$, which is parallel or anti-parallel to the radar signal's look direction or **k**-vector.

Figure 6.3 shows a range-time plot for the 15th beam of the Stokkseyri radar's field of view in the northern hemisphere, during the period between 13:00 and 15:00 UT. In plots such as this, the measurements have not yet been median filtered in their respective spatial grid. Positive $\mathbf{V}_{LOS}$ measurements (blue) are toward the radar, and indicate sunward convection. This beam was chosen because it was closest to parallel to sunward reverse flow channel within the NBZ cells, and it observed the largest reverse convection velocity magnitude. Between a range of 1440 and 1755 km, large sunward velocities are observed. Figure 6.4 shows a similar range-time plot for the seventh beam of the Halley radar's field of view in the southern hemisphere.

With this beam, the radar is observing mostly sunward convection.

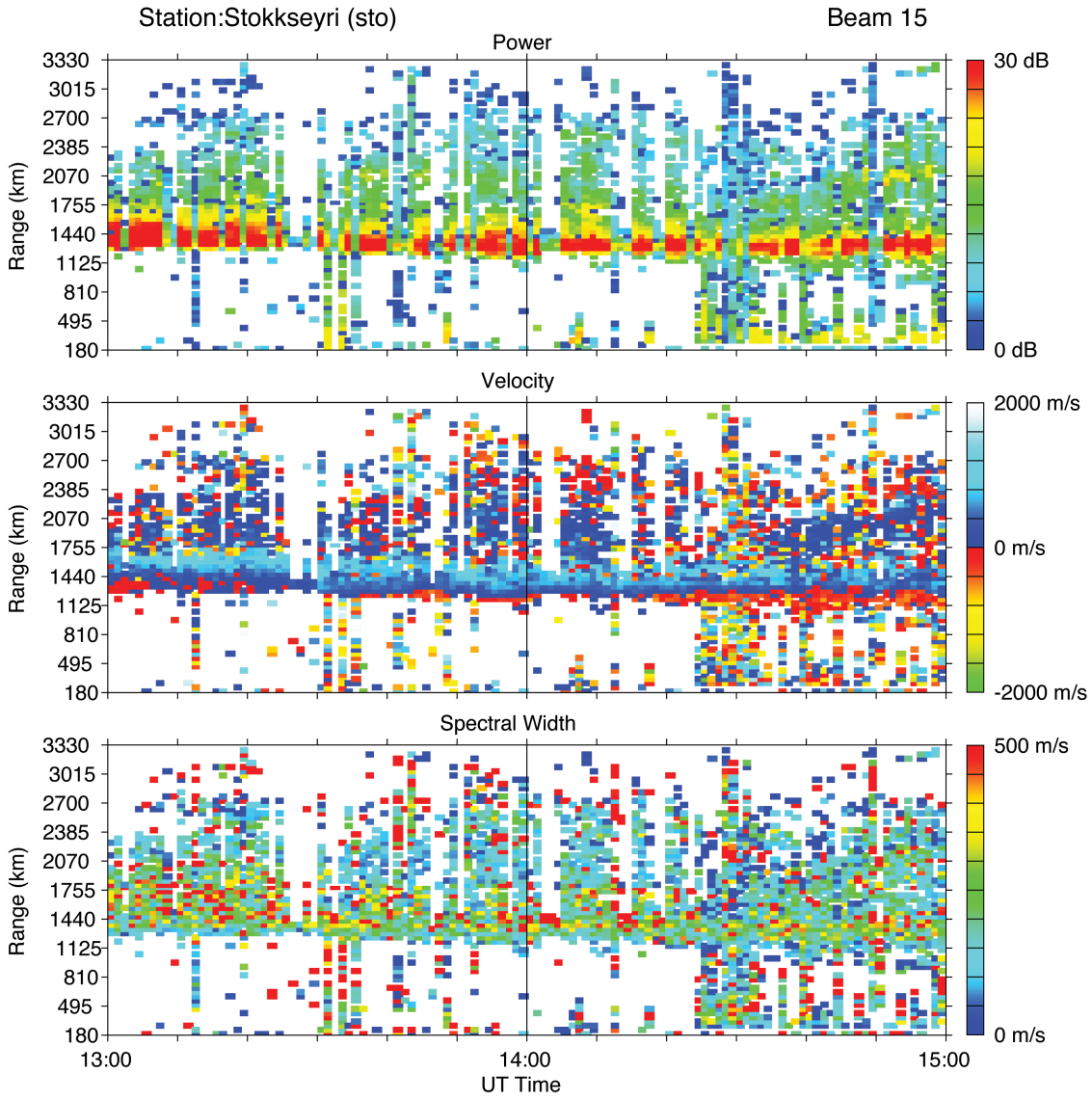

Figure 6.3: Range time plots for beam 15 of the Stokkseyri SuperDARN radar between 13:00 and 15:00 UT. Top is the backscattered power, middle is the line of sight velocity measurement ($\mathbf{V}_{LOS}$), and bottom is the spectral width for each measurement.

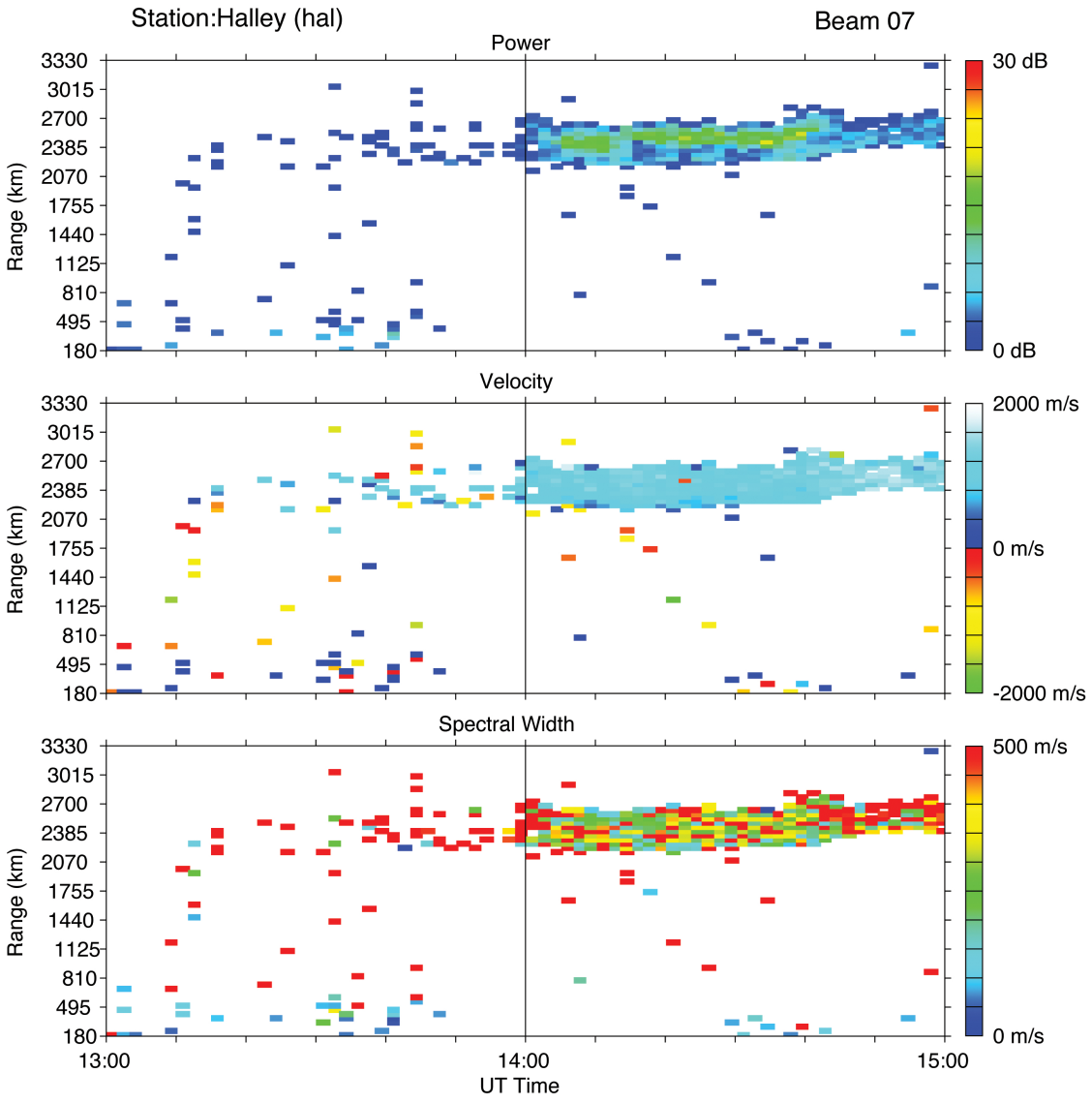

Figure 6.4: Range time plots for beam 15 of the Halley SuperDARN radar between 13:00 and 15:00 UT. Top is the backscattered power, middle is the line of sight velocity measurement ($\mathbf{V}_{LOS}$), and bottom is the spectral width for each measurement.

From Figures 6.3 and 6.4, it can be seen that the $\mathbf{V}_{LOS}$ magnitude in the reverse flow channel will average to larger values in the southern hemisphere. As is typical of SuperDARN radars, a larger backscattered power is seen in the northern (winter) hemisphere. The final parameter of interest is the radar spectral width. This is a measure of how perturbed the ionosphere is, and under optimal conditions, it can be

used to determine where the open-closed field line boundary is located *Wild et al.* (2004). In this case, however, there is a very high amount of variability in spectral width throughout the sunward flow channel. Therefore, particle precipitation data will prove more useful.

One difficulty with using $\mathbf{V}_{LOS}$ measurements from individual radar beams is that there is no guarantee that the beam is parallel to the flow. Therefore, a method to resolve the actual ionospheric velocity vectors using more than one radar is needed. If there are grid cells where two line of sight vectors from different radars overlap, the actual flow vector of the convection can be resolved. Due to spotty coverage in each radar's field of view, the likelihood of having direct overlap of measurements is low (*Provan et al.*, 2002). Another method for determining convection velocity measurements is to infer velocities from the fitted potential pattern, $\mathbf{V}_{FIT}$, using the map-potential method (*Ruohoniemi and Baker*, 1998).

A more rigorous method, which is used in the present study, is the calculation of "true vectors," $\mathbf{V}_T$ (*Chisham et al.*, 2002, Appendix A). "True" vectors are obtained by combining $\mathbf{V}_{LOS}$ vectors with the transverse component of the $\mathbf{V}_{FIT}$ vectors, which allows them to preserve the small-scale variations in $\mathbf{V}_{LOS}$ magnitude, as well as more accurately reproduce the magnitude of the velocities seen when there is overlap between radar fields of view (*Provan et al.*, 2002).

Figure 6.5 shows dayside convection patterns for the (a) northern and (b) southern hemispheres between 13:45 and 14:00 UT with "true" vectors superposed over the maps. Only "true" vectors within the sunward flow channel which had an angular separation from the $\mathbf{V}_{LOS}$ direction of less than 30 degrees are shown. We define the sunward flow channel as the region in the dayside ionosphere between 11:15 and 12:45 MLT at greater than 79 degrees MLAT. This criteria was verified through

visual inspection throughout the event. The potential maps are given in the same format as Figure 6.2. In both hemispheres, there is a clear sunward ("reverse") flow channel along the noon meridian at high latitudes in both hemispheres. To provide a basis for quantitative comparison, the magnitude of the"true" vectors from this flow channel, V_T, will be averaged at given time intervals to produce a time-series of the flow magnitude.

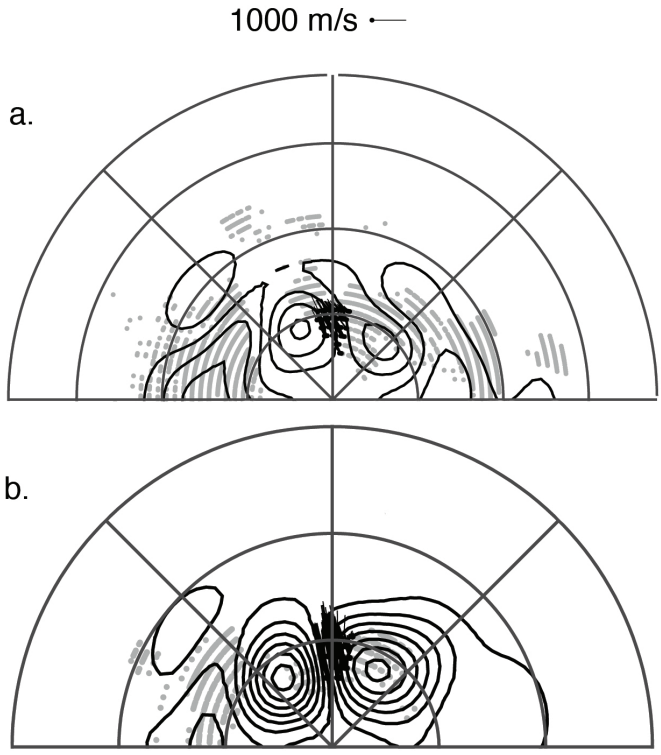

Figure 6.5: Dayside convection patterns for the (a) northern (winter) and (b) southern (summer) hemispheres. "True Vectors" are superposed on the patterns where the angle between the true vectors and the $\mathbf{V}_{LOS}$ measurements are less than 30 degrees.

Figure 6.6a shows the time series for average "true" vector magnitude in the sunward flow channel defined above in each hemisphere at 5 minute cadence. Error bars show the standard deviation in velocity magnitude per 5 minute interval. In addition, Figure 6.6b provides a running standard deviation in true velocity magnitude,

and Figure 6.6c shows the number of measurements within the sunward flow channel per 5 minute interval. Between 13:15 and 13:45 UT, there is an increase in sunward convection velocity in the southern hemisphere. This coincides with increases in radar coverage, with 4 available "true" velocities in the sunward flow channel at 13:15 and between 20 and 58 measurements starting at 13:45. In the northern hemisphere, radar coverage of the sunward flow channel begins to drop at around 14:30 UT. Therefore, the best period in which to compare the sunward convection velocity in each hemisphere is between 13:45 and 14:30 UT. The sunward convection averages between 900 and 1000 m/s in the southern (summer) hemisphere, and around 300 m/s in the northern (winter) hemisphere. There also is significantly larger running standard deviation in the sunward velocity magnitude for the southern hemisphere, though the reason for this is unclear.

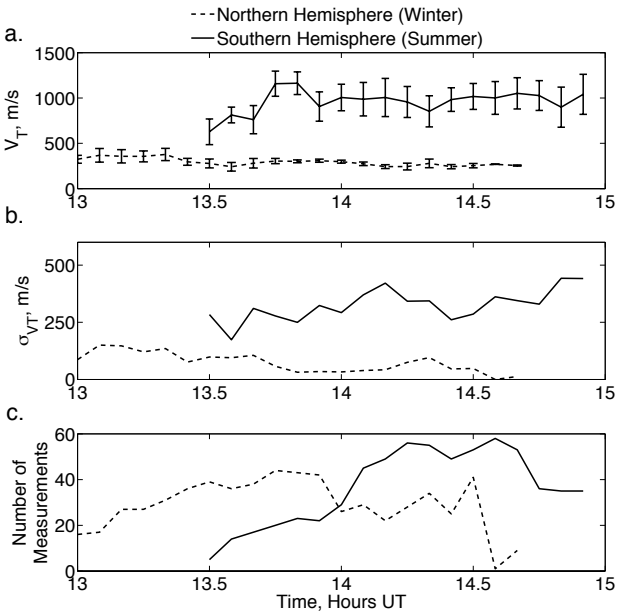

Figure 6.6: (a) Time series of the "true vector" magnitudes, V_T, measured in the reverse (sunward) flow channel for the northern (dashed line) and southern (solid line) hemispheres. Error bars are the standard deviation in V_T per 5 minute interval. (b) Time series of the "true vector" standard deviation, σ_{VT}, measured in the reverse (sunward) flow channel for each hemisphere. (c) Time series for the number of "true vector" measurements in the reverse flow channel for each hemisphere.

Seasonal or inter-hemispheric asymmetries in the polar cap convection and electric field are usually assumed to be related to ionospheric conductivity. In the summer hemisphere, the polar ionosphere is illuminated by the sun, leading to a larger conductivity than in the winter. For southward IMF, the region 1 FAC magnitude has been observed to be about 1.5 times larger in the summer (*Christiansen et al.*, 2002). In spite of this, larger conductivity in the summer also seems to lead to weaker polar cap electric fields, as observed in Chapter 5. The opposite is observed in the sunward velocities shown in Figure 6.6. This implies that the reconnection which occurs in the winter hemisphere under northward IMF may not drive ionospheric convection as effectively as in the summer hemisphere.

6.2.3 Polar Cap Boundaries observed by DMSP

Watanabe et al. (2006) proposed two forms of NBZ cells under northward IMF. The first are commonly referred to as "lobe cells," which are a result of direct merging between the IMF and lobe field lines in the summer hemisphere. These cells are centered on regions of open field lines. These are not to be confused with viscous convection cells, which are also sometimes referred to as "lobe cells." In the winter hemisphere, much of the convection is driven by reconnection with over-draped lobe field lines from the summer hemisphere. This "internal reconnection" leads to another form of convection cell, called "reciprocal cells," which circulate in regions with closed field lines. In order to determine which kind of convection cell is seen in each hemisphere, particle precipitation data from the DMSP satellites may be used to determine the open-closed boundary.

Figure 6.7 shows time-energy spectrograms of electron and ion energy flux observed by the DMSP F15 (top) and F13 (bottom) satellites in the northern (winter) hemisphere. The F13 satellite passed through both reverse convection cells, and the F15 pass skimmed the afternoon reverse convection cell on the duskward side (see Figure 6.9. The F15 pass observes constant electron flux, as well as fairly constant ion flux centered around 2 keV. From the electron flux, it seems apparent that the F15 satellite passes almost entirely through a region of closed field lines. The F13 satellite requires more explanation. At approximately 13:05:06 UT, the satellite crosses an open-closed boundary. We define this as the point where the electron flux drops to pre-polar cap background levels, coinciding with a comparable drop in ion energy flux. Between this time and approximately 13:06, precipitation characteristics typical for the polar rain are observed (*Newell and Meng*, 1992; *Newell et al.*, 2008). At approximately 13:06:59, the satellite appears to pass back into the closed

field line region.

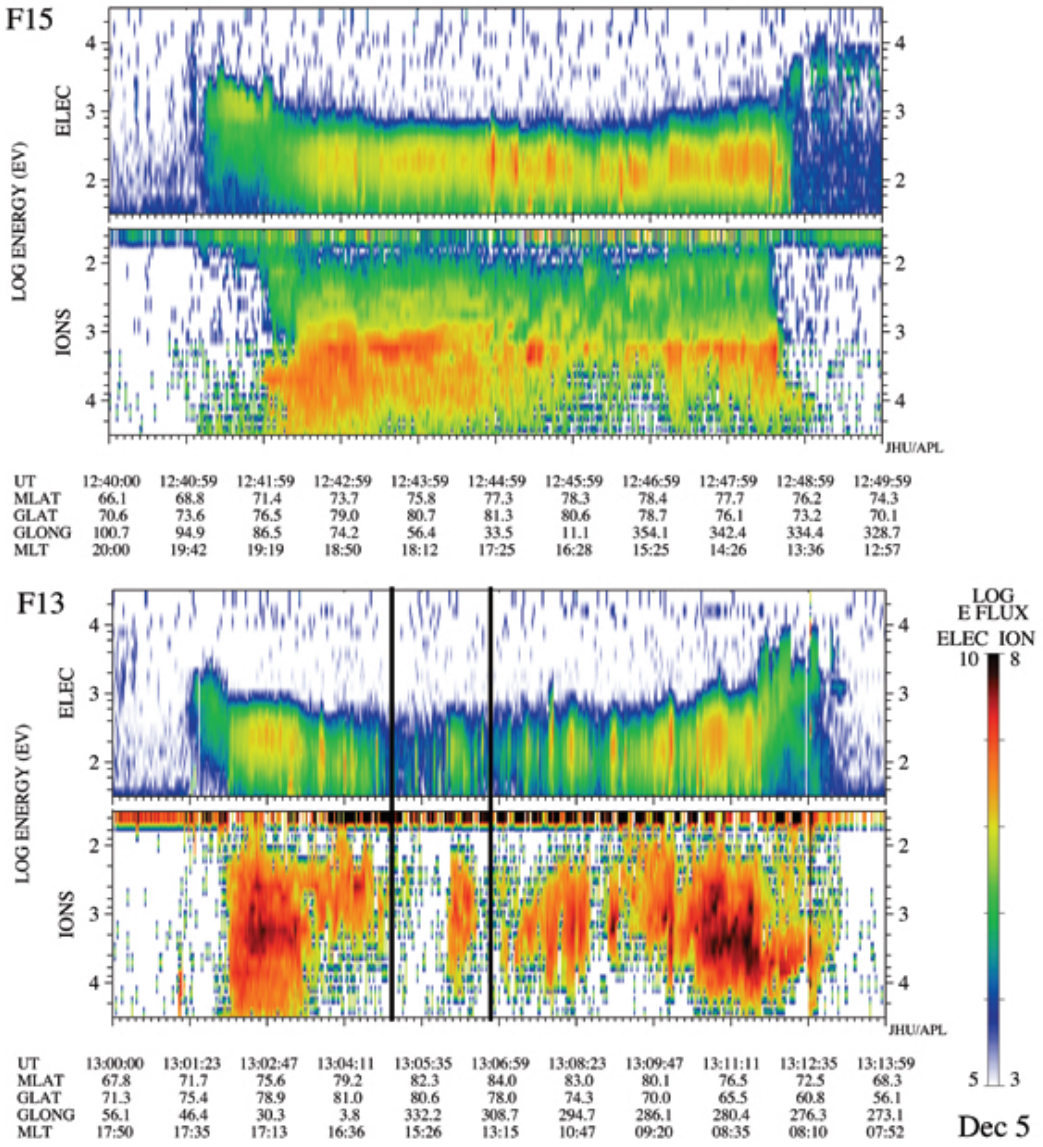

Figure 6.7: Spectrograms of ion and electron energy flux in the northern hemisphere along the trajectory of the F15 (top) and F13 (bottom) passes.

Figure 6.8 shows time-energy spectrograms of electron and ion energy flux observed by the DMSP F15 (top) and F13 (bottom) satellites in the southern (summer) hemisphere. The F15 pass shows asymmetry in both electron and ion precipitation, yet it appears to pass entirely through closed field line regions. The F13 pass is

more symmetric about local noon than in Figure 6.7, and shows the typical northward IMF summer particle precipitation characteristics observed by *Watanabe et al.* (2006). Between 13:57 and 13:59, signatures of energetic ions centered around approximately 1 keV are seen. These are magnetosheath ions which precipitate in areas of sunward convection, and have been invoked in the past to explain theta aurora (*Reiff et al.*, 1980; *Woch and Lundin*, 1992; *Crooker*, 1992). It is interesting to note that at the highest latitude, the distribution includes ions with energy greater than 10 keV are seen, which are not typical for ions of magnetosheath origin. It could be proposed that such energetic ions are accelerated from the reconnection site. Aside from this anomaly, which is at present unexplained, this DMSP pass shows the characteristics of open field lines mapping to the merging site in the magnetosheath, which has been observed in the past (*Watanabe et al.*, 2006). We identify the open field line region to be between 13:55:36 UT and 14:00:08 UT.

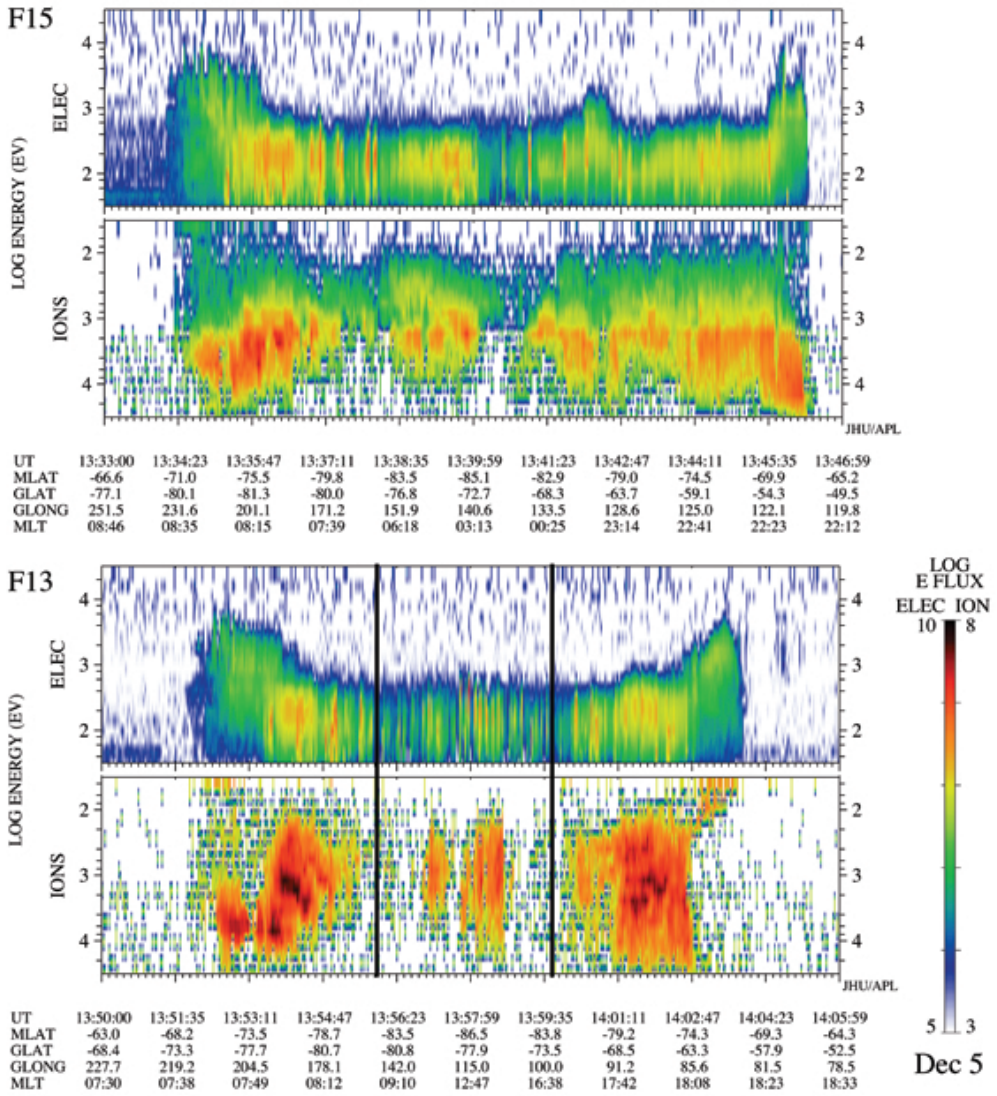

Figure 6.8: Spectrograms of ion and electron energy flux in the southern hemisphere along the trajectory of the F15 (top) and F13 (bottom) passes.

Figure 6.9 shows the trajectories of the DMSP passes in Figures 6.7 and 6.8 superposed over their corresponding average potential patterns. The blue lines indicate portions of the trajectory which are through closed field line regions, and the red lines indicate open field line regions (the "polar cap"). The respective boundaries were determined from Figures 6.7 and 6.8.

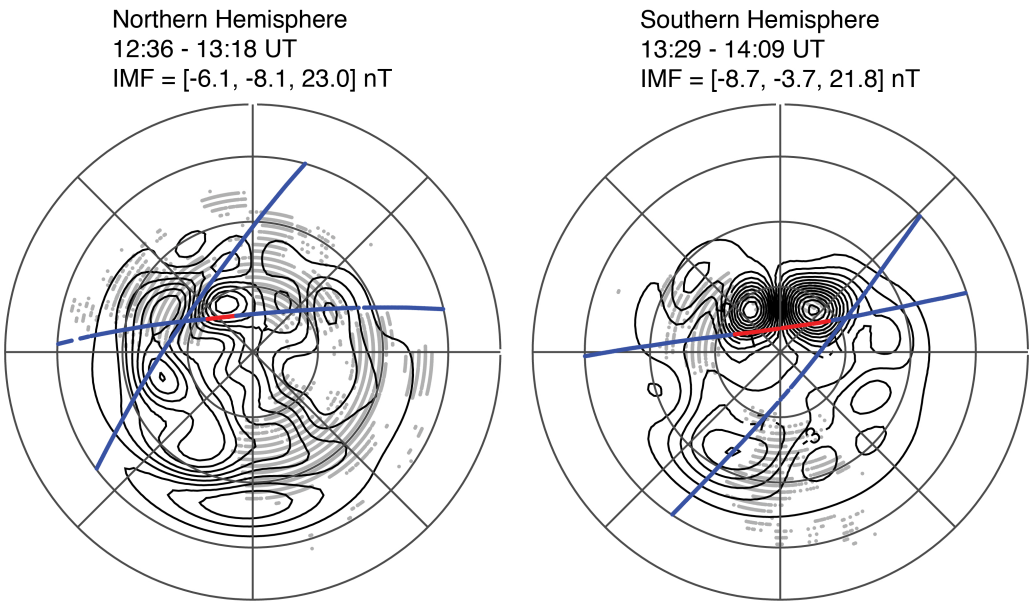

Figure 6.9: Maps of the DMSP trajectories and related regions for the northern (left) and southern (right) hemisphere. Blue regions along the satellite trajectories indicate regions of closed field lines, and red regions indicate the polar cap region which is characterized by magnetosheath particle precipitation due to reconnection with lobe field lines in the cusp. Contour spacing is 2 kV and the minimum latitude shown is 50 degrees.

In the southern hemisphere, the center of each NBZ cell appears to be on open field lines. This fits the characteristics of "lobe cells" that result from reconnection between the IMF and lobe field lines. For the northern hemisphere passes, a more complex interaction is occurring. The afternoon NBZ cell is more prominent than the morning, which is not typically observed for purely northward IMF, and the circulation is occurring on open field lines. The dawn-side convection cell, however, is centered on regions with closed field lines. This circulation on closed field lines suggests that it is a "reciprocal" cell and that part of the reconnection driving it is between winter lobe field lines and over-draped summer lobe field lines (*Crooker*, 1992; *Watanabe et al.*, 2005, 2006).

In order to explain the northern hemisphere morning-afternoon asymmetry in

NBZ cells, one should consider that the IMF B_Y component in Figure 6.9 is more strongly negative for the northern hemisphere passes. Figure 6.10 shows a diagram of the Earth's magnetosphere as viewed from the sun. The IMF in the diagram is northward with a significant negative IMF B_Y component. The blue field lines are over-draped summer lobe field lines due to magnetic merging in the southern hemisphere, and the red field lines are IMF field lines. The IMF B_Y component causes the over-draped field lines to be tilted towards the morning side of the northern hemisphere, leaving the evening side open to direct merging with the IMF. Therefore, internal reconnection primarily occurs on the dawn side, leading to reciprocal cells, while direct merging with the IMF primarily occurs on the dusk side, leading to merging cells.

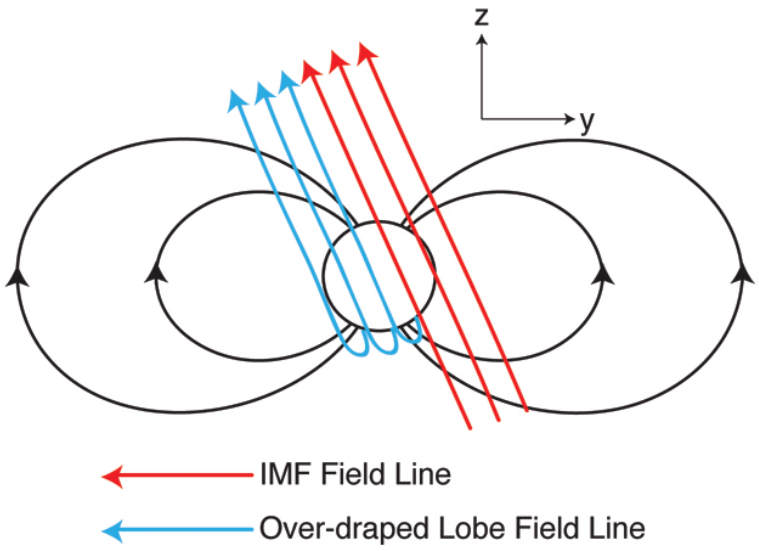

Figure 6.10: A diagram of the possible magnetic field line configuration during the northern hemisphere DMSP passes. The magnetosphere is viewed from the Sun, with red lines being IMF field lines, and blue lines being over-draped lobe field lines.

6.3 Summary and Discussion

The present study investigates the simultaneous development of the reverse convection speed and potential in both hemispheres on December 5, 2004. During this event, the IMF Bz was strongly northward ($\sim$ 20 nT) with a merging electric field well within the "saturation" regime of driving. It has been shown that the convection speed in the sunward flow channel was larger in the southern hemisphere by an approximate factor of three. Further, it has been demonstrated that part of the reverse convection pattern in the northern (winter) hemisphere contained circulation entirely on closed field lines. This is a signature of "internal" reconnection, which has been observed in the past by *Watanabe et al.* (2006).

There are several key differences between the present study and those done in the past. First, *Watanabe et al.* (2006) did not observe ion precipitation in the anti-sunward flow region in the winter hemisphere while the present study does. This could be, in part, due to the fact that in the present study, the northern hemisphere F13 and F15 passes coincide with a more strongly negative IMF B_Y component, which may result in a more open magnetosphere in the afternoon sector, as demonstrated in Figure 8. The IMF B_Y component was closer to zero in the northern hemisphere winter case examined by *Watanabe et al.* (2006).

Further, to the authors' knowledge, this is the first study to simultaneously compare the strength of convection in both hemispheres. *Watanabe et al.* (2006) investigated two separate events, one during northern hemisphere summer and one during northern hemisphere winter, and was mostly concerned with characterizing the boundaries in the polar cap and identifying reciprocal cells in winter. *Burke et al.* (1979) also found it difficult to observe reverse convection at all in the summer months, as did the reverse convection potential saturation study done by *Sundberg et al.* (2009).

This study also resolves a question regarding observations in Chapters 4 and 5, which saw the reverse convection potential and electric field saturating at larger values in the summer hemisphere than in the winter. This was compounded by the fact that Chapter 5 demonstrated the opposite response of the saturated polar cap potential and electric field under southward IMF. Chapter 5 suggested that the high latitude reconnection on the nightside of the cusp under northward IMF might be less effective in the winter hemisphere. The present study confirms that the reverse convection is significantly weaker in the winter hemisphere, and that part of the circulation is in regions of closed field lines. This suggests that in the winter hemisphere, a portion of the reconnection is "internal" merging between lobe field lines and over-draped lobe field lines from the summer hemisphere. Internal reconnection appears to be less effective at transmitting the interplanetary electric field into the polar cap than direct merging with the IMF.

As the next solar maximum approaches, there will be even more opportunities to simultaneously observe dayside convection in both hemispheres. PolarDARN radars have been built near the magnetic north pole, and there is an effort to establish more SuperDARN radars in the southern hemisphere (*Chisham et al.*, 2007). There is also an effort to deploy low power magnetometers on the antarctic plateau which will be magnetically conjugate to the magnetometer chain on the west coast of Greenland (*Musko et al.*, 2009). This increase in measurement capability will increase the probability that reverse convection can be observed in both hemispheres for a larger number of events. With this capability, more inter-hemispheric studies can be done over varying interplanetary and geomagnetic conditions.

CHAPTER VII

THE NON-LINEAR RESPONSE OF THE POLAR CAP POTENTIAL UNDER SOUTHWARD IMF - A STATISTICAL VIEW

The main purpose of this thesis is to empirically investigate the phenomenon of polar cap potential saturation. In Chapters 3-6, the non-linear response of the localized reverse convection potential was shown. This demonstrates that "saturation" is not confined to a single IMF orientation and that the response of field aligned currents depends heavily on the magnetic field line topology in the magnetosphere. This chapter returns to the overall polar cap potential under southward IMF, in order to investigate the existing models which try to explain the "saturation" phenomenon.

In recent years, several hypotheses have been presented to explain the non-linearity of the cross polar cap potential. One hypothesis is that there is a feedback mechanism whereby the magnetic field associated with the region 1 field-aligned currents reduces the strength of the Earth's magnetic field at the dayside magnetopause, limiting reconnection. This is commonly referred to as the Siscoe-Hill model (*Hill et al.*, 1976; *Siscoe et al.*, 2002b). This model also predicts a positive correlation between solar wind dynamic pressure and the polar cap potential, as the region 1 currents adjust themselves to replace the Chapman-Ferraro currents to stand-off the

solar wind (*Siscoe et al.*, 2002a). Another hypothesis is that there is a conductivity mismatch between the source electric field at the solar wind and the load in the ionosphere. This mismatch occurs as the Alfvènic mach number drops and the Earth's magnetosphere forms Alfvèn wings (*Ridley*, 2007; *Kivelson and Ridley*, 2008). In the Alfvèn wing model, a transmission coefficient for the electric field imposed on the ionosphere is given based on ionospheric conductivity and solar wind Alfvèn speed. Finally, there is a more recent model in the paper *Lopez et al.* (2010). They propose that lower Alfvènic Mach number (though not necessarily as low as required for the formation of Alfvèn wings) and increasing IMF magnitude leads to lower plasma beta in the magnetosheath. This, in turn, encourages the diversion of plasma flow around the flanks of the magnetosphere, which reduces the reconnection potential. Testing these predictions using ionospheric data-sets is a useful way of determining which model might be the most accurate. Therefore, the primary purpose of this study is to test the saturation models by examining the dependence of the CPCP on solar wind dynamic pressure, Alfvènic Mach number, and Alfvèn wing conductance. If the Siscoe-Hill model is the most accurate, one should see a strong positive correlation with solar wind dynamic pressure. Both the (*Lopez et al.*, 2010) and Alfvèn wing model should see strong positive correlation with the Alfvènic Mach number, though the formation of Alfvèn wings is dependent on critically low values. The Alfvèn wing transmission coefficient is dependent on Alfvèn wing conductance and ionospheric pederson conductance, and the results will depend on how both are measured.

In the past, polar cap potential saturation has been observed using data from both the Defense Meteorological Survey Program (DMSP) (*Hairston et al.*, 2003, 2005) and the Super Dual Auroral Radar Network (SuperDARN) (*Shepherd et al.*, 2002). With both data-sets, the overall trends were similar, but the CPCP values at

which saturation occurs were much larger in studies using DMSP than in those using SuperDARN. Detailed examination of co-located DMSP and SuperDARN velocities show they are largely consistent with each other once the difference in altitude between the measurements are considered (*Drayton et al.*, 2005). It is therefore reasonable to assume that the DMSP-SuperDARN CPCP differences might be related to the different methods used to process the data. DMSP CPCPs are obtained via a one-dimensional integration across the satellite trajectory with little or no error analysis, while SuperDARN CPCPs are obtained using two-dimensional least squares fitting weighted by the velocity errors. The end result is that SuperDARN potential measurements benefit from wide spatial distribution of measurements and good temporal resolution, but at the expense of finer spatial resolution. DMSP measurements benefit from higher spatial resolution, but have poor coverage and significantly poorer temporal resolution.

In order to get the most complete picture of ionospheric convection with which the CPCP can be calculated, it makes sense to combine both data-sets. Previous studies have done this in an ad-hoc manner and found anomalies and inconsistencies in the potential measurements. There are challenges, however, in merging DMSP and SuperDARN data to weight the datasets evenly and produce a time series free of anomalies. Overcoming these challenges is a secondary purpose of this study, as CPCP measurements from the merged data-sets will be used in order to investigate the major models of polar cap potential saturation.

Using measurements of both the solar wind and the ionospheric convection, the present study aims to investigate the polar cap potential saturation phenomenon. First, a demonstration of the merging of DMSP and SuperDARN data and its advantages will be done. Then, once consistent polar cap potential determinations

have been made, the extent of polar cap potential saturation will be correlated with various interplanetary parameters in order to test the various hypotheses to describe the phenomenon.

7.1 Data-sets and Methodology

For ionospheric convection measurements, the present study uses data from the Super Dual Auroral Radar Network (SuperDARN) (*Chisham et al.*, 2007) and the Defense Meteorological Satellite Program (DMSP) (*Rich and Hairston*, 1994). For measurements of upstream solar wind conditions, this study uses pre-propagated data from the OMNI database (*King and Papitashvili*, 2005). All of these data-sets and how they can be analyzed in order to investigate the saturation phenomenon need to be discussed in more detail.

7.1.1 The Super Dual Auroral Radar Network

A majority of the measurements throughout the polar cap used in this study were line of sight velocity (VLOS) measurements from the Super Dual Auroral Radar Network (SuperDARN) (*Chisham et al.*, 2007). From the VLOS measurements, an average polar cap potential pattern for a period can be calculated using a spherical harmonic fit. This fitting procedure has been described in *Ruohoniemi and Baker* (1998) as well as in *Shepherd et al.* (2002), and a summary shall be given here.

- The map of the polar cap is divided into 50 km by 100 km spatial bins. The main purpose of gridding the VLOS measurements is to remove artifacts in the convection patterns associated with the variable area of radar range-beam cells.

- VLOS vectors from SuperDARN radars measured during each period were then

placed in their respective spatial bin. This allows measurements throughout the event to be superposed to produce average convection patterns.

- Velocity vectors from a statistical model are then included in order to constrain the fitted polar cap potential pattern in areas with poor radar coverage. As long as a majority of the polar cap is covered by actual radar measurements, the model vectors do not have a significant impact on the value of the cross polar cap potential. The input to the statistical model is the IMF vector, which is obtained by averaging IMF data obtained from the OMNI database over the period for which the potential pattern is calculated.

- A potential pattern is then obtained by applying the spherical harmonic fitting technique to the resulting gridded velocity measurements and model vectors. Here, the electric field in the ionosphere is assumed to be the gradient of the electric potential, with equipotential lines that are the streamlines of the plasma convection (*Ruohoniemi and Baker*, 1998).

- The difference between the maximum and minimum of the potential pattern is taken to determine the cross polar cap potential.

One of the weaknesses to using SuperDARN is that as the magnetosphere-ionosphere system experiences stronger solar wind driving, the polar cap potential pattern can expand beyond the radars' field of view. For this reason, previous studies have tended to focus on low levels of saturation (*Shepherd et al.*, 2002, Chapter 5). While new SuperDARN radars are being built at mid-latitudes to rectify this problem, it must still be addressed when using data from the early 2000s solar maximum. Further, comprehensive spatial coverage for all events during strong driving is not guaranteed in the polar cap. Sometimes, only one of two convection cells is covered during a

given event. One way to deal with this is to add measurements from other data sets into the calculation of the polar cap convection pattern.

7.1.2 The Defense Meteorological Satellite Program

In the present study, plasma drift data from the Defense Meteorological Satellite Program (DMSP) is used to augment SuperDARN in the calculation of ionospheric convection patterns. DMSP is a constellation of sun-synchronous polar orbiting satellites which make measurements of various plasma parameters in the ionosphere (*Rich and Hairston*, 1994). The instrument used in the present study is the SSIES thermal plasma monitor, which contains an ion drift meter (IDM). Drift along the satellite track, as well as drift perpendicular to the track can be measured. For the present study, only the cross-track drift will be used, since these measurements are the most reliable (*Rich and Hairston*, 1994).

Traditionally, the polar cap potential is calculated from DMSP data by obtaining the ionospheric electric field from the ion velocity and magnetic field measurements. The electric field is then integrated over the satellite track in order to calculate the cross-polar cap potential pattern (*Hairston et al.*, 2005). Because the potential pattern is likely to change over the approximately 20 minute satellite track through the polar cap, the potential tends to be larger than zero at the end of the track. This offset is redistributed over the satellite pass in order to set the potential to zero at both ends of the satellite pass (*Hairston et al.*, 2005). In the present study, we have restricted the analysis to those DMSP passes which create a potential offset of less than 25% in order to ensure the stability of the polar cap potential pattern. Instead of using the traditional integration over the satellite track, the present study includes DMSP velocity vectors along with SuperDARN data in the spherical har-

monic analysis in order to obtain a 2-D convection pattern over the polar cap. The pre-processing required to ensure consistency between the data-sets will be discussed in detail in Section 7.2.

7.2 Merging SuperDARN and DMSP Data to Produce CPCP Measurements

Central to the study of polar cap potential saturation are measurements of ionospheric convection during strong solar wind driving. While under moderate solar wind driving, the SuperDARN radars observe much of the polar cap potential pattern, under strong solar wind driving, the pattern begins to expand beyond the radars field of view. Also, while SuperDARN radars exist throughout North America, Europe and Japan, there is a considerable gap in coverage over northern Russia. This means that at certain times of the day, the SuperDARN radars may have good coverage of only one convection cell. Having an extra data-set that can both provide measurements at mid-latitudes during strong driving and make up for local time gaps in radar coverage provides more reliable measurements of the storm time polar cap potential. If only DMSP data is used to measure the polar cap potential, there is no guarantee that the satellite's trajectory will cross through the exact location of the potential pattern's minimum and maximum. It is therefore desirable to find a way to combine both data-sets in order to get the most reliable picture of storm-time polar cap convection. *Baker et al.* (2007) did this in an ad-hoc fashion in order to demonstrate the mid-latitude capabilities of the Wallops Island radar, and the present study shall utilize this method with additional considerations on how to merge the two data-sets consistently for a large statistical study.

Combining both data sets does present some challenges, particularly with regard

to spatial and temporal resolution, difference in altitude between measurements, and weighing of uncertainties in the measurements. In order to demonstrate the effects of these factors, an event which occurs at moderate solar wind driving with good coverage by the SuperDARN radars and three consecutive low-offset passes by the F13 satellite will be studied in detail. Further, a statistical study of the effects of merging DMSP F13 data into SuperDARN patterns at moderate solar wind driving will be performed. The reason events at moderate driving are chosen is because under optimal conditions and the appropriate processing of the data, both DMSP and SuperDARN should observe the same potential. It therefore makes sense to focus on these optimal conditions first before moving on to analyze saturation.

The event to be studied in detail occurs on January 1, 2001 between the hours of 12:00 and 16:00 UT. Figure 7.1 shows the OMNI solar wind data for the time period of interest. The IMF Bz becomes increasingly negative, but only slightly exceeds -6 nT. During this time period, there was good global coverage by the SuperDARN radars, and three passes over the northern polar cap by the DMSP F13 satellite: one from 12:12 to 12:36 UT, one from 13:53 to 14:17 UT, and one from 15:35 to 15:57 UT.

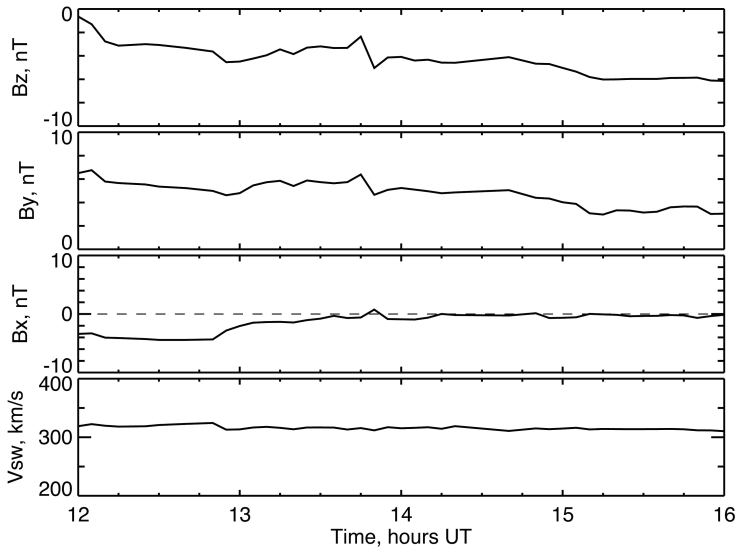

Figure 7.1: OMNI solar wind data propagated to the Earth's Bow Shock on January 20, 2001. The traces are, from the top: IMF Bz, By, Bx and the solar wind bulk speed, Vsw.

Initially, DMSP data is merged into the SuperDARN patterns with no pre-processing, aside from removing "poor" and "caution" quality flags. No error weighting on the satellite measurements, scaling based on altitude, or change in spatial and temporal resolution will be done. The SuperDARN vectors, however, will be processed with the usual spatial gridding and error weighting based on the standard deviation in velocity per grid cell. Figure 7.2 shows a time series of the polar cap potential for 12:00 - 16:00 UT on January 20, 2001, shown at 10 minute resolution. The solid line is the potential using only SuperDARN data. The dashed line uses SuperDARN data as well as DMSP data in each 10 minute interval where it is available. As can be seen, the polar cap potential using just SuperDARN steadily grows as the IMF in Figure 7.1 turns increasingly southward. This is to be expected. When DMSP F13 data is added into each 10 minute interval, spikes appear in the potential time series each time the satellite passes over the polar region.

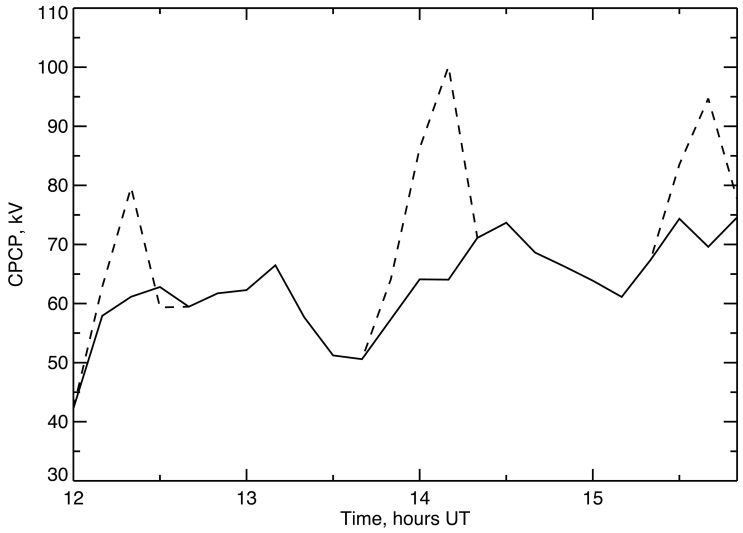

Figure 7.2: A time series of the polar cap potential for 12:00 - 16:00 UT on January 20, 2001. The solid line is the potential using only SuperDARN data. The dashed line is the potential using SuperDARN as well, but also including data from three consecutive passes by the DMSP F13 satellite. The potentials are calculated at 10 minute resolution in each case.

In order to demonstrate what is causing the large spikes in the potential time series, the actual convection maps can be examined. Figure 7.3 shows three calculated convection patterns for the third DMSP pass shown in Figure 7.2. The pattern on the left is a result of a spherical harmonic fit on data from SuperDARN radars alone and a statistical model based on the IMF conditions. The center pattern is the result of a spherical harmonic fit on DMSP data alone and statistical model vectors based on the IMF. The pattern on the right uses merged DMSP and SuperDARN data in addition to statistical model vectors. Again, no error weighting on satellite measurements, scaling based on altitude, or change in spatial and temporal resolution are used.

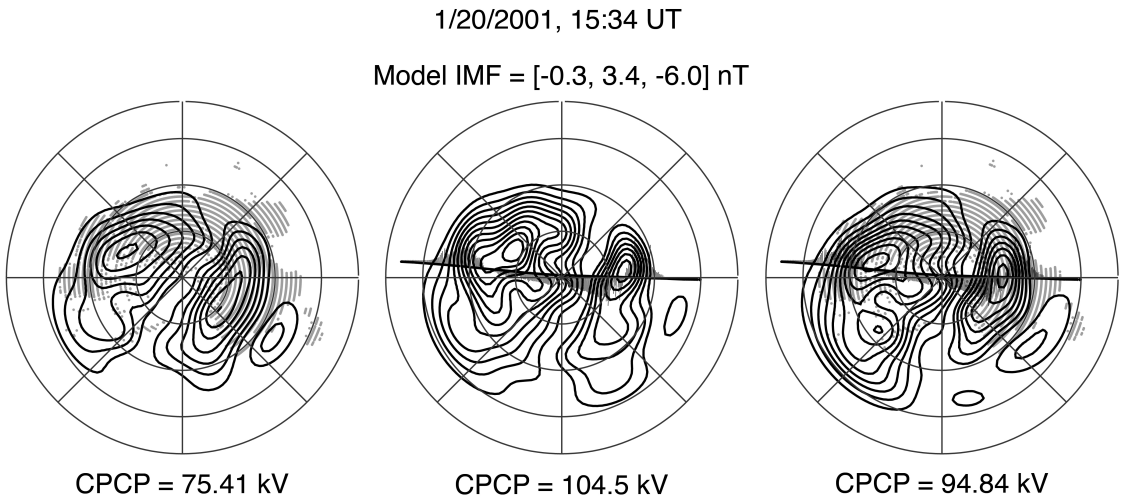

Figure 7.3: Maps of the polar cap potential for 1/20/2001 from 15:34 to 16:04 UT. Left is a pattern fitted to just SuperDARN data during the period. Center is a fitted pattern with just a single DMSP F13 pass over the period. Right is a fitted pattern containing both SuperDARN and DMSP measurements. Solid black lines are the electric potential contours, grey dots are the locations of the SuperDARN measurements, and the black dots are the location of the DMSP measurements. The DMSP data was not error weighted, filtered, or scaled in any way. Each pattern is given in AACGM MLT-MLAT format with magnetic local noon directed up the page. The lowest latitude shown is 50 degrees and contour spacing is 5.3 kV.

It can be seen from Figure 7.3 that the polar cap potential observed using fitted DMSP data is significantly larger than that seen by using fitted SuperDARN data. Merging DMSP data into the SuperDARN pattern also increases the strength of the potential pattern. It is also worth noting that when DMSP data is placed into the spherical harmonic fit without error weighting, the fitted potential pattern becomes unstable with unphysical vortices developing. This is because the spatial resolution of the dmsp measurements is too small for the spherical harmonics to capture. This is why SuperDARN data is spatially gridded before fitting.

In the case shown above, the polar cap potential drastically increases when DMSP velocities are merged into the spherical harmonic fit. This discrepancy has been noted

in previous studies of polar cap potential saturation, with SuperDARN observing the potential saturating at 100 kV, while DMSP observed a saturation potential of approximately 200 kV (*Shepherd et al.*, 2002; *Hairston et al.*, 2005). In order to combine the two data-sets properly, it is important to understand why this discrepancy in potential is seen.

One thing to consider is how the velocities seen by each data-set differ. *Drayton et al.* (2005) did comparisons between raw SuperDARN VLOS measurements and DMSP cross-track drift in regions where they overlapped. It was found that the SuperDARN measurements were smaller than DMSP measurements by a factor of 0.8 to 0.9. If it assumed that the geomagnetic field is dipolar, all measurements are at high latitude and the field lines are equipotential, then velocities measured at different altitudes would scale by a factor of $R^{3/2}$, with R being the distance from the center of the Earth. This implies that at typical measurement altitudes, SuperDARN velocity measurements should be approximately 88.8% smaller than those made by DMSP. Therefore, much of the discrepancy in velocity that has been observed in the past can be explained by difference in altitude of the measurements. When merging the two data-sets together, DMSP velocity vectors should be scaled for altitude.

The second reason for differing potential measurements has to do with the spatial resolution of the two data-sets. As has been explained before, before SuperDARN VLOS measurements are fitted to a convection pattern using spherical harmonics, the measurements are filtered over spatial "grid cells" in order to remove artifacts in the convection patterns associated with the variable area of radar range-beam cells. The filtering is also necessary to remove noise spikes in the radar data. Therefore, gridded SuperDARN measurements are filtered over a larger spatial volume than DMSP measurements. In order to merge the two data sets, DMSP measurements

should be subjected to the same pre-processing and averaged to SuperDARN gridded spatial resolution. An added benefit of averaging DMSP data down to SuperDARN grid resolution is that it allows DMSP data to be more easily folded into time series in which the time resolution may be shorter than the duration of a DMSP pass.

A final factor which has an impact on the calculated polar cap potential is error weighting of the velocity data. The coefficients of the spherical harmonic expansion which are calculated to obtain a potential pattern are obtained using least-squares fitting. When performed on SuperDARN data, typically each velocity measurement is weighted by the standard deviation in measured velocity over its respective grid cell. If one is to assume that DMSP and SuperDARN should be weighed equally in a fit, then some form of error analysis must also be applied for velocity data from the DMSP satellite. For each individual DMSP measurement, a four second standard deviation is supplied, which corresponds to approximately 29.6 km spatial resolution. The method which will be used in the present study is to simply average this over each 100 x 100 km "grid cell."

When DMSP data is scaled for altitude, averaged to SuperDARN grid resolution and weighted by standard deviation, it can be merged with SuperDARN data to produce a coherent global pattern. To demonstrate this point, the plots in Figures 7.2 and 7.3 are recalculated upon using the new method of merging DMSP satellite and SuperDARN radar data.

Figure 7.4 shows three calculated potential patterns for the same time period as Figure 7.3. This time, the DMSP data is scaled for altitude, averaged to SuperDARN grid resolution, and is weighed by standard deviation in the spherical harmonic fit. Left is a pattern fitted to SuperDARN data, center is a pattern fitted to DMSP data, and right is a pattern fitted to both data-sets. The measured polar cap potentials

are 75.41, 76.21 and 75.96 kV respectively. In comparing Figures 7.3 and 7.4, it can be seen that the pattern seen with just DMSP data is less distorted once appropriate error weighting and gridding of the data is applied. Further, the data from the satellite can now be merged with SuperDARN data without dominating areas with overlapping coverage.

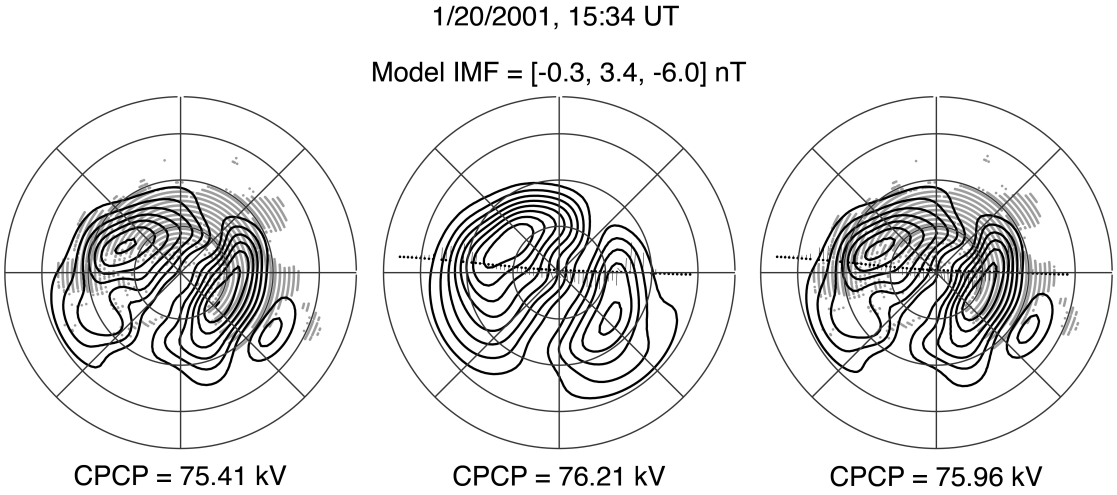

Figure 7.4: Maps of the polar cap potential for 1/20/2001 from 15:34 to 16:04 UT, which is the same time period as Figure 7.3. Left is a pattern fitted to just SuperDARN data during the period. Center is a fitted pattern with just a single DMSP F13 pass over the period. Right is a fitted pattern containing both SuperDARN and DMSP measurements. Solid black lines are the electric potential contours, grey dots are the locations of the SuperDARN measurements, and the black dots are the location of the DMSP measurements. Thin black lines extend from the black dots to denote the magnitude and direction of the cross-track plasma drift. Each pattern is given in AACGM MLT-MLAT format with magnetic local noon directed up the page. The lowest latitude shown is 50 degrees and contour spacing is 5.3 kV.

Figure 7.5 shows a time series of the polar cap potential for the same time period as Figure 7.2. The solid line represents the potential calculated using only SuperDARN data and the dashed line is the potential using both SuperDARN data and cross-track velocity data from DMSP F13 as the three satellite passes from the time interval occur. This time, the DMSP data is scaled for altitude, averaged to Su-

perDARN grid resolution, and is weighted by standard deviation in the spherical harmonic fit. The spikes seen in Figure 7.2 are gone, and only slight differences remain when DMSP data is included in the potential fit. These differences are acceptable as an uncertainty in the measurement.

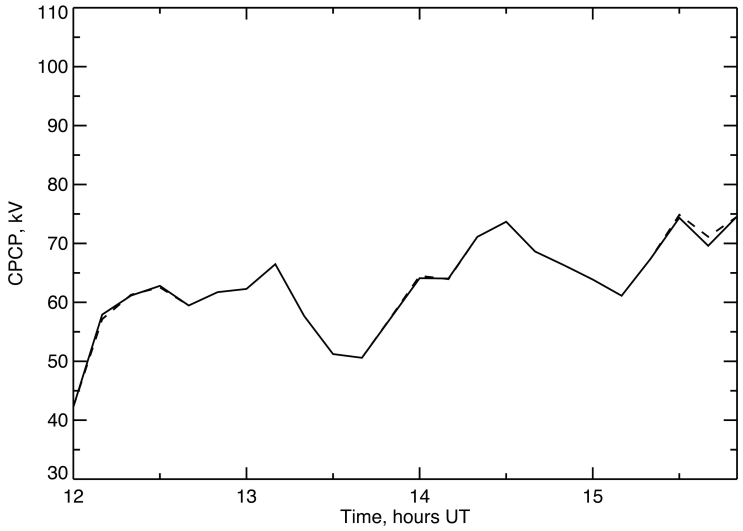

Figure 7.5: A time series of the polar cap potential for 12:00 - 16:00 UT on January 20, 2001. This is the same time period as Figure 7.2. The solid line is the potential using only SuperDARN data. The dashed line is the potential using SuperDARN as well, but also including data from three consecutive passes by the DMSP F13 satellite. The potentials are calculated at 10 minute resolution in each case.

In order to statistically demonstrate the effect of spatial averaging, altitude scaling, and error weighting on DMSP measurements before merging them with SuperDARN data, 31 low-offset F13 passes will be examined. The selection criteria for these passes were observation of both convection cells, and an average of 200 dayside SuperDARN measurements per 2-minute interval for the 30 minutes after the satellite pass over the polar cap begins. Having a significant amount of dayside SuperDARN measurements ensures that the low latitude boundary of the polar cap convection pattern will be resolved in the spherical harmonic fit. These passes are

listed in Appendix B.

Figure 7.6 shows the calculated polar cap potential using merged DMSP and SuperDARN data ($CPCP_M$) versus the calculated polar cap potential using SuperDARN data alone($CPCP_{SD}$). Points where no spatial filtering, error weighting or altitude scaling was performed on the DMSP data are represented by triangles. Points where the DMSP data was pre-processed are represented by black dots. The solid black line represents the ideal case where $CPCP_M = CPCP_{SD}$. This case is considered ideal because it assumes that there is adequate coverage by the SuperDARN radars alone to make an accurate potential measurement.

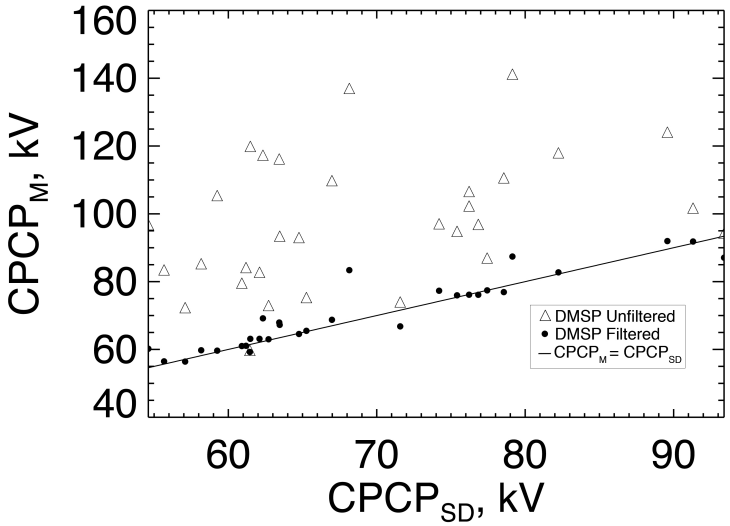

Figure 7.6: The calculated polar cap potential using merged DMSP and SuperDARN data for the 31 events selected $CPCP_M$ versus the calculated polar cap potential using only SuperDARN data $CPCP_{SD}$. Triangular points are potential patterns where DMSP was not spatially filtered, scaled for altitude, or error weighted. Black dots indicate potential patterns where DMSP data was pre-processed. The solid line represents $CPCP_M = CPCP_{SD}$.

It can be seen in Figure 7.6 that when pre-processing of DMSP velocity measurements as described above is performed, the polar cap potential measurement is closer to the solid line. This indicates that DMSP measurements are observing

roughly the same phenomena as SuperDARN measurements, and are not dominating the potential fit in locations where they overlap. Points where the merged potential measurement is still significantly larger than the SuperDARN potential measurement are due to gaps in coverage, as the selection criteria used number of measurements and not spatial distribution. When examining the 10 "best" events with an even distribution of SuperDARN measurements across the local dawn and dusk sectors, the potential using just DMSP differs from the potential using just SuperDARN by an average of approximately 7% of the SuperDARN potential. The potential using the merged data-set only differs from the SuperDARN potential by 1-2%. This demonstrates that the data-sets can be successfully merged under optimal conditions, so the analysis can be applied to less optimal conditions when the polar cap potential saturates.

To demonstrate the advantage of merging DMSP into SuperDARN patterns, one more example at stronger solar wind driving will prove useful. Figure 7.7 shows two potential patterns for September 23, 2001. Both patterns are given in the same format as those given in Figure 7.4. Both use SuperDARN measurements between 17:21 and 17:51 UT. The left pattern only contains SuperDARN data, while the right pattern includes a pass by the DMSP F13 satellite. The measured polar cap potential for each is 67.09 kV and 91.85 kV, respectively. The left pattern shows good coverage by SuperDARN over a majority of the dusk convection cell. Its weakness is lack of coverage at low latitudes, the center of the polar cap, and the dawn convection cell. In fact, a majority of the dawn cell is determined by statistical model vectors. The pattern on the right demonstrates the benefit of adding a DMSP pass to the pattern. The added coverage constrains the dawn cell more, and shows convection at lower latitudes as well as over the center of the polar cap. However, these modifications

have been achieved without altering the details in the vicinity of the SuperDARN measurements or introducing instabilities into the pattern. The result is a 24.76 kV increase in the measured potential. Using this method of calculating the polar cap potential will prove useful in investigating the polar cap potential saturation phenomenon.

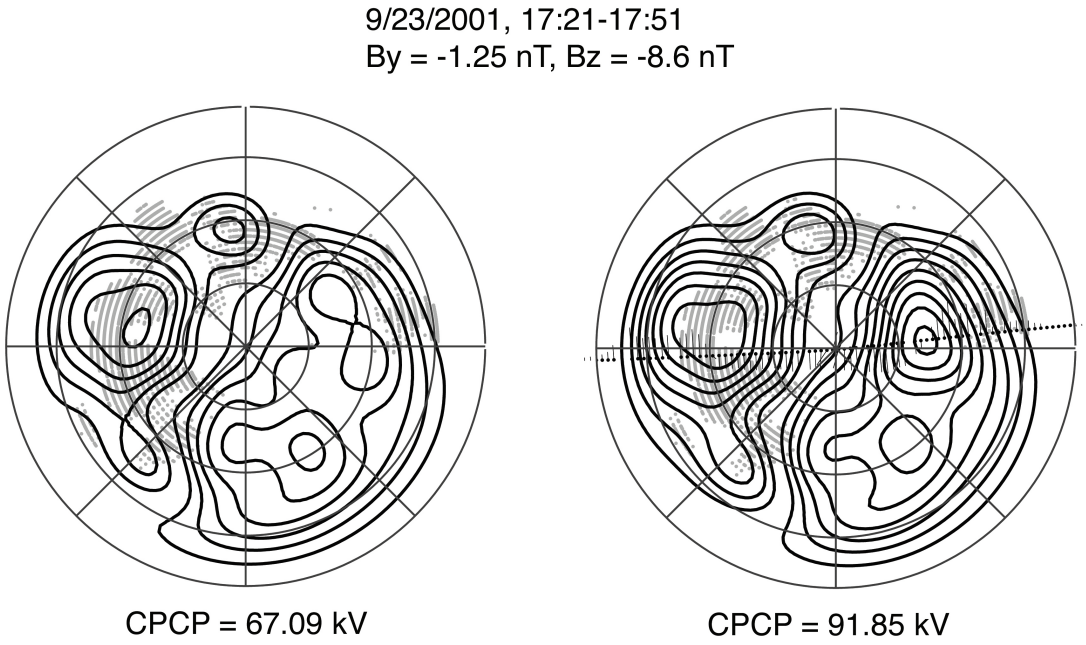

Figure 7.7: Maps of the polar cap potential for 9/23/2001 from 17:21 to 17:51 UT. Left is a pattern fitted to just SuperDARN data during the period. Right is a fitted pattern containing both SuperDARN and DMSP measurements. Solid black lines are the electric potential contours, grey dots are the locations of the SuperDARN measurements, and the black dots are the location of the DMSP measurements. Thin black lines extend from the black dots to denote the magnitude and direction of the cross-track plasma drift. Each pattern is given in AACGM MLT-MLAT format with magnetic local noon directed up the page. The lowest latitude shown is 50 degrees and contour spacing is 5.3 kV.

7.3 Testing the Models of Polar Cap Potential Saturation

7.3.1 Interplanetary and Geophysical Parameters Relevant to Saturation

Most hypotheses explaining saturation of the polar cap potential invoke the effects of upstream solar wind conditions on the polar cap potential's response to the interplanetary electric field. In order to calculate the parameters relevant to these upstream conditions, 1 minute data from the OMNI database between 1998 and 2007 was used for conditions directly upstream of the bow shock (*King and Papitashvili*, 2005). Parameters relevant to the present study include the interplanetary electric field coupling function, solar wind dynamic pressure, the Alfvènic Mach number, and the Alfvèn wing transmission coefficient.

For the interplanetary electric field coupling, the metric commonly known as the Kan-Lee function was used. This function is given by equation (7.1).

$$E_{KL} = V B_T \sin^2 \frac{\theta}{2} \tag{7.1}$$

Where V is the anti-sunward component of the solar wind velocity, $B_T = \sqrt{B_Z^2 + B_Y^2}$ is the IMF transverse to V, and $\theta = \cos^{-1} \frac{B_Z}{B_T}$ is the IMF clock angle in the (Y-Z) plane (*Kan and Lee*, 1979; *Sonnerup*, 1974). Several studies have used this parameter to correlate the interplanetary electric field with the polar cap potential (*Reiff et al.*, 1981; *Weimer*, 1995; *Shepherd et al.*, 2002).

The dynamic pressure of the solar wind is calculated using $P_{dyn} = \rho_{sw} V^2$, where ρ_{sw} is the mass density of the solar wind.

The solar wind can also be characterized by its speed relative to MHD modes ambient in the plasma. The most commonly referenced mode is the Alfvèn wave, which propagates parallel to the IMF. The Alfvènic Mach number is the ratio of the solar wind speed and the solar wind Alfvèn speed and is given by equation (7.2).

$$M_A = \frac{V}{V_A} = V(\frac{B^2}{\mu_0 \rho_{sw}})^{-1} \tag{7.2}$$

Where M_A is the Alfvènic Mach number and V_A is the Alfvèn speed of the solar

wind.

The Alfvèn Wing Transmission Coefficient

The final solar wind parameter of interest is the Alfvèn wing transmission coefficient. It is also related to the Alfvèn speed of the solar wind, but requires more detailed explanation. *Kivelson and Ridley* (2008) presented the hypothesis that the polar cap potential saturation phenomenon is, in actuality, a wave phenomenon. The concept is that as the IMF increases in magnitude, the Alfvèn speed of the solar wind also increases, reducing the Alfvènic Mach number. It has been suggested that in many events when the polar cap potential saturates, the Alfvènic Mach number even reduces to less than 1.

In order to understand what happens as a sub-Alfvènic plasma passes a conducting body, one can look to the moons of Jupiter. The Galileian satellites Io and Ganymede are embedded in plasma co-rotating with Jupiter within its magnetosphere (*Kopp and Ip*, 2002; *Ip and Kopp*, 2002). As a result, when the sub-Alfvènic plasma containing a frozen-in magnetic field encounters these obstacles, the magnetic field bends and Alfvèn waves are launched along magnetic field lines. The combination of a bent magnetic field and Alfvèn waves forms tubes of plasma above and below the satellite where the flow characteristics are significantly altered. These tubes are called "Alfvèn wings" (*Neubauer*, 1980; *Linker et al.*, 1998). It should be noted that in the original formulation of the Alfvèn wing problem, it was assumed that $M_A << 1$ (*Drell et al.*, 1965).

Ridley (2007) demonstrated that prominent Alfvèn Wings could develop when M_A dropped below 1 using MHD simulations. It was then proposed by *Kivelson and Ridley* (2008) that the interplanetary electric field was transmitted via Alfvèn waves

into the polar cap, generating the polar cap potential. In this formulation, Alfvèn wings act as a transmission line, with a conductivity given by equation (7.3).

$$\Sigma_A = (\mu_0 V_A)^{-1} \tag{7.3}$$

Where Σ_A is the Alfvèn wing conductivity. During nominal conditions, Σ_A is significantly larger than the ionospheric Pederson conductivity, Σ_P, and the relationship between the incident interplanetary electric field (IEF) and transmitted polar cap potential is approximately linear. When the IMF becomes increasingly strong, Σ_A is reduced, and part of the incident IEF is reflected by the polar cap. Using MHD wave reflection theory, *Kivelson and Ridley* (2008) showed the expression for the polar cap potential to be given by equation (7.4).

$$\Phi_{PC} = \frac{2E_{SW}^R D\Sigma_A}{\Sigma_P + \Sigma_A} \tag{7.4}$$

E_{SW}^R is the effective IEF which merges into the magnetosphere via reconnection and D is the reconnection line length. In this study, I define

$$Q_A = \Sigma_A(\Sigma_A + \Sigma_P)^{-1}, \tag{7.5}$$

which is half the Alfvèn wing transmission coefficient.

In order to calculate Q_A, the ionospheric Pederson conductivity is needed. In the present study, the empirical formula from *Robinson et al.* (1987) was used to approximate Σ_P from the monthly F10.7 flux and the solar zenith angle. This formula is given by equation (7.6).

$$\Sigma_P = 0.88(S_a \cos\chi)^{1/2} \tag{7.6}$$

S_a is the F10.7 flux and χ is the solar zenith angle. This method of calculating the ionospheric conductivity is appropriate, since it accounts for the seasonal trends

in polar cap illumination and F10.7 flux. Under strong driving, there may be an increase in auroral conductivity; however, this is difficult to precisely determine and therefore isn't used in the present study.

The Saturation Q Parameter

In order to examine conditions in the solar wind and see how they relate to polar cap potential saturation, it will be useful to determine a metric for how "saturated" an individual potential measurement is. For this purpose, I define a non-linearity factor, Q, given by equation (7.7).

$$Q = \frac{CPCP_{measured}}{CPCP_{linear}} \tag{7.7}$$

$CPCP_{measured}$ is the polar cap potential calculated using fitted potential data, and $CPCP_{linear}$ is the predicted polar cap potential using a linear fit on potential measurements from events with weak-to-moderate solar wind driving. A larger value of Q refers to a potential which is "less saturated", while a smaller value of Q refers to a potential which is "more saturated." Q greater than 1 implies that the potential is likely not "saturated."

Because I am using gridded ionospheric velocity data applied to a spherical harmonic fit, it would be most useful to define $CPCP_{linear}$ using a similar data-set. To obtain a linear fit, events where E_{KL} varied by no more than 10% for at least 50 minutes were selected. The first 20 minutes were truncated both to account for error in propagation of the solar wind data, as well as to allow time for the polar cap potential to develop. For the last 30 minutes, it was required that there were approximately 700 gridded SuperDARN measurements every 10 minutes. This ensures that there is adequate coverage by the radars to make a potential measurement during moderate driving, as in section 7.2. A spherical harmonic fit was applied to

velocity data for each period in order to measure the potential.

Figure 7.8 shows CPCP versus E_{KL} for the selection criteria described above. A linear fit was performed for E_{KL} between 0 and 10 kV/Re. The y-intercept was held fixed at 20 kV, to account for previous measurements of the viscous potential (*Wilder et al.*, 2009; *Papitashvili et al.*, 1981). This has also been observed using coordinated observations between SuperDARN, DMSP and the Sondrestrom incoherent scatter radar during the week of May 12-17, 2007 when the IMF was near zero. The resulting fit is given by equation (7.8).

$$CPCP_{linear}(kV) = 20 + 4.433E_{KL}(kV/Re) \tag{7.8}$$

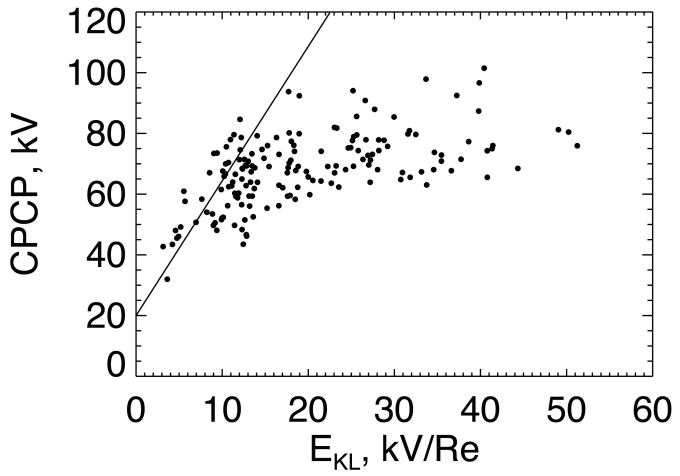

Figure 7.8: Scatter plot of polar cap potential versus the Kan-Lee coupling function. The line is a linear fit for E_{KL} from 0 to 20 kV/Re.

It can be seen from Figure 7.8 that for E_{KL} greater than 20 kV/Re, the linear fit always over-predicts the polar cap potential. This is in agreement with previous observations of when polar cap potential saturation begins sets in (*Shepherd et al.*, 2002; *Hairston et al.*, 2005). It is worth noting that when (*Reiff et al.*, 1981) performed a linear fit to E_{KL}, they had a y intercept of 39 kV and a significantly smaller slope.

It should be noted, however, that they included events at extreme driving where we now know saturation occurs in their fit.

Event Selection Criteria

In the present study, two different selection criteria are used depending on the solar wind driving. For weak-to-moderate solar wind driving ($E_{KL} \approx 0 - 25kV/Re$), as long as there is good coverage by the SuperDARN radars, then accurate potential measurements can be made. For this regime of driving, it was simply required that E_{KL} varied by no more than 10% over 50 minutes. Further, for the last 30 minutes of the 50 minute period, it was required that at least 700 measurements from SuperDARN were available per 10 minute interval, with at least 200 of those being on the dayside. This ensures that the radars capture the spatial extent of the potential pattern. The polar cap potential was then calculated for the last 30 minutes of the event in order to account for error in the propagation of the solar wind data.

For stronger solar wind driving, it is likely that the polar cap potential pattern will expand beyond the field of view of the SuperDARN radars. Therefore, data from DMSP should also be used to resolve the potential pattern at lower latitudes. This changes the selection criteria, as care must be taken in merging the data-sets. For events with $E_{KL} > 25kV/Re$, selection was based on the simultaneous availability of DMSP and SuperDARN data. In particular, only events with DMSP passes which cross through both convection cells and potential offsets less than 25% are used. This ensures stability of the potential pattern over the pass. Further, in the 30 minutes surrounding the DMSP pass, at least 500 SuperDARN measurements per 10 minutes are available. No restriction is placed on the availability of dayside

SuperDARN measurements, because the DMSP satellites are now the instrument providing coverage of the equator-ward extent of the potential pattern. The threshold of $E_{KL} > 25kV/Re$ was chosen because it corresponds with the "saturation" regimes seen in previous studies of polar cap potential saturation (*Reiff et al.*, 1981; *Hairston et al.*, 2005; *Shepherd et al.*, 2002). These DMSP passes and their corresponding interplanetary parameters are listed in Appendix B.

Using the above criteria, a total of 158 events were found, with 55 existing in the "saturation" regime of driving. For each event, the polar cap potential was calculated, along with the mean E_{KL}, M_A, P_{SW} and Q_A in order to test the hypotheses related to polar cap potential saturation.

7.3.2 Results

Using the event selection criteria described in section 7.3.1 and the potential fitting described in section 7.2, the polar cap potential was calculated for the 158 thirty-minute periods being studied. For each potential measurement, the non-linearity factor Q, given by equations (7.7) and (7.8), was calculated as a measure of the extent of polar cap potential saturation.

Figure 7.9a shows a scatter plot of CPCP vs. E_{KL} for the 158 events used in the study. While there is a large amount of variation in CPCP, it seems to be insensitive to changes in E_{KL} beyond 25 kV/Re, which demonstrates that the events chosen exhibit the saturation trend observed in previous studies. Figure 7.9b and 7.9c show how the saturation parameter, Q, varies with respect to (b) E_{KL} and (c) CPCP, respectively. It can be seen that at larger values of E_{KL}, Q becomes smaller, which means the polar cap is increasingly over-predicted by a linear formula. This makes sense, given the nature of the saturation phenomenon. The same applies

for the CPCP, which is larger at larger values of Q, or when the potential is "less saturated." These plots are for demonstrative purposes, and are simply used to show that Q captures the saturation phenomenon.

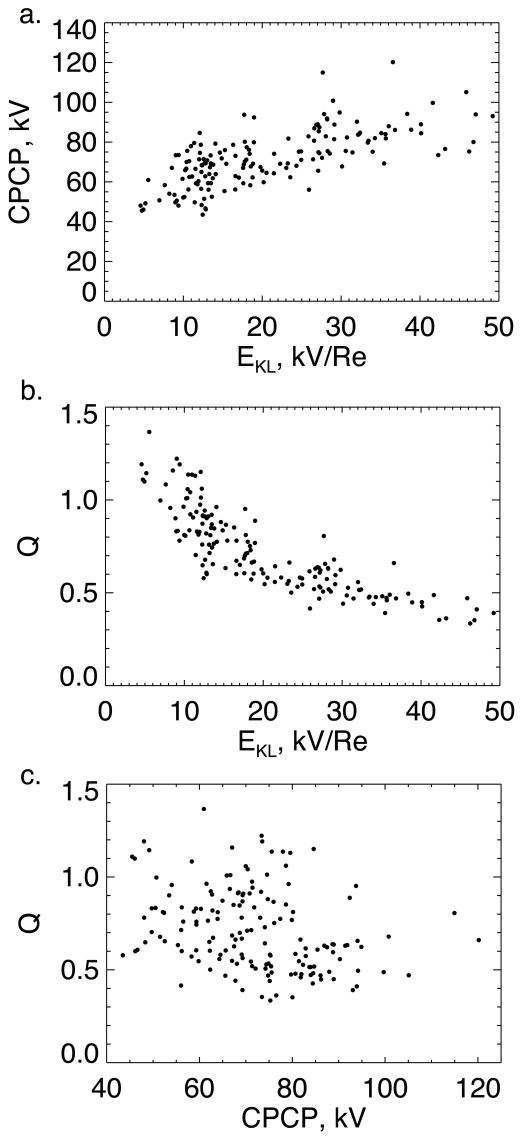

Figure 7.9: Scatter plots of (a) CPCP vs. E_{KL}, (b) Q vs. E_{KL} and (c) Q vs. CPCP.

In order to examine the various models of polar cap potential saturation, one can investigate how the value of Q varies with respect to the various interplanetary parameters central to the models. Figure 7.10 shows scatter plots of Q versus (a)

solar wind dynamic pressure, (b) solar wind Alfvènic Mach number, and (c) Alfvèn wing transmission coefficient. As can be seen, there is a large amount of scatter, yet visible trends are apparent for all three parameters. A non-linear correlation analysis will prove useful to investigate the statistical significance of the trends in the extent of polar cap potential saturation.

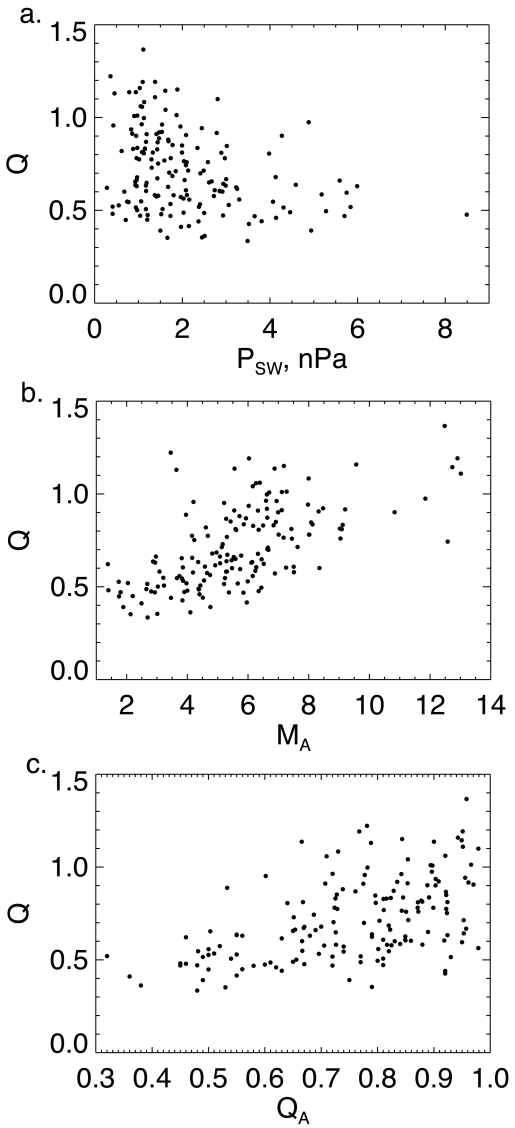

Figure 7.10: Scatter plots of the saturation parameter, Q, vs. (a) solar wind dynamic pressure, P_{SW}, (b) solar wind Alfvènic Mach number, M_A, and (c) Alfvèn wing transmission coefficient, Q_A.

One of the main challenges in performing a correlation analysis for the polar cap potential saturation phenomenon is that it is inherently non-linear. Further, it is not necessarily reasonable to assume that all parameters being investigated have a Gaussian distribution. Unfortunately, these two assumptions are central to using the typical Pearson product-moment correlation coefficient. Therefore, another method of analysis must be performed in order to investigate the polar cap potential saturation phenomenon.

For the present study, the Kendall rank correlation (τ) (*Kendall*, 1938) and the Spearman rank correlation (ρ) (*Spearman*, 1904) are used. These correlation coefficients each show the degree to which the two variables being correlated vary in a monotonic manner. In other words, it tests for whether one variable increases or decreases as the other increases. These coefficients will quantify a linear, square-root, exponential or other monotonic trend. Both of these correlations are tested at the 5% significance or 95% confidence level. The Spearman correlation coefficient can be thought of as a Pearson correlation coefficient, but between ranked variables. The Kendall correlation coefficient requires further explanation.

The Kendall correlation coefficient looks at joint observations of two variables or parameters, X and Y. If there is a pair of two joint observations, (X_i, Y_i) and (X_j, Y_j), then one can determine if the pair is "concordant" or "discordant." A pair is concordant if the following condition is met: $(X_i > X_j)$ and $(Y_i > Y_j)$. Conversely, the pair is considered discordant if $(X_i > X_j)$ and $(Y_i < Y_j)$. The Kendall correlation coefficient is proportional to the number of concordant pairs minus the number of discordant pairs (*Kendall*, 1938). Therefore, a data-set with more concordant pairs than discordant will exhibit positive correlation, while a data-set with more discordant pairs than concordant pairs will exhibit negative correlation.

A data-set with an equal number of concordant and discordant pairs will exhibit no correlation.

Table 7.1 shows the values of ρ and τ between the saturation parameter, Q, and various interplanetary and geospace parameters. The mean and standard deviation of each parameter in its respective units are also included. All correlations are significant at the 5% level. The strongest correlation is with E_{KL}, which is anti-correlated. This is to be expected, since as E_{KL} gets larger, the potential will become more "saturated."

Table 7.1: Correlation between Q and various interplanetary and geospace parameters for the selected events.

Parameter	τ	ρ	mean	st. dev.
E_{KL} (kV/Re)	-0.705	-0.885	20.87	10.45
P_{SW} (nPa)	-0.233	-0.336	2.09	1.36
M_A	0.452	0.633	5.69	2.30
Q_A	0.362	0.510	0.751	0.153

The weakest correlation is with the dynamic pressure, which is negatively correlated. This will be expanded upon later, but a large contributing factor to the negative correlation could be the fact that under weak IEF driving, there tends to be significantly lower dynamic pressure because the velocity is lower. There could be competition between this fact and possible positive correlation with potential under stronger driving which reduces the correlation coefficient.

The second strongest correlation is with the solar wind Alfvènic Mach Number. This can have several implications, especially with regards to the Alfvèn wing model. As can be seen from Table 1 and Figure 7.10c, Q_A and Q also exhibits positive correlation. While the correlations given in Table 7.1 seem to imply that the Alfvèn

wing model is a plausible model for polar cap potential saturation, the scatter plot in Figure 7.10b presents a contradiction. In a majority of cases where Q is significantly smaller than 1, the Alfvènic Mach number has a large amount of variation between the values of 2 and 8. A majority of this range is theoretically too super-Alfvènic for Alfvèn wings to form. In the original theory of Alfvèn wings, M_A was assumed much smaller than 1 (*Drell et al.*, 1965; *Neubauer*, 1980). It is therefore important that the Alfvèn wing model provide a physical picture by which an appropriate conducting channel can form to cause the reflection represented by the Alfvèn wing transmission coefficient without actual Alfvèn wings forming.

Finally, it is useful to investigate how Q correlates with various interplanetary parameters for $E_{KL} > 25kV/Re$ in order to see whether events from the "linear" regime are biasing the correlations given in Table 7.1. Table 7.2 shows the correlation coefficient between Q and various interplanetary parameters, as well as each parameter's mean and standard deviation for $E_{KL} > 25kV/Re$. Correlations given in bold pass a significance test at the 5% level. The most stark difference from Table 7.2 is the correlations for dynamic pressure, which are weakly positive. This could from the idea that under an increase in dynamic pressure, the region 1 currents will adjust so that the resulting $\mathbf{J} \times \mathbf{B}$ force balances the solar wind dynamic pressure. Since the correlation is not statistically significant, however, it is unlikely that such a process has a significant impact on the saturation of the polar cap potential. It should be noted that these measurements are from average potential patterns over a 30 minute period, and therefore do not say anything about the time dependent response of the polar cap potential to pressure pulses in the solar wind.

Table 7.2: Correlation between Q and various interplanetary and geospace parameters for $E_{KL} > 25kV/Re$.

Parameter	τ	ρ	mean	st. dev.
E_{KL}, kV/Re	**-0.494**	**-0.670**	26.01	14.81
P_{SW}, nPa	0.073	0.126	2.85	1.786
M_A	**0.244**	**0.361**	4.10	1.50
Q_A	0.141	0.200	0.632	0.155

Further, from Table 7.2, it appears that the extent of saturation no longer correlates with the Alfvèn wing transmission coefficient in a statistically significant manner. It is possible that this could be impacted by our method of calculating the ionospheric height-integrated pederson conductivity, as under strong solar wind driving, auroral conductivity can have a larger impact on ionospheric convection. All other parameters exhibit statistically significant correlation, albeit much weaker than in Table 7.1. These significantly smaller correlation coefficients demonstrate that as the solar wind driving becomes strong enough, the response of the polar cap potential becomes increasingly insensitive to all parameters in the solar wind.

7.4 Summary and Discussion

This study is intended to present a statistical view of the non-linear coupling between the solar wind and the Earth's magnetosphere-ionosphere system. First, it was demonstrated that DMSP and SuperDARN data can be consistently merged to provide a global polar cap potential pattern. This resolves some of the controversy over what exactly the saturation potential is (*Shepherd et al.*, 2002; *Hairston et al.*, 2005; *Sundberg et al.*, 2009, Chapter 3). Polar cap potential values were calculated for 158 events and the extent of polar cap potential saturation was compared to various

parameters in the solar wind. No significant relation with dynamic pressure was found, but significant correlation with Alfvènic Mach number and related parameters was noted.

It was also shown that while the Alfvèn wing transmission coefficient correlated in a statistically significant manner with the non-linearity of the polar cap potential, there was a discrepancy in the fact that for most events (even under strong driving), the Alfvènic Mach number was still larger than traditional Alfvèn wing theory requires. Recently, another mechanism for polar cap potential saturation has been proposed which accounts for saturation occurring at less-than-nominal M_A while allowing for the existence of a bow shock. In this model, MHD jump theory is invoked to suggest that at strong driving and lower Alfvènic Mach number, there is a larger magnetic shear across the bow shock. This increases the strength of the magnetic field and reduces the plasma beta in the magnetosheath. It also produces an electric current across the bow shock to account for the magnetic shear, which closes partially in the Chapman-Ferraro currents at the magnetopause, as well as in the ionosphere via Region 1 field aligned currents. At reduced magnetosheath plasma beta and stronger bow shock current, there will therefore be a stronger $\mathbf{J} \times \mathbf{B}$ force which diverts magnetosheath plasma around the flanks of the magnetosphere, reducing the reconnection potential at the magnetopause (*Lopez et al.*, 2010). This reduction in magnetopause reconnection potential results in the saturation of the polar cap potential.

Further, it was found that the extent of polar cap potential saturation under strong driving ($E_{KL} > 25kV/Re$) showed no correlation with solar wind dynamic pressure. This implies that in the steady state, the region 1 currents do not need to re-adjust themselves to stand off the solar wind dynamic pressure, which is a

common feature of the Siscoe-Hill model. Therefore, it appears that either the Alfvèn wing (*Ridley*, 2007; *Kivelson and Ridley*, 2008) or the sheath control (*Lopez et al.*, 2010) mechanism is appropriate. Determining which mechanism is more accurate will depend upon how much measured parameters in the magnetosheath effect the polar cap potential in real time. Further research using satellite measurements during the next solar maximum will prove especially useful in accomplishing this goal.

CHAPTER VIII

CONCLUSION

The non-linear response of the ionospheric polar potential and convection pattern to increasingly strong interplanetary electric field has been discussed and debated since the mid-1970s (*Hill et al.*, 1976). While earlier studies did demonstrate that linear models over-predicted the polar cap potential once the IEF reached a certain magnitude, it was not until the past decade that there was enough consistent global coverage to empirically demonstrate that the polar cap potential "saturation" phenomenon occurred (*Reiff et al.*, 1981; *Shepherd et al.*, 2002; *Hairston et al.*, 2005). The question at present involves what causes this non-linear response, and whether the ionospheric convection driven by reconnection under other IMF orientations also exhibits non-linear behavior.

8.1 Summary of Results

This thesis presents a statistical and observational framework by which the remaining questions involving the non-linear response of the polar cap potential can be answered. First, I identified events where the IMF was northward for greater than 40 minutes, and binned the events by the IEF coupling function. Then, using superposed velocity measurements from SuperDARN, I calculated average convection

patterns from which I could calculate the reverse convection potential. The result was that as the IEF coupling function increased above 18 kV/Re, the reverse convection potential tapered off at approximately 20 kV. This demonstrated that while the lobe reconnection that occurs under northward IMF generates a more localized convection pattern, the associated potential in the polar cap saturates in the same manner as the overall polar cap potential under southward IMF. *Mitchell et al.* (2010) found that the polar cap potential also saturates when the IMF has an east-west orientation. This implies that non-linear "saturation" effects are inherent in the mechanism which couples the interplanetary electric field into the polar ionosphere, regardless of IMF orientation. Since the magnetic merging under northward, eastward, and westward IMF tends to occur on the night-side of the magnetosphere near the cusp, hypotheses such as the Siscoe-Hill model which rely on dayside reconnection under southward IMF may be inadequate.

Second, I expanded on the result that the reverse convection potential saturates by performing a variety of statistical studies. I demonstrated that when the size of the reverse convection cells is taken into account, the polar cap electric field at which they saturate is comparable to what is seen under southward IMF and polar cap potential saturation. This suggests that the electric field in the polar cap might be a better metric of coupling between the solar wind and the magnetosphere/ionosphere system than the potential. I also showed that the saturation reverse convection potential is significantly larger in summer months (16 kV) than in winter months (12 kV). This is the opposite of what one would expect given Ohm's law and equally effective lobe reconnection in each hemisphere. I then showed that the reverse convection potential still saturates at nominal Alfvènic Mach number (> 5), which demonstrates that Alfvèn wings may not be the fundamental mechanism by which the reverse

convection potential saturates. Finally, I showed that there appears to be an increase in reverse convection saturation potential with an increase in solar wind plasma β. This implies that either the sheath-control mechanism or a northward IMF analogue to the Siscoe-Hill model might be at work.

Third, I looked at the response of SuperDARN line-of-sight velocities (VLOS) in the polar cap to increasing IEF under both northward and southward IMF during winter, summer and equinox. For southward IMF, the VLOS measurements in the throat of the convection pattern saturated at a higher speed in the winter than in the summer, which is in agreement with the idea of reconnection as a current generator. For northward IMF, the sunward VLOS measurements saturated at a higher speed in the summer than in the winter, which is the opposite of the southward IMF case. For both orientations, the VLOS measurements under saturation corresponded to a saturation average electric field between 18 and 40 mV/m depending on season. This was found to be in agreement with what has been seen by DMSP satellites by *Hairston et al.* (2005) and *Sundberg et al.* (2009) for northward and southward IMF. While there has been debate over whether DMSP or SuperDARN sees the correct saturation potential, they both see roughly the same saturation average electric field across the polar cap.

Fourth, I investigated the seasonal asymmetry between the saturation reverse convection electric field under northward IMF using inter-hemispheric observations for a northern-winter case. In the sunward flow channel of the NBZ cells, the velocity was approximately 1000 m/s in the summer, and around 300 m/s in the winter. Further, the reverse convection cells were centered on open field lines in the summer hemisphere, but the morning cell in the winter hemisphere circulated on closed field lines. This suggests two things. First, that lobe field lines from the summer

hemisphere were draping over the dayside magnetosphere and merging with lobe field lines in the winter hemisphere. Second, it demonstrates that the IMF B_Y component skewed the over-draped field lines towards the morning side of the winter hemisphere, leaving the afternoon side open to direct merging with the IMF.

Finally, I took a statistical look at the saturation phenomenon when the IMF is southward. In particular, the investigation considered how the non-linearity of the polar cap potential response correlated with various interplanetary parameters. A major obstacle was determining a reliable way to measure the polar cap potential during storm time. This was done by merging DMSP driftmeter and SuperDARN line of sight data into a spherical harmonic fit by filtering the datasets to the same resolution, scaling by altitude, and weighing the velocity measurements by their spatial standard deviation. When this was done, it was found that the non-linearity of the polar cap potential correlated best with the Alfvènic Mach number, and little significant correlation with solar wind dynamic pressure. It was also found that under saturation, the polar cap potential was largely insensitive to all relevant interplanetary parameters.

In the past, polar cap potential saturation was largely thought to be a phenomenon related to southward oriented IMF and the Dungey reconnection model. This is at the core of the original Siscoe-Hill model (*Hill et al.*, 1976; *Siscoe et al.*, 2002a). The work presented in this thesis assists in demonstrating that saturation is a phenomenon inherent in the coupling of electric fields and currents into the magnetosphere-ionosphere system via the solar wind. In addition to the saturation of the reverse convection potential under northward IMF, *Mitchell et al.* (2010) observed the saturation of polar cap potential in response to strong eastward and westward IMF (the B_Y component). This leads one to the conclusion that the elec-

tric field and potential saturation observed in the ionosphere can be the result of two things: an inherent quality of magnetic reconnection itself, or an inherent quality in which field-aligned currents couple the solar wind electric field into the ionosphere.

The observed correlation between the extent of saturation and solar wind Alfvènic Mach number in chapter 7, but lack of correlation with solar wind dynamic pressure implies that the nature of the bow shock and magnetosheath may play a role in the saturation phenomenon. This also casts doubt on the pressure-balance aspect of the Siscoe-Hill model. Since saturation occurs even at nominal Alfvènic Mach number (observed in Chapters 4 and 7 for both northward and southward IMF respectively), it seems to imply that the formation of Alfvèn wings is unlikely to be the fundamental mechanism by which the electric fields in the polar ionosphere saturate. This leaves the Sheath-Control mechanism proposed by *Lopez et al.* (2010) to be tested.

Further, the seasonal asymmetry observed in the reverse convection electric field for Northward IMF demonstrates that magnetic field line topology in the magnetosphere also plays an important role in the coupling between the IMF and the geomagnetic field. In particular, it appears that direct merging with the IMF in the summer hemisphere is more effective than the "internal" reconnection observed in the winter hemisphere. Figuring out what the effect of magnetic field topology on solar wind-magnetosphere-ionosphere coupling is for other IMF orientations will be crucial for understanding how currents and electric fields feed into the ionosphere.

8.2 Future Work

Although the work presented in this thesis provides significant advances in our understanding of the polar cap potential saturation phenomenon, several questions still remain unanswered. Central to understanding the coupling between the solar

wind, magnetosphere and ionosphere is understanding the drivers of magnetospheric field-aligned currents (FACs). These FACs communicate strong electric fields into the polar ionosphere, which can effect upper atmospheric dynamics. Much of the future work on the polar cap potential saturation phenomenon should relate to how magnetospheric current systems are driven, and how they are effected by both internal and external factors.

Periods which have been traditionally referred to as "storm-time" coincided with a strongly southward IMF. When the IMF is oriented in a northward, eastward, or westward direction, FACs associated with the dayside cusp of the magnetosphere can form, as explained in Chapter 2. These dayside currents have been shown to be associated with anomalous density enhancements and strong localized Poynting flux in the thermosphere and ionosphere at times where traditional metrics of geomagnetic activity indicated a "quiet" magnetosphere (*Lühr et al.*, 2004; *Crowley et al.*, 2010).

The research in this thesis goes to demonstrate that the localized ionospheric convection which relates to these dayside currents has much in common with the larger scale ionospheric convection associated with southward IMF. In particular, both observe a saturation effect (see Chapters 3 through 5). Further, by demonstrating that sunward flow associated with reciprocal cells was weaker than sunward flow associated with merging cells, Chapter 7 suggested that magnetic field line topology might have an appreciable impact on the formation of dayside field aligned currents. In the case of both northward and southward IMF, there is a different merging site in each hemisphere.

To understand what drives dayside field aligned currents, and what impacts their magnitude, more case studies such as the one in Chapter 7 need to be done for a variety of IMF orientations and dipole tilts. One thing that should immediately be

apparent is that coverage of the ionosphere by one particular instrument is often not enough to completely resolve ionospheric electric fields. In addition to SuperDARN, other instruments and data-sets can be used.

One additional dataset which has not been used in present studies are the polar incoherent scatter radars (ISRs). An advantage to incoherent scatter radars is that they can measure the density, velocity, temperature and other plasma parameters using collective Thompson scattering off of individual electrons (*Evans*, 1972). These measurements can therefore be made even in the absence of field-aligned irregularities that SuperDARN detects, and therefore can provide additional coverage. In addition to RISR, there are several other incoherent scatter radars.

Traditional ISRs measure ionospheric velocity components by dwelling the radar in two different azimuthal directions until there is significant signal to attain a LOS velocity at similar range gates along the beam. In order to resolve two dimensional velocity vectors from these measurements, the ionospheric convection pattern must be assumed to be uniform and unchanging over the dwell times. Recently, the Advanced Modular Incoherent Scatter (AMISR) project has developed phased-array radars which can electronically stear the beam, allowing for drastically shorter dwell times and therefore, higher resolution velocity measurements.

The AMISR of interest for studying the saturation problem is the new Resolute Bay incoherent scatter radar (RISR) which has a field of view near the geomagnetic pole. RISR consists of north and south pointing faces. Each face consists of 128 panels that provide 4096 crossed dipole elements. The phased array design permits electronic steering of the radar beam by $\pm 25^o$ in azimuthal and vertical directions. Figure 8.1 shows an artists conception of RISR with two faces.

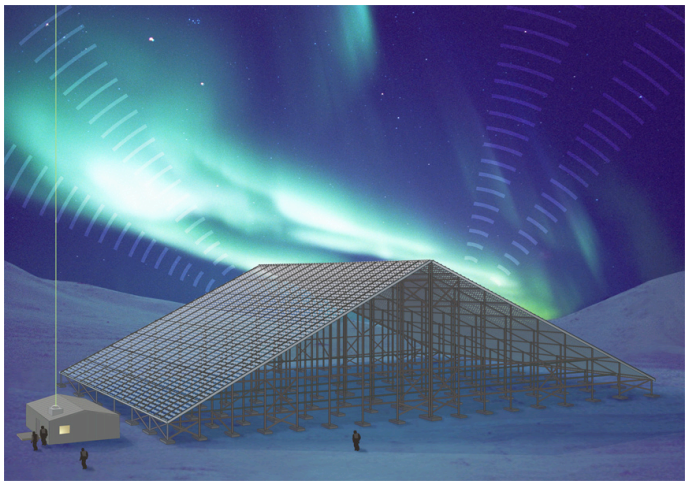

Figure 8.1: Artist's sketch of RISR with two radar faces, one pointed north and the other directed south.

Figure 8.2 shows the orientations of the RISR radars superposed on an ionospheric convection pattern and theta aurora for reference. Throughout the day, the radars will rotate around the pattern. We also show the fields of view of the pair of EISCAT radars, the Sondrestrom radar, the pair of faces to be deployed at Resolute, and the Poker Flat radar in Alaska. The oval patterns are for radar dishes that scan in azimuth and the star-like patterns come from the phased array radars. The size of the star patterns depend on the elevation angle and is a projection of the F-region field of view. The north-south configuration of the resolute radars allows for extended measurements across the polar cap, and being in a region that in the past had poor coverage, can massively help resolve convection patterns for both northward and southward IMF by placing considerable constraint on the electric potential fits when combined with SuperDARN.

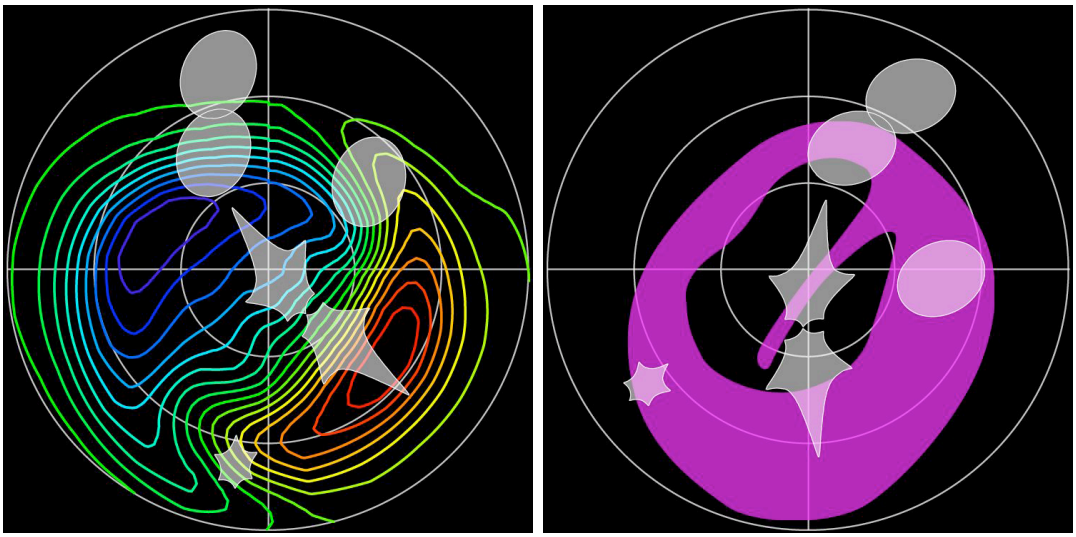

Figure 8.2: Fields of view for RISR along with other incoherent scatter radars. The star shaped patterns show AMISR fields of view at Resolute and Poker Flat. The oval regions show fields of view for the azimuthal scanning radars at Eiscat Svalbard and Tromso radars, and the sondrestron radar. A typical $B_Z < 0, B_y > 0$ potential pattern and theta auroral are shown for reference.

From Figure 8.2, it is apparent that when the RISR fields of view are on the dayside, they provide an excellent opportunity to measure the convection related to high latitude field aligned currents. One could, for example, run dayside experiments which coincide with satellite passes that measure energetic particle precipitation, in order to see how ionospheric convection and magnetic field line topology relate.

It will also be important to understand the drivers which determine the strength of field FACs, as well as the saturation of the polar cap electric field. While the evidence provided in this thesis contradicts the Siscoe-Hill and Alfvèn wing models, one magnetospheric model which explains the polar cap potential saturation model has not been falsified. This model is the sheath-control mechanism proposed by *Lopez et al.* (2010). In this model, strong magnetosheath magnetic fields, in addition to region 1 FACs which close with the bow shock surface current, divert the flow of magnetosheath plasma away from the reconnection site and around the flanks

of the magnetosphere. A similar process can occur under northward IMF, as the bow shock surface current would shift directions, and therefore have to close through currents with NBZ polarity. The resulting $\mathbf{J} \times \mathbf{B}$ force would also divert plasma around the flanks of the magnetosphere. When the IMF is eastward or westward, the bowshock current would have to close in the ionosphere via a unipolar DPY current which couples into each hemisphere. There are therefore two ways in which the sheath-control model of saturation may be tested.

First, given that the diversion of plasma flow around the flanks of the magnetosphere relates to the strength of the magnetic field in the magnetosheath relative to the thermal and dynamic pressure, the plasma β in the sheath will provide a useful metric by which to test the sheath-control hypothesis. During the upcoming solar maximum, experiments where RISR is on the dayside can measure convection, and see how the convection speed is effected by the magnetosheath plasma beta observed by satellites such as the Cluster mission. SuperDARN data may also be used to perform this analysis, particularly time series of ionospheric "true" velocity, as in Chapter 6.

Second, one could investigate the DPY currents in both hemispheres to see if there is evidence of a unipolar DPY current due to closure with the bow shock currents. In this case, use of magnetometer data in both hemispheres will be useful, including data from the ongoing PENGUIn project (*Musko et al.*, 2009). A challenge to investigating the sheath-control mechanism from this perspective; however, is that it will be difficult to subtract out the effect of viscous interactions.

Performing these analyses will be useful both in attempting to explain the saturation phenomenon, as well as investigating how strong dayside FACs form under northward, eastward and westward IMF. In essence, by finding the mechanism by

which saturation occurs, one can understand the over-all coupling between the solar wind, magnetosphere and ionosphere. Once these mechanisms are understood, we can forecast geomagnetic disturbances more accurately, which benefits society as a whole.

APPENDICES

APPENDIX A

Average Potential Patterns Used in Chapter 4

A.1 Average Potential Patterns Binned by Alfvènic Mach Number

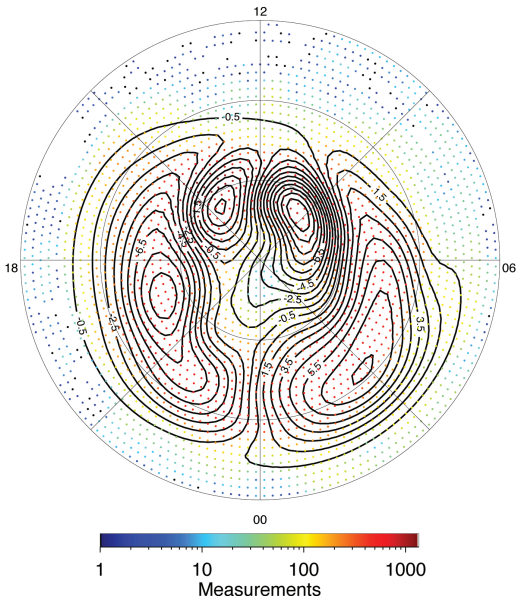

Figure A.1: Potential pattern for the bin with E_{RC} between 18 and 60 kV/Re and M_A between 0 and 3.

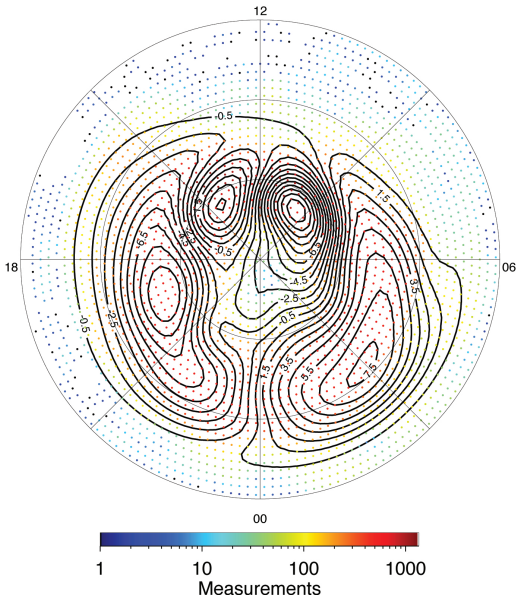

Figure A.2: Potential pattern for the bin with E_{RC} between 18 and 60 kV/Re and M_A between 1 and 3.

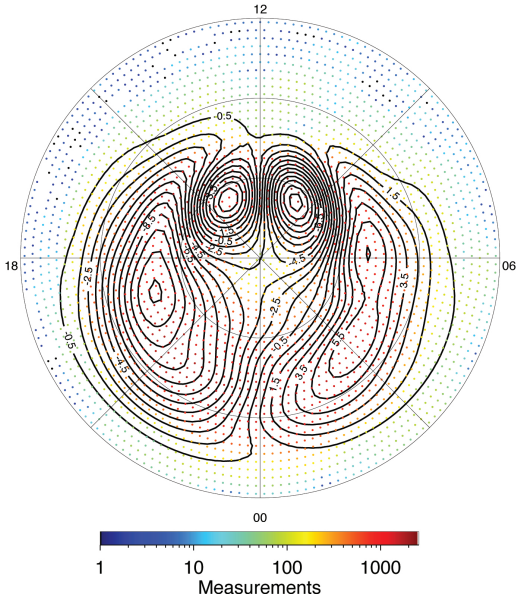

Figure A.3: Potential pattern for the bin with E_{RC} between 18 and 60 kV/Re and M_A between 2 and 4.

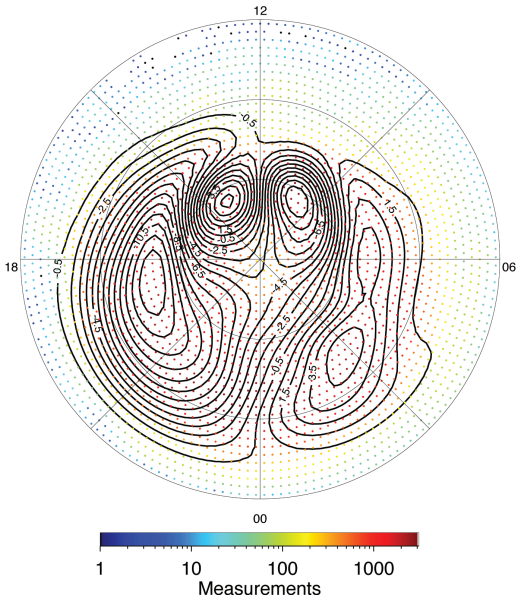

Figure A.4: Potential pattern for the bin with E_{RC} between 18 and 60 kV/Re and M_A between 3 and 5.

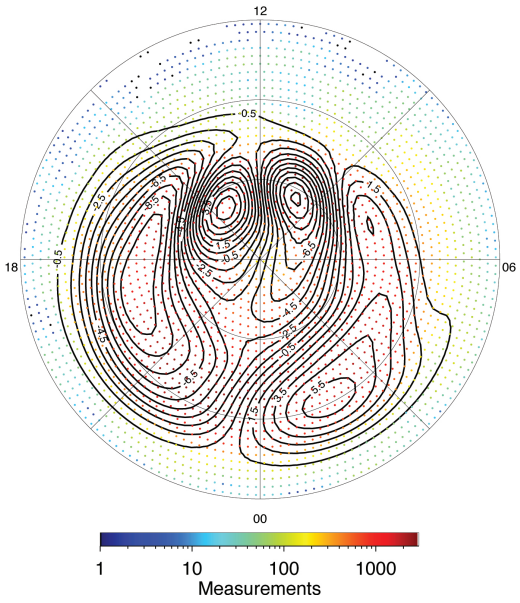

Figure A.5: Potential pattern for the bin with E_{RC} between 18 and 60 kV/Re and M_A between 4 and 6.

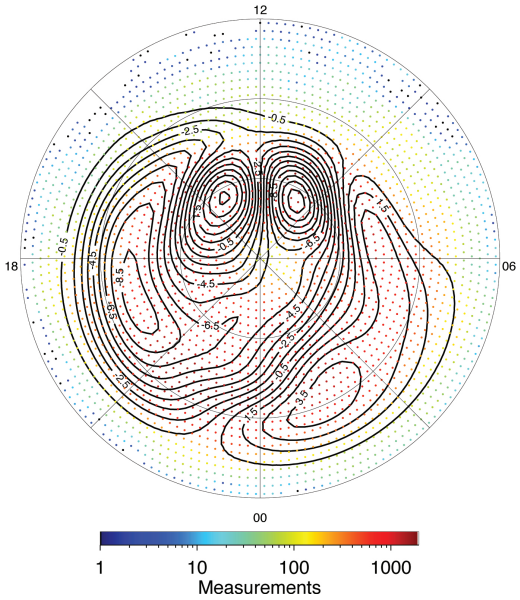

Figure A.6: Potential pattern for the bin with E_{RC} between 18 and 60 kV/Re and M_A between 5 and 7.

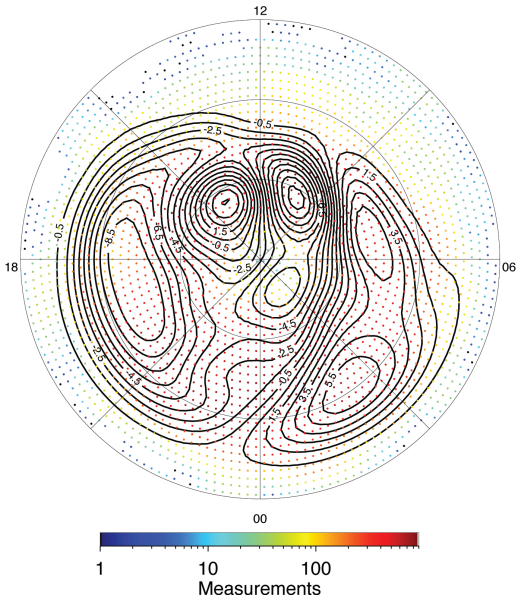

Figure A.7: Potential pattern for the bin with E_{RC} between 18 and 60 kV/Re and M_A between 6 and 8.

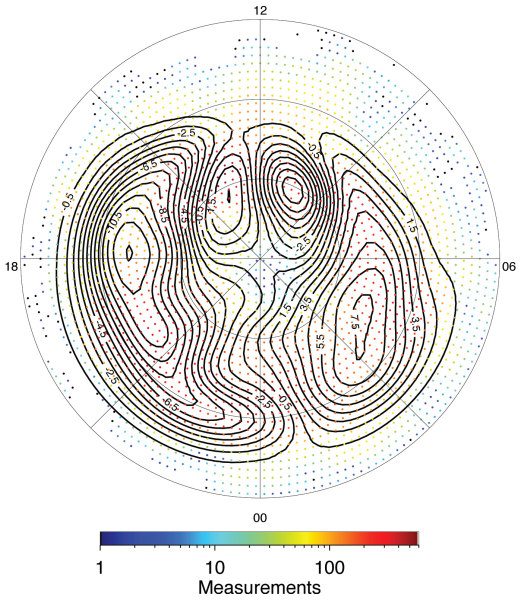

Figure A.8: Potential pattern for the bin with E_{RC} between 18 and 60 kV/Re and M_A greater than 8.

A.2 Average Potential Patterns Binned by Solar Wind Plasma Beta

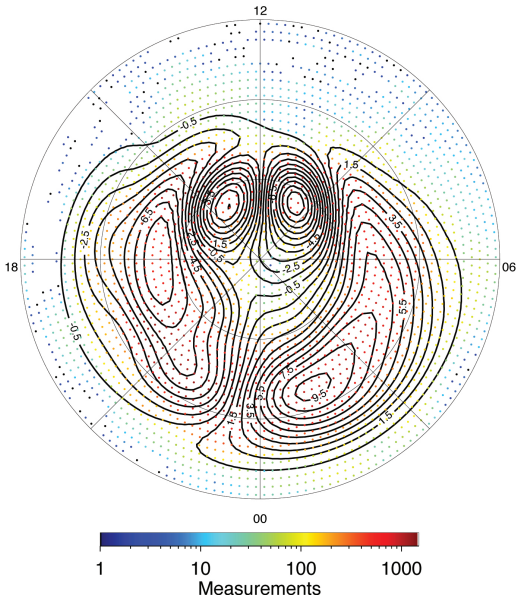

Figure A.9: Potential pattern for the bin with E_{RC} between 18 and 60 kV/Re and solar wind plasma beta between 0 and 0.025.

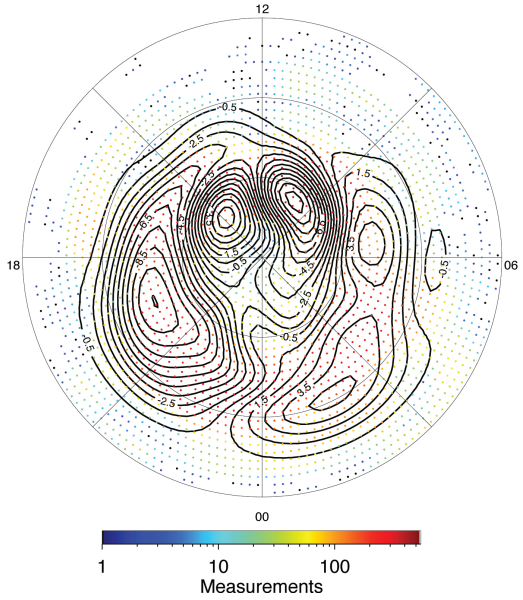

Figure A.10: Potential pattern for the bin with E_{RC} between 18 and 60 kV/Re and solar wind plasma beta between 0.025 and 0.05.

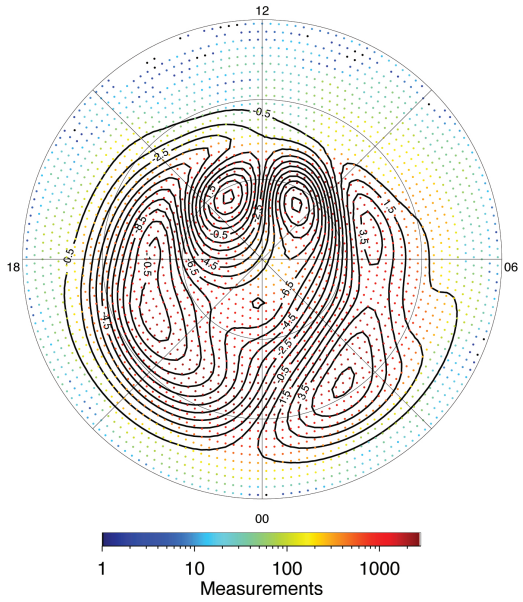

Figure A.11: Potential pattern for the bin with E_{RC} between 18 and 60 kV/Re and solar wind plasma beta between 0.05 and 0.2.

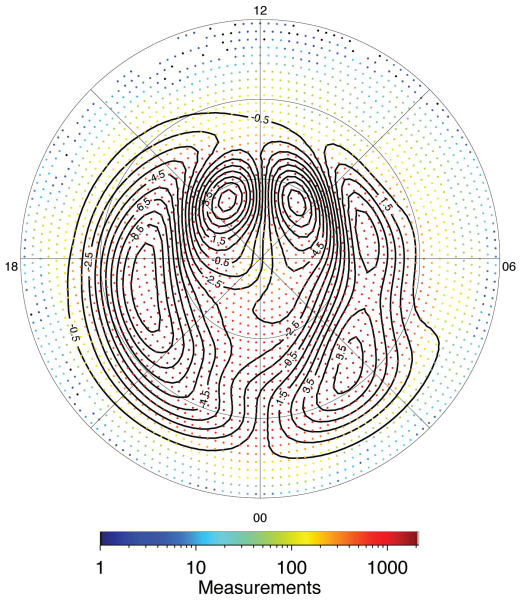

Figure A.12: Potential pattern for the bin with E_{RC} between 18 and 60 kV/Re and solar wind plasma beta between 0.1 and 0.3.

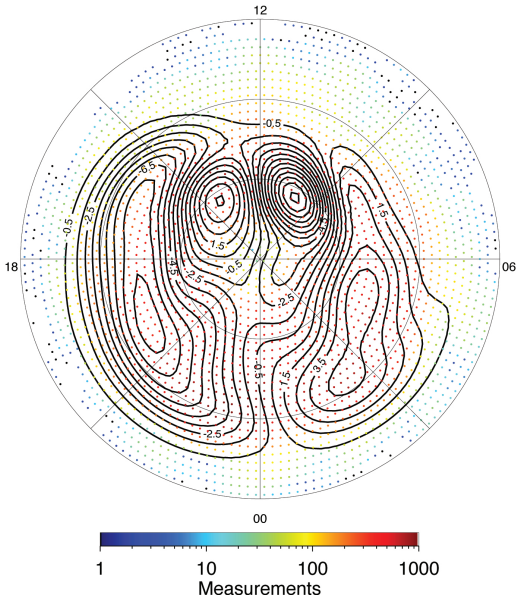

Figure A.13: Potential pattern for the bin with E_{RC} between 18 and 60 kV/Re and solar wind plasma beta between 0.2 and 0.4.

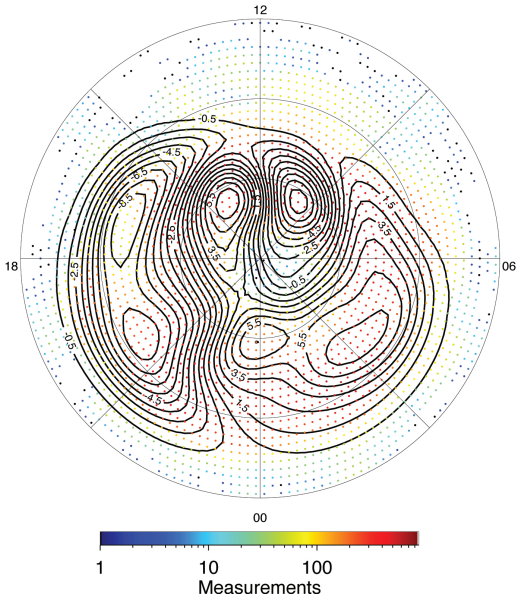

Figure A.14: Potential pattern for the bin with E_{RC} between 18 and 60 kV/Re and solar wind plasma beta between 0.3 and 0.5.

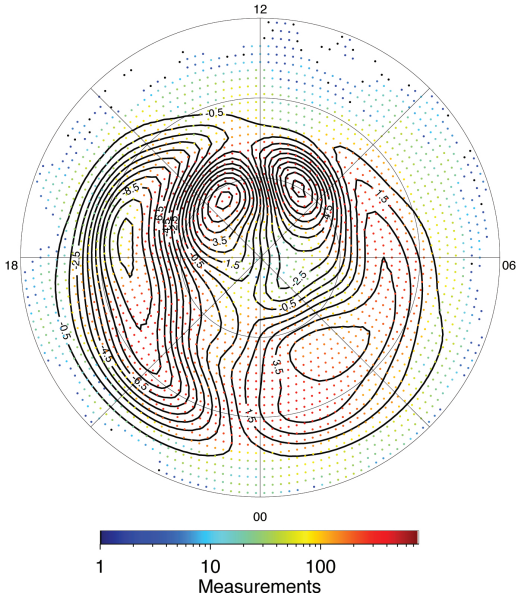

Figure A.15: Potential pattern for the bin with E_{RC} between 18 and 60 kV/Re and solar wind plasma beta between 0.4 and 0.7.

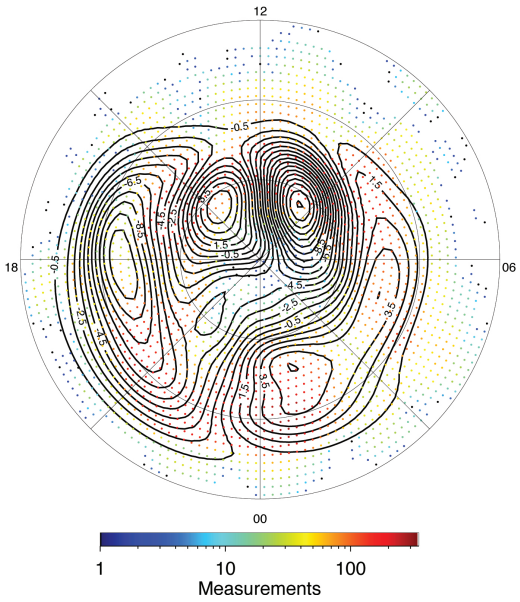

Figure A.16: Potential pattern for the bin with E_{RC} between 18 and 60 kV/Re and solar wind plasma beta between 0.5 and 0.8.

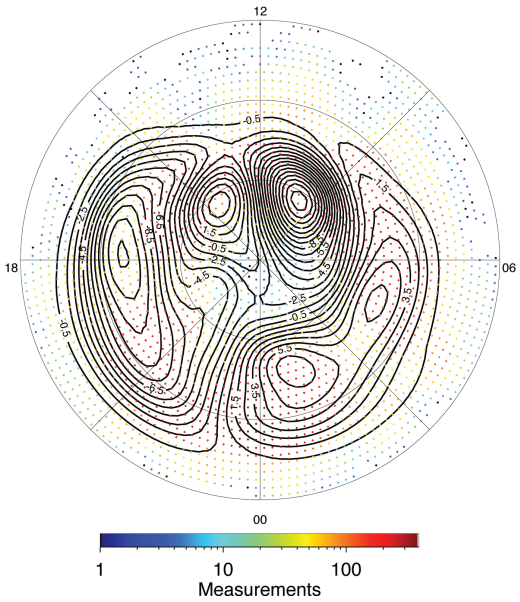

Figure A.17: Potential pattern for the bin with E_{RC} between 18 and 60 kV/Re and solar wind plasma beta between 0.5 and 1.

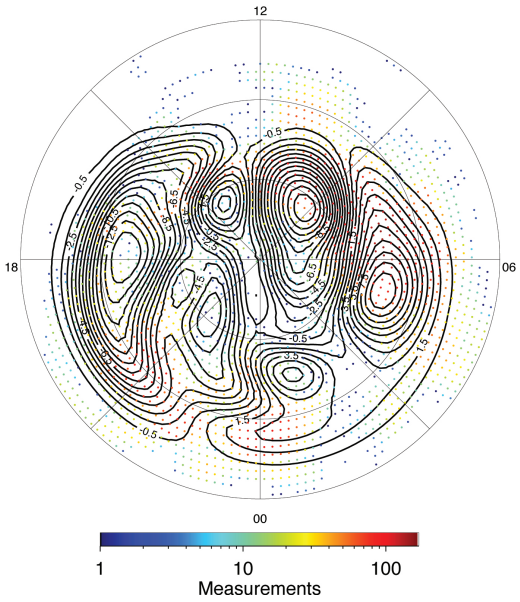

Figure A.18: Potential pattern for the bin with E_{RC} between 18 and 60 kV/Re and solar wind plasma beta between 0.6 and 1.

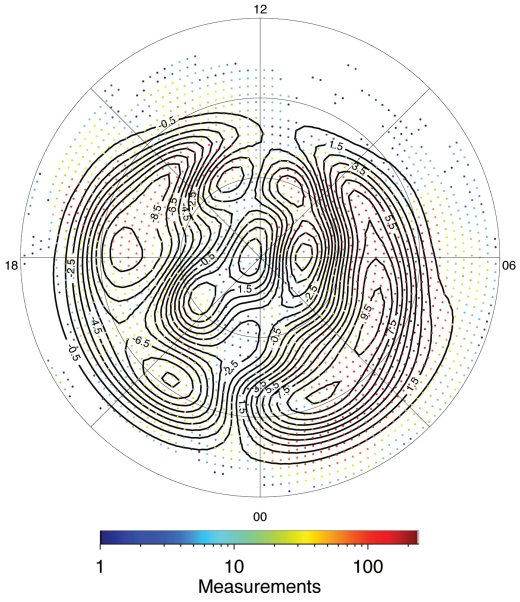

Figure A.19: Potential pattern for the bin with E_{RC} between 18 and 60 kV/Re and solar wind plasma beta greater than 1 (not used in any plots).

APPENDIX B

List of DMSP Passes Used In Chapter 7

B.1 DMSP Passes Used to Demonstrate Merging With SuperDARN Data

Table B.1: DMSP F13 Passes Used to Demonstrate Merging With SuperDARN Data

Number	Date (MM/DD/YYYY)	Time of Pass (UT)
1	01/18/1999	19:38 - 20:00
2	03/19/1999	14:02 - 14:26
3	03/19/1999	15:44 - 16:06
4	11/02/1999	22:30 - 22:54
5	03/10/2000	17:27 - 17:48

Continued on next page

Table B.1 – continued from previous page

Number	Date (MM/DD/YYYY)	Time of Pass (UT)
6	03/10/2000	19:08 - 19:29
7	03/10/2000	20:48 - 21:11
8	03/11/2000	18:55 - 19:16
9	03/31/2000	14:42 - 15:05
10	03/31/2000	18:05 - 18:25
11	05/09/2000	21:36 - 21:59
12	09/29/2000	16:23 - 16:45
13	11/21/2000	13:22 - 13:47
14	11/23/2000	11:15 - 11:39
15	12/04/2000	22:23 - 22:47
16	12/05/2000	00:05 - 00:29
17	12/18/2000	19:23 - 19:43
18	12/23/2000	16:37 - 16:57

Continued on next page

Table B.1 – continued from previous page

Number	Date (MM/DD/YYYY)	Time of Pass (UT)
19	12/27/2000	15:44 - 16:06
20	01/11/2001	12:28 - 12:52
21	01/11/2001	14:09 - 14:32
22	01/11/2001	19:15 - 19:35
23	01/15/2001	14:59 - 15:21
24	01/15/2001	16:41 - 17:02
25	01/16/2001	14:46 - 15:08
26	01/20/2001	12:12 - 12:36
27	01/20/2001	13:53 - 14:16
28	01/20/2001	15:34 - 15:57
29	12/12/2001	14:44 - 15:06
30	12/12/2001	16:26 - 16:47
31	12/12/2001	18:07 - 18:28

B.2 DMSP Passes Used to Study Potential Saturation

Table B.2: DMSP F13 Passes Used to Study Potential Saturation (F13 unless noted otherwise)

Date	**Time (UT)**	E_{KL}, **kV/Re**	P_{SW}, **nPa**	M_A	Q_A
02/18/1998	01:40 - 02:02	35.45	4.94	4.76	0.75
03/21/1998	12:21 - 12:45	30.12	3.81	4.51	0.63
06/06/1998	18:38 - 18:58	27.09	3.65	5.85	0.58
09/18/1998	12:34 - 12:58	34.28	8.49	6.35	0.67
10/19/1998	07:53 - 08:14	49.21	1.50	1.89	0.49
10/19/1998	09:35 - 09:58	46.77	1.66	2.13	0.53
10/19/1998	11:17 - 11:41	45.86	1.04	1.80	0.48
11/07/1998	12:28 - 12:52	38.38	5.28	6.44	0.80
11/13/1998	09:31 - 09:54	42.31	2.45	3.01	0.79
11/13/1998	11:13 - 11:38	41.62	2.03	2.65	0.77
12/11/1998	07:09 - 07:29	29.11	4.07	5.24	0.82

Continued on next page

Table B.2 – continued from previous page

Date	**Time (UT)**	E_{KL}, **kV/Re**	P_{SW}, **nPa**	M_A	Q_A
12/11/1998	12:14 - 12:38	27.16	2.74	4.58	0.81
01/14/1999	08:37 - 08:58	35.62	2.93	3.90	0.81
03/01/1999	00:43 - 01:07	32.40	5.84	5.66	0.72
03/01/1999	04:10 - 04:31	31.44	5.70	5.37	0.72
03/01/1999	16:04 - 16:26	36.03	4.46	4.37	0.65
11/13/1999	13:27 - 13:52	27.58	1.55	4.43	0.81
01/23/2000	00:08 - 00:33	33.99	2.37	3.46	0.92
01/23/2000	01:52 - 02:14	40.14	3.52	3.84	0.92
02/05/2000	19:31 - 19:53	26.86	4.59	5.29	0.79
06/26/2000	09:41 - 10:04	43.18	2.51	4.10	0.38
08/11/2000 (F12)	10:34 - 10:54	26.44	0.41	2.04	0.32
09/04/2000 (F12)	18:55 - 19:19	25.92	2.15	5.96	0.55
09/30/2000	12:47 - 13:11	27.67	3.98	5.61	0.64

Continued on next page

Table B.2 – continued from previous page

Date	**Time (UT)**	E_{KL}, **kV/Re**	P_{SW}, **nPa**	M_A	Q_A
10/04/2000	11:55 - 12:20	30.58	2.50	4.38	0.61
10/04/2000	13:37 - 14:00	28.56	1.17	3.23	0.54
10/14/2000	04:39 - 04:49	27.03	0.98	2.87	0.55
10/14/2000	06:21 - 06:41	26.60	0.96	2.94	0.56
10/29/2000	03:05 - 03:26	40.11	1.20	2.20	0.56
10/29/2000	04:48 - 05:08	38.88	0.71	1.75	0.50
10/29/2000	06:30 - 06:50	35.09	0.41	1.40	0.45
10/29/2000	08:12 - 08:33	30.74	0.55	1.74	0.50
10/29/2000	11:35 - 12:00	27.24	0.28	1.38	0.46
12/23/2000	03:00 - 03:21	28.29	2.38	3.97	0.77
01/21/2001	20:26 - 20:47	29.15	5.75	5.74	0.95
03/04/2001	23:05 - 23:30	32.25	0.94	2.68	0.49
03/20/2001	00:54 - 01:18	32.01	2.16	3.74	0.50

Continued on next page

Table B.2 – continued from previous page

Date	**Time (UT)**	E_{KL}, **kV/Re**	P_{SW}, **nPa**	M_A	Q_A
03/20/2001	04:21 - 04:42	36.83	1.73	2.93	0.45
09/23/2001	17:21 - 17:42	28.21	2.99	6.14	0.55
10/28/2001	07:52 - 08:12	36.56	5.59	5.53	0.69
10/31/2001	22:24 - 22:48	33.38	1.21	2.81	0.60
02/01/2002	13:23 - 13:48	26.47	5.18	6.24	0.84
03/01/2002	00:09 - 00:34	35.66	4.14	4.40	0.62
03/24/2002	00:00 - 00:24	27.17	1.73	4.55	0.51
05/11/2002	22:56 - 23:20	27.23	3.06	5.99	0.55
10/01/2002	08:39 - 09:01	46.23	3.49	2.69	0.48
10/01/2002	20:30 - 20:51	28.23	5.99	6.11	0.68
10/07/2002	12:21 - 12:46	25.86	3.25	4.92	0.63
10/14/2002	09:02 - 09:24	27.84	2.67	4.16	0.65
10/14/2002	12:25 - 12:50	28.97	4.13	4.82	0.70

Continued on next page

Table B.2 – continued from previous page

Date	**Time (UT)**	E_{KL}, **kV/Re**	P_{SW}, **nPa**	M_A	Q_A
11/20/2002	17:24 - 17:45	32.15	4.31	5.21	0.93
12/21/2002	03:22 - 03:43	29.81	3.23	6.52	0.79
03/20/2003	18:13 - 18:34	33.47	1.52	4.00	0.46
03/31/2003	13:56 - 14:20	28.06	1.41	4.65	0.52
08/18/2003	04:50 - 05:10	47.06	1.97	2.49	0.36

BIBLIOGRAPHY

BIBLIOGRAPHY

Axford, W., and C. Hines, A unifying theory of high-latitude geophysical phenomena and geomagnetic storms, *Can. J. Phys.*, *39*, 1433, 1961.

Baker, J. B. H., R. A. Greenwald, J. M. Ruohoniemi, K. Oksavik, J. W. Gjerloev, L. J. Paxton, and M. R. Hairston, Observations of ionospheric convection from the wallops superdarn radar at middle latitudes, *J. Geophys. Res.*, *112*, DOI:10.1029/2006JA011982, 2007.

Burgess, D., "Collisionless Shocks," in *Introduction to Space Physics,*edited by M.G. Kivelson and C.T. Russell*, p. 129*, Cambridge University Press, Cambridge, 1995.

Burke, W. J., M. C. Kelley, R. C. Sagalyn, M. Smiddy, and S. T. Lai, Polar cap electric field structures with a northward interplanetary magnetic field, *Geophys. Res. Lett.*, *6*, 21, 1979.

Carlson, H., and A. Egeland, "The aurora and auroral ionosphere," in *Introduction to Space Physics,*edited by M.G. Kivelson and C.T. Russell*, p. 459*, Cambridge University Press, Cambridge, 1995.

Chen, F. F., *Introduction To Plasma Physics and Controlled Fusion Volume 1: Plasma Physics, Second Edition*, Springer, New York, 1974.

Chisham, G., et al., A decade of the super dual auroral radar network (superdarn): scientific achievements, new techniques and future directions, *Surveys in Geophysics*, *28*(1), 33–109, 2007.

Chisham, G., I. J. Coleman, M. P. Freeman, M. Pinnock, and M. Lester, Ionospheric signiatures of split reconnection x-lines during conditions of imf $b_Z < 0$ and $|b_Y| \approx |b_Z|$: evidence for the anti-parallel merging hypothesis, *J. Geophys. Res.*, *107*(A1O), 1323, 2002.

Christiansen, F., V. O. Papitashvili, and T. Neubert, Seosonal variations of high-latitude field-aligned currents inferred from Ørsted and Magsat observations, *JGR*, *107*(A2), doi:10.1029/2001JA900104, 2002.

Crooker, N. U., Reverse convection, *J. Geophys. Res.*, *97*, 19363, 1992.

Crowley, G., D. J. Knipp, K. A. Drake, J. Lei, E. Sutton, and H. Lühr, Thermospheric density enhancements in the dayside cusp region during strong by conditions, *Geophys. Res. Lett.*, *37*(L07110), doi:10.1029/2009GL042143, 2010.

Dorelli, J., A. Bhattacharjee, and J. Raeder, Separator reconnection at earth's dayside magnetopause under northward interplanetary magnetic field conditions, *J. Geophys. Res.*, *112*(A02202), doi:10.1029/2006JA011877, 2007.

Drayton, R. A., A. V. Koustov, M. R. Hairston, and J.-P. Villain, Comparison of dmsp cross-track ion drifts and superdarn line-of-sight velocities, *Ann. Geophys.*, *23*, 2479–2486, 2005.

Drell, S., H. Foley, and M. Ruderman, Drag and propulsion of large satellites in the ionosphere: An alfvèn propulsion engine in space, *J. Geophys. Res.*, *70*, 3131, 1965.

Dremukhina, L., A. Levitin, and V. Papitashvili, Analytical representation of IZMEM model for near-real time prediction of electromagnetic weather, *J. Atmos. Sol. Terr. Phys.*, *60*(15), 1517–1529, 1998.

Dungey, J. W., Interplanetary magnetic field and the auroral zones, *Phys. Rev. Lett.*, *6*, 47, 1961.

Evans, J. V., Ionospheric movements measured by incoherent scatter: A review, *Journal of Atmospheric and Terrestrial Physics*, *34*(2), 175–209, 1972.

Friis-Christensen, E., and J. Wilhjelm, Polar cap currents for different directions of the interplanetary magnetic field in the $Y - Z$ plane, *J. Geophys. Res.*, *80*, 1248, 1975.

Fujii, R., T. ijima, T. Potemra, and M. Sugiura, Seasonal dependence of large-scale birkeland currents, *Geophys. Res. Lett.*, *8*, 1103–1106, 1981.

Gurnett, D., and A. Bhattacharjee, *Introduction to Plasma Physics With Space and Laboratory Applications*, Cambridge University Press, Cambridge, 2005.

Hairston, M., T. Hill, and R. Heelis, Observed saturation of the ionospheric polar cap during the 31 march 2001 storm, *Geophys. Res. Lett.*, *30*(6), doi:10.1029/2002GL015894, 2003.

Hairston, M. R., K. A. Drake, and R. Skoug, Saturation of the ionospheric polar cap potential during the october-november 2003 superstorms, *J. Geophys. Res.*, *110*, doi:10.1029/2004JA010864, 2005.

Hardy, D., H. Yeh, L. Schmitt, T. Schumaker, M. Gussenhoven, A. Huber, F. Marshall, and J. Pantazis, Precipitating electron and ion detectors (SSJ/4) for Block SD/ Flights 6-10 DMSP satellites: Calibration and data presentation, *Environ. Res. Pap.*, *902*, 1984.

Hardy, D. A., M. S. Gussenhoven, and E. Holeman, A statistical model of auroral electron precipitation, *J. Geophys. Res.*, *90*(A5), 4229–4248, 1985.

Hardy, D. A., M. S. Gussenhoven, and D. Brautigam, A statistical model of auroral ion precipitation, *J. Geophys. Res.*, *94*(A1), 370–392, 1989.

Hill, T., A. J. Dessler, and R. A. Wolf, Mercury and Mars: The role of ionospheric conductivity in the acceleration of magnetospheric particles, *Geophys. Res. Lett.*, *3*, 429 – 432, 1976.

Hughes, W., "The magnetopause, magnetotail and magnetic reconnection," in *Introduction to Space Physics,*edited by M.G. Kivelson and C.T. Russell*, p. 227*, Cambridge University Press, Cambridge, 1995.

Hundhausen, A., "The solar wind," in *Introduction to Space Physics,*edited by M.G. Kivelson and C.T. Russell*, p. 91*, Cambridge University Press, Cambridge, 1995.

Iijima, T., T. A. Potemra, L. J. Zanetti, and P. F. Bythrow, Large-scale Birkeland currents in the dayside polar region during strongly northward IMF: A new Birkeland current system, *J. Geophys. Res.*, *89*, 7441, 1984.

Ip, W. H., and A. Kopp, Resistive mhd simulations of ganymede's magnetosphere 2. birkeland currents and particle energetics, *J. Geophys. Res.*, *107*, 1491, 2002.

Jackson, J. D., *Classical Eelectrodynamics*, John Wiley and Sons, New York, 1975.

Kan, J. R., and L. C. Lee, Energy coupling function and solar wind magnetosphere dynamo, *Geophys. Res. Lett.*, *6*, 577, 1979.

Karemcheti, K., *Principles of Ideal Fluid Aerodynamics*, Krieger, Malabar, 1966.

Kendall, M., A new measure of rank correlation, *Biometrika*, *30*, 81–89, 1938.

King, J. H., and N. E. Papitashvili, Solar wind spatial scales in and comparisons of hourly wind and ace plasma and magnetic field data, *J. Geophys. Res.*, *110*, doi:10.1029/2004JA010804, 2005.

Kivelson, M., "Pulsations and magnetohydrodynamic waves," in *Introduction to Space Physics,*edited by M.G. Kivelson and C.T. Russell*, p. 330*, Cambridge University Press, Cambridge, 1995.

Kivelson, M. G., and A. J. Ridley, Saturation of the polar cap potential: Inference from alfvèn wing arguments, *J. Geophys. Res.*, *113*, doi:10.1029/2007JA012302, 2008.

Kivelson, M. G., and C. T. Russell, Geophysical coordinate transformations, in *Introduction to Space Physics*, edited by M. G. Kivelson, and C. T. Russell, pp. 531–543, Cambridge University Press, Cambridge, UK, 1995.

Kopp, A., and W. H. Ip, Resistive mhd simulations of ganymede's magnetosphere 2. time variabilities of the magnetic field topology, *J. Geophys. Res.*, *107*, 1490, 2002.

Koustov, A. V., G. Y. Khachikjan, R. A. Makarevich, and C. Bryant, On the superdarn cross polar cap potential saturation effect, *Ann. Geophys.*, *27*, 2755–3764, 2009.

Linker, J. A., K. K. Khurana, M. G. Kivelson, and R. J. Walker, MHD simulation of Io's interaction with the plasma torus, *J. Geophys. Res.*, *103*(E9), 19,867, 1998.

Lopez, R., R. Bruntz, E. Mitchell, M. Wiltberger, J. Lyon, and V. Merkine, The role of magnetosheath force balance in regulating the dayside reconnection potential, 2010.

Luhmann, J., "Ionospheres," in *Introduction to Space Physics,*edited by M.G. Kivelson and C.T. Russell*, p. 183*, Cambridge University Press, Cambridge, 1995.

Lühr, H., M. Rother, W. Kohler, P. Ritter, and L. Grunwaldt, Thermospheric up-welling in the cusp region, evidence from champ observations, *Geophys. Res. Lett.*, *31*(L06805), doi:1029/2003GL09314, 2004.

Lyatsky, W., G. V. Khazanov, and J. A. Slavin, Saturation of the electric field transmitted to the magnetosphere, *J. Geophys. Res.*, *In Press*, doi:10.1029/2009JA015091, 2010.

Mitchell, E. J., R. E. Lopez, R. J. Bruntz, M. Wiltberger, J. G. Lyon, R. C. Allen, S. J. Cockrell, and P. L. Whittlesey, Saturation of the transpolar potential for large y-component interplanetary magnetic field, *J. Geophys. Res.*, *115*(A06201), doi:10.1029/2009JA015119, 2010.

Musko, S. B., C. R. Clauer, A. Ridley, and K. Arnett, Autonomous low power instrument platform to enable remote high latitude array deployment, *Rev. Sci. Inst.*, *80*(4), 044501, 2009.

Neubauer, F., Nonlinear standing alfvèn wave current system at io: Theory, *J. Geophys. Res.*, *85*, 1171–1178, 1980.

Newell, P., and C.-I. Meng, Mapping the dayside ionosphere to the magnetosphere according to particle precipitation characteristics, *Geophys. Res. Lett.*, *19*, 609, 1992.

Newell, P. T., K. Liou, and G. R. Wilson, Polar cap particle precipitation and aurora: Review and commentary, *Journal of Atmospheric and Solar-Terrestrial Physics*, *71*(2), 199–215, 2008.

Papitashvili, V. O., and F. J. Rich, High-latitude ionospheric convection models derived from Defense Meteorological Satillite Program ion drift observations and parameterized by the interplanetary magnetic field strength and direction, *J. Geophys. Res.*, *107*, doi:10.1029/2001JA000264, 2002.

Papitashvili, V. O., O. A. Troshichev, D. S. Faermark, and A. N. Zaitzev, Linear dependence of the intensity of geomagnetic variations in the polar region on the magnitudes of the southern and northern components of the interplanetary magnetic field, *Geomagn. Aeron. Engl. Transl.*, *21*, 565, 1981.

Papitashvili, V. O., B. A. Belov, D. S. Faermark, Y. I. Feldstein, S. A. Golyshev, L. I. Gromova, and A. E. Levitin, Electric potential patterns in the northern and southern polar regions parameterized by the interplanetary magnatic field, *J. Geophys. Res.*, *99*, 13,251, 1994.

Papitashvili, V. O., F. J. Rich, M. A. Heunemann, and M. R. Hairston, Parameterization of the Defense Meteorological Satellite Program ionospheric electrostatic potentials by the interplanetary magnetic field stength and direction, *J. Geophys. Res.*, *104*, 177, 1999.

Papitashvili, V. O., F. Christiansen, and T. Neubert, A new model of field-aligned currents derived from high-precision satellite magnetic field data, *Geophys. Res. Lett.*, *29*, doi:10.1029/2001GL014207, 2002.

Pearson, F., *Map Projections: Theory and Applications*, CRC Press, Boca Raton, 1990.

Provan, G., T. K. Yeoman, S. E. Milan, J. M. Ruohoniemi, and R. Barnes, An assessment of the map-potential and beam swinging techniques for measuring the ionospheric convection pattern using data from the superdarn radars, *Ann. Geophysicae*, *20*, 191, 2002.

Rastatter, P., M. Hesse, M. Kuznetsova, J. Sigwarth, J. Raeder, and T. Gombosi, Polar cap size during 14-16 july 2000 (bastille day) solar coronal mass ejection event: Mhd modeling and satellite imager observations, *J. Geophys. Res.*, *110*, doi:10.1029/2004JA010672, 2005.

Rees, M., *Physics and Chemistry of the Upper Atmosphere*, Cambridge University Press, Cambridge, 1989.

Reiff, P., R. Spiro, and T. Hill, Dependence of polar cap potential on interplanetary parameters, *J. Geophys. Res.*, *86*, 7,639, 1981.

Reiff, P. H., and J. G. Luhmann, Solar wind control of the polar cap voltage, in *Solar Wind - Magnetosphere Coupling,* edited by Y. Kamide and J.A. Slavin*, p. 507*, Terra Scientific Publishing, Tokyo, Japan, 1986.

Reiff, P. H., J. L. Burch, and R. W. Spiro, Cusp proton signiatures and the interplanetary magnetic field, *J. Geophys. Res.*, *85*, 5997–6005, 1980.

Rich, F. J., and M. Hairston, Large-scale convection patterns observed by DMSP, *J. Geophys. Res.*, *99*, 3,827, 1994.

Richmond, A., and J. Thayer, "Ionospheric electrodynamics: A Tutorial", in Magnetospheric Current Systems, AGU Geophys. Monogr. Ser., Vol. 118, *edited by S. Ohtani, R. Fujii, M. Hesse, and R. L. Lysak, p. 131*, AGU, Washington, D.C., 2000.

Ridley, A., Alfvèn wings at the earth's magnetosphere under strong interplanetary magnetic field, *Ann. Geophys.*, *23*, 533, 2007.

Ridley, A. J., Estimations of the uncertainty in timing the relationship between magnetospheric and solar wind processes, *J. Atmos. Sol. Terr. Phys.*, *62*, 757, 2000.

Robinson, R., R. Vondrak, K. Miller, T. Dabbs, and D. Hardy, On calculating ionospheric conductances from the flux and energy of precipitating electrons, *J. Geophys. Res.*, *92*, 2,565, 1987.

Ruohoniemi, J., and S. K. Baker, Large-scale imaging of high-latitude convection with super dual auroral radar network hf radar observations, *J. Geophys. Res.*, *103*(A9), 20797–20811, 1998.

Ruohoniemi, J. M., and R. A. Greenwald, Statistical patterns of the high-latitude convection obtained from Goose Bay HF radar observations, *J. Geophys. Res.*, *101*, 21,743, 1996.

Ruohoniemi, J. M., R. Greenwald, K. Baker, J. Villain, and M. McCready, Drift motions of small-scale irregularities in the high-latitude f region: an experimental comparison with plasma drift motions, *J. Geophys. Res.*, *92*(A5), 4553–4564, 1987.

Russel, C. T., J. Luhmann, and G. Lu, Nonlinear response of the polar ionosphere to large values of the interplanetary electric field, *J. Geophys. Res.*, *106*(A9), 21083–21094, 2001.

Russell, C. T., "A brief history of solar-terrestrial physics," in *Introduction to Space Physics,*edited by M.G. Kivelson and C.T. Russell*, p. 227*, Cambridge University Press, Cambridge, 1995.

Sckopke, N., G. Paschmann, G. Haerendel, B. U. O. Sonnerup, S. J. Bame, T. G. Forbes, J. E. W. Hones, and C. T. Russell, Structure of the low-latitude boundary layer, *J. Geophys. Res.*, *86*, 2099–2110, 1981.

Scurry, L., C. T. Russel, and J. T. Gosling, Geomagnetic activity and the beta dependance of the dayside reconnection rate, *J. Geophys. Res.*, *99*, 14,811–14,814, 1994.

Shepherd, S., R. Greenwald, and J. Ruohoniemi, Cross polar cap potentials measured with super dual auroral radar network during quasi-steadi solar wind and interplanetary magnetic field conditions, *J. Geophys. Res.*, *107*(A7), doi:10.1029/2001JA000152, 2002.

Siscoe, G., J. Raeder, and A. Ridley, Transpolar potential saturation models compared, *J. Geophys. Res.*, *109*(A09203), doi:10.1029/2003JA010318, 2004.

Siscoe, G. L., N. U. Crooker, and K. D. Siebert, Transpolar potential saturation: Roles of region 1 current system and solar wind ram pressure, *J. Geophys. Res.*, *107*(A10), 2002a.

Siscoe, G. L., G. M. Erickson, B. U. O. Sonnerup, N. C. Maynard, J. A. Schoendorf, K. D. Siebert, D. R. Weimer, W. W. White, and G. R. Wilson, Hill model of transpolar potential saturation: Comparisons with MHD simulations, *J. Geophys. Res.*, *107*(A6), 2002b.

Song, Y., and R. Lysak, "Paradigm Transition in Cosmic Plasma Physics, Magnetic Reconnection and the Generation of Field-Aligned Current," in *Magnetospheric Current Systems, AGU Geophysical Monograph 118,*edited by S. Ohtani, R. Fujii, M. Hesse and R.L. Lysak*, p. 11*, Cambridge University Press, Cambridge, 1995.

Sonnerup, B. U. O., Magnetopause reconnection rate, *J. Geophys. Res.*, *79*, 1546–1549, 1974.

Spearman, C., The proof and measurement of association between two rings, *American Journal of Psychology*, *15*, 72–101, 1904.

Stone, E., A. Frandsen, R. Mewaldt, E. Christian, D. Margolies, J. Ormes, and F. Snow, The advanced composition explorer, *Space Science Reviews*, *86*, 1–22, 1998.

Sundberg, K. A. T., J. A. Cumnock, and L. G. Blomberg, The reverse convection potential: a statistical study of the general properties of lobe reconnection and saturation effects during northward imf, *J. Geophys. Res*, *114, A06205*, doi:10.1029/2009JA014069, 2009.

Walker, R., and C. Russell, "Solar-wind interactions with magnetized planets," in *Introduction to Space Physics,*edited by M.G. Kivelson and C.T. Russell*, p. 164*, Cambridge University Press, Cambridge, 1995.

Watanabe, M., K. Kabin, G. J. Sofko, R. Rankin, T. I. Gombosi, A. J. Ridley, and C. R. Clauer, The internal reconnection for northward interplanetary magnetic field, *J. Geophys. Res.*, *110*, doi:10.1029/2004JA010832, 2005.

Watanabe, M., G. J. Sofko, D. A. Andre, J. M. Ruohoniemi, M. R. Hairston, and K. Kabin, Ionospheric signiatures of internal reconnection for northward interplanetary magnetic field: Observation of "reciprocal cells" and magnetosheath ion precipitation, *J. Geophys. Res.*, *A06201*, doi:10.1029/2005JA011446, 2006.

Weimer, D., Models of high-latitude electric potentials derived with a least error fit of spherical harmonic coefficients, *J. Geophys. Res.*, *100*, 19,595, 1995.

Weimer, D., A flexible, IMF dependent model of high-latitude electric potential having "space weather" applications, *Geophys. Res. Lett.*, *23*, 2,549, 1996.

Weimer, D., An improved model of ionospheric electric potentials including substorm perturbations and application to the geospace environment modeling november 24, 1996, event, *J. Geophys. Res.*, *106*, 407, 2001a.

Weimer, D., Maps of field-aligned currents as a function of the interplanetary magnetic field derived from Dynamic Explorer 2 data, *J. Geophys. Res.*, *106*, 12,889, 2001b.

Weimer, D., D. Ober, N. Maynard, M. Collier, D. McComas, N. Ness, C. Smith, and J. Watermann, Predicting interplanetary magnetic field (imf) propagation delay times using the minimum variance technique, *J. Geophys. Res.*, *108*(A1), doi:10.1029/2002JA009405, 2003.

Wild, J., et al., The location of the open-closed magnetic field line boundary in the dawn sector auroral ionosphere, *Ann. Geophys.*, *22*, 3625–3639, 2004.

Wilder, F. D., C. R. Clauer, and J. B. H. Baker, Reverse convection potential saturation during northward imf under various driving conditions, *J. Geophys. Res.*, *114*(A8), doi: 10.1029/2009JA014266, 2009.

Winglee, R., D. Chua, M. Brittnacher, G. Parks, and G. Lu, Global impact of ionospheric outflows in the dynamics of the magnetosphere and cross polar cap potential, *J. Geophys. Res.*, *107*(A9), doi:10.1029/2002JA009241, 2002.

Woch, J., and R. Lundin, Magnetosheath plasma precipitation in the polar cusp and its control by the interplanetary magnetic field, *J. Geophys. Res.*, *97*, 1421–1430, 1992.

Wolf, R., "Magnetospheric Configuration," in *Introduction to Space Physics,*edited by M.G. Kivelson and C.T. Russell*, p. 288*, Cambridge University Press, Cambridge, 1995.

Xu, L., A. V. Koustov, J. S. Xu, R. A. Drayton, and L. Huo, A 2-d comparison of ionospheric convection derived from superdarn and dmsp measurements, *Adv. Spa. Res.*, *47*, 1259–1266, 2007.